INFLUENCE OF DILATANCY ON SLIP PLANES AND ON LOCALIZATION OF STRAINS

by

Adlen Altunbaş

B.S., Civil Engineering, İstanbul University, 2009,

M.S., Civil Engineering, Boğaziçi University, 2012

Submitted to the Institute for Graduate Studies in
Science and Engineering in partial fulfillment of
the requirements for the degree of
Doctor of Philosophy

Graduate Program in Civil Engineering

Boğaziçi University

2015

INFLUENCE OF DILATANCY ON SLIP PLANES AND ON LOCALIZATION OF STRAINS

APPROVED BY:

Assoc. Prof. Özer Çinicioğlu (Thesis Supervisor)	.....
Prof. Gökhan Baykal	.....
Assoc. Prof. İlknur Bozbey	.....
Prof. Erol Güler	.....
Assoc. Prof. Mehmet Murat Monkul	.....

DATE OF APPROVAL: 12 December 2014

This PhD thesis is dedicated to my lovely son, Mustafa, and my adorable husband, Akın. I am truly thankful for having you in my life...

Adlen Altunbaş

ACKNOWLEDGEMENTS

First and foremost, I would like to thank my thesis supervisor and mentor Assoc. Prof. Özer Çinicioğlu for his constant interest, patience, immense knowledge, supervision on the development of this research thesis and helping me through my whole academic life. I would also like to thank him for the many hours spent reading my thesis and various publications and providing feedback and input.

I want to express my deep and sincere gratitude to Behzad Soltanbeigi for his assistance in the experiments, discussion, and exchange of ideas. I am really proud that I have had an opportunity to work closely with such a great person.

I would also like to thank the Scientific and Technological Research Council of Turkey (TUBITAK Project 110M595) for providing financial support for this thesis.

I am also grateful to my thesis committee members, Prof. Erol Güler, Prof. Gökhan Baykal, Assoc. Prof. İlknur Bozbey and Assoc. Prof. Mehmet Murat Monkul for their support and insightful comments to improve my PhD study.

My gratitude also goes to my colleague Marat Abzal and Ahmet Talha Gezgin for their assistance throughout the experiments. This PhD has involved a large number of laboratory investigations, which could not have been completed without their patience.

In particular, I would like to give my special thanks to my dear friend İrem Şanal for endless support, patience, shearing ideas and comments. She is the sources of great joy and patience.

I wish to express my unending gratitude to my family, especially my parents for their unwavering support and encouragement throughout my life. Words are not enough to thank my parents for their love, support, and encouragement in every aspect of my life.

Last but most certainly not least, I would like to express my deepest gratitude, which cannot be put into words, for the happiness, continuous caring and understanding which I received from my husband Akın. He always gives me the strength to succeed in pursuing my goals. Without his support, I would not have been able to continue my study.

ABSTRACT

INFLUENCE OF DILATANCY ON SLIP PLANES AND ON LOCALIZATION OF STRAINS

Correct calculation of slip plane geometry plays a key role in the design of geotechnical structures. The goal of this study is the identification of slip planes in cohesionless soils retained behind walls and quantifying the failure plane geometries to measurable and calculable soil properties. For this purpose, 1 g small scale retaining wall model tests were performed. Soil mass behind the model retaining wall was prepared at different relative densities corresponding to different dilation angles (ψ_p) to monitor both the effect of dilative behavior on slip plane geometry and strain distribution within the failure wedge. Model test results were analyzed using particle image velocimetry (PIV) for the detection and identification of shear planes associated with retaining wall failure. The results show that generated failure surfaces at active and passive failure states behind horizontally translating rigid walls are not planar. This is an expected outcome which is attributed to the dilatant nature of the backfill. However, as a novel approach, this study attempts to quantify the geometry of failure planes as functions of dilatancy angle. Thus, an empirical equation that uses dilatancy angle as input is proposed to predict the failure surface geometry of cohesionless backfills behind retaining walls at active state. It is observed that the geometries of slip planes calculated using the proposed empirical equation are in good agreement with the results from the experimental models. Addittionally, shear band formation within the active failure wedge is investigated using an image processing technique in MATLAB program, which allows the examination of the distribution of shear strains along the shear bands. Accordingly, it is noted that dilatant behavior influences both thickness and inclination of shear bands.

ÖZET

GENLEŞİM AÇISININ GÖÇME YÜZEYLERİNE VE BÖLGESEL GERİNİM YOĞUNLAŞMASINA ETKİSİ

Göçme yüzeyi geometrisinin gerçekçi bir şekilde tanımlanabilmesi geoteknik yapıların doğru şekilde dizayn edilebilmesi açısından son derece önemlidir. Bu çalışma nın amacı, kohezyonsuz dolguların arkasında meydana gelen göçme yüzeylerini ölçüle bilir ve hesaplanabilir zemin özellikleri kullanılarak tanımlayabilmek ve nicelleştirebil mektir. Bu amaçla, 1 g küçük ölçekli istinat duvarı model deneyleri gerçekleştirilmiştir. İstinat duvarı arkasındaki dolgu, değişik genleşim açılarında (ψ_p) hazırlanmış olup genleşim açısının (ψ_p) göçme yüzeyi geometrisine ve göçme kaması içinde oluşan şekil değiştirme dağılımlarına olan etkisi incelenmeye çalışılmıştır. Model deney sonuçları, dolgu arkasında meydana gelen göçme yüzeyinin gözlenebilmesi ve tanımlanabilmesi amacıyla parçacık görüntülü hız ölçümü (PGHÖ) yönteminden faydalanılarak analiz edilmiştir. Elde edilen sonuçlar göstermektedir ki; aktif ve pasif göçme durumlarının duvar ötelenmesi ile modellendiği bir dolguda oluşan göçme yüzeyi geometrisi genleşim davranışından dolayı doğrusal olmayıp eğrisel bir geometri oluşturmaktadır. Zeminlerin genleşim özelliklerinden dolayı bu durum beklenen bir sonuçtur. Fakat, bu çalışmada yeni bir yaklaşım olarak, meydana gelen göçme yüzeyleri, genleşim açısına bağlı olarak nicelleştirilmeye çalışılmıştır. Bu sayade, aktif göçme durumunda meydana gelen göçme yüzeyini genleşim açısını göz önüne alarak hesaplayabilen bir eşitlik önerilmiştir. Model deney sonuçlarından elde edilen göçme yüzeyi geometrisinin ve önerilen eşitliğin kullanılması ile elde edilen göçme yüzeyleri karşılaştırılmış olup birbiriyle uyumlu sonuçlar elde edildiği gözlenmiştir. Ek olarak, aktif göçme kaması içinde meydana gelen kayma kuşaklarının oluşumunu gözlemleyebilmek için MATLAB programının görüntü işleme özelliğinden faydalanılmıştır. Analiz sonuçlarına göre, genleşim davranışının kayma bandının kalınlığını ve eğimini etkilediği görülmüştür.

TABLE OF CONTENTS

ACKNOWLEDGEMENTS iv
ABSTRACT vi
ÖZET vii
LIST OF FIGURES x
LIST OF TABLES xviii
LIST OF SYMBOLS xix
LIST OF ABBREVIATIONS xxii
1. INTRODUCTION 1
2. LITERATURE REVIEW 5
2.1. Active Earth Pressure and Slip Plane Geometry 5
2.1.1. Coulomb Theory 6
2.1.2. Rankine Theory 8
2.1.3. Others Researchers 9
2.2. Passive Earth Pressure and Slip Plane Geometry 14
2.2.1. Coulomb Theory 15
2.2.2. Rankine Theory 17
2.2.3. Terzaghi Theory 18
2.2.4. Other Researchers 18
2.3. Strain Localization and Visualization 24
2.4. Dilatancy 36
3. SMALL SCALE RETAINING WALL MODEL 39
3.1. Physical Model 39
3.2. Equipments Used in PIV Analysis 43
3.2.1. Digital Camera 43
3.2.2. Remote Controller 44
3.2.3. Tripod 45
3.2.4. Lights 45
4. BACKFILL PROPERTIES AND SAMPLE PREPARATION 46
4.1. Backfill Properties of Akpınar Sand 46

4.1.1. Sieve Analysis 46
4.1.1.1. The Result of Sieve Analysis 46
4.2. Particle Shape of Akpınar Sand 47
4.2.1. Determination of Specific Gravity 49
4.2.2. Determination of Minimum and Maximum Relative Densities . 50
4.2.3. Direct Shear Test for the Determination of Interface Friction Angles 50
4.2.4. Triaxial Test 52
4.3. Sample Preparation 54
5. DILATANCY CALCULATION BASED ON IN-SITU PROPERTIES 56
6. VISUALIZATION OF DEFORMATION 59
6.1. PIV Programs used for the Applications 60
6.2. GeoPIV for the Slip Plane Geometry 61
6.2.1. Determination of Patch Size 66
7. RESULTS 69
7.1. Slip Plane Geometry based on PIV at Active State 69
7.2. Influence of Interface Friction between wall and backfill at Active Failure 74
7.3. Influence of Dilatancy on Slip Plane Geometry at Active State 75
7.4. Determination of Slip Plane Geometry 79
7.5. Slip Plane Geometry based on PIV at Passive State 84
7.6. Influence of Dilatancy on Slip Plane Geometry at Passive State 86
8. SHEAR BAND FORMATION 90
9. DISCUSSION 102
10. CONCLUSIONS 107
REFERENCES 109

LIST OF FIGURES

Figure 2.1. Active Case with c = 0, Coulomb Theory (After Craig 2004). . . . 6

Figure 2.2. Active and Passive Rankine States (Craig, 2004). 8

Figure 2.3. Generated Failure Surface within the Backfill Resulting from a) Rotation about the Base b) Rotation about the Top (Paik and Salgado, 2003). 9

Figure 2.4. Slip Surfaces Plotted from Equation 2.5 and Experimental Data a) $\phi = 40^o$; b) $\phi = 37^o$; c) $\phi = 32^o$; d) $\phi = 30^o$; e) $\phi = 25^o$; f) Experimental Curves for $\phi = 37^o$. 10

Figure 2.5. Modes of Wall Movement (Matsuzawa and Hazarika, 1996). 11

Figure 2.6. Movable Earth Support Apparatus (Toyosawa *et al.*, 2006). 12

Figure 2.7. Schematic Diagram of Retaining Wall Model: (a) Container Geometry and Moving Scheme; (b) Experimental Set-up (plan) (Khosravi *et al.*, 2013). 14

Figure 2.8. Curvature due to the Wall Friction (Craig 2004). 17

Figure 2.9. Log Spiral Failure Mechanism after Terzaghi (Fang *et al.*, 2002). . 18

Figure 2.10. Method of slices (After Shield and Tolunay 1973). 19

Figure 2.11. Model Retaining Wall (Fang *et al.*, 2006). 21

Figure 2.12. Schematic Elevation View of Passive Earth Pressure Experiment with Instrumentation Layout (Wilson and Elgamal 2010). 23

Figure 2.13. Broken Foam Cores Showing Shape of Failure Wedge (Wilson and Elgamal 2010). 23

Figure 2.14. Biaxial Apparatus (Desrues and Hammad, 1989). 26

Figure 2.15. Evolution of the Localized Zone with employing PIV in the Active Case (Nübel and Weitbrecht, 2002). 27

Figure 2.16. Schematic Diagram of the Plane Strain Apparatus. 28

Figure 2.17. Experimental Set-Up for Pull-Out Test (Slominski *et al.*, 2005). . . 29

Figure 2.18. Test Box Geometry and Loading Scheme for the Active "Wall" Model (Lesniewska and Wood, 2011). 31

Figure 2.19. Experimental Set-up (Niedostatkiewicz *et al.*, 2011). 32

Figure 2.20. Conceptual Representation of Plane Strain Test Specimen and Surrounding Hardware (Rechenmacher *et al.*, 2011). 33

Figure 2.21. Evolution of Strains During Test (Pietrzak and Lesniewska, 2012). 34

Figure 2.22. Test Box (Tehrani *et al.*, 2014). 35

Figure 2.23. Test and Camera Setup (Tehrani *et al.*, 2014). 36

Figure 3.1. Retaining Wall Model Set-Up (a) Photograph c) (b) Horizontal Cross-Section. 40

Figure 3.2. (a) Positions of the Pressure Transducers Along the vertical Axis of The Retaining Wall Model, (b) Face View of a Pressure Transducer, (c) Side View of a Pressure Transducer. 41

Figure 3.3. Location of Pressure Transducers and Transparent Side Walls. . . 41

Figure 3.4. Movable Part of Model System. 41

Figure 3.5. Back Face of the Wall. 42

Figure 3.6. Data Logger with 16 Channels. 43

Figure 3.7. Digital Camera and Remote Controller used in the Experiments. . 43

Figure 4.1. Particle Grading Curves for Akpınar Sand. 47

Figure 4.2. Particle Shape Determination-Sphericity (S) and Roundness (R) (Cho *et al.*, 2006). 48

Figure 4.3. Particle Shape Determination-Sphericity (S) and Roundness (R) (Cho *et al.*, 2006). 48

Figure 4.4. Particle Shape Determination on Shape Chart. 49

Figure 4.5. Wall-Backfill Interface Friction (δ_{wb}) Obtained by Conducting Direct Shear Test. 51

Figure 4.6. Plexiglass-backfill Interface Friction (δ_{pb}) Obtained by Conducting Direct Shear Test. 51

Figure 4.7. Triaxial Sample at Failure. 53

Figure 4.8. Preparation of Backfill with Dry-Pluviation Method. 54

Figure 4.9. Extraction of Density Can. 55

Figure 5.1. Comparison of Calculated and Measured ψ_p using Equation 5.1 (Çinicioğlu and Abadkon 2014). 57

Figure 5.2. Comparison of Calculated and Measured ϕ'_p using Equation 2.11 (Çinicioğlu and Abadkon 2014). 58

Figure 6.1. PIVlab Results for the Visialization of Deformation behind the Retaining Wall. 61

Figure 6.2. Principles of PIV Analysis (White and Take, 2002). 63

Figure 6.3. Determination of Displacement Vector Field a) Determination of Area of Interest b) Pixel Intensity Variation Signature c) Displacement Vector. 63

Figure 6.4. Deformation Determination in PIV a) Initial Image Divided to Square Patches b) Displacement Vector. 64

Figure 6.5. Flowchart of the GeoPIV Analysis Procedure (After White and Take, 2002). 64

Figure 6.6. Typical PIV Results for Active Retaining Wall Translation a) Shear Strain b) Volumetric Strain c) Vector Field d) Patch Deformation Profile. 65

Figure 6.7. Determination of Patch Size. 67

Figure 6.8. Control Markers on Side of the Wall. 68

Figure 7.1. Control Markers on Side of the WallQuantification of Slip Plane Geometry with Using Plot Digitizer Program. 69

Figure 7.2. Detection of the Failure Surface Geometry a) as Plotted on the Cumulative Shear Strain Map and b) as Shown with an Illustration. 70

Figure 7.3. Localization of Cumulative Strains in Initially Dense Sand Based on as Obtained from PIV Analyses (a) Vector Field of Deformation, (b) Distribution of Shear Strains (ε_s), (c) Distribution of Volumetric Strains (ε_v). 71

Figure 7.4. Shear Strain Concentration and Failure Surface Evolution with Respect to Rigid Retaining Wall Movement. 72

Figure 7.5. Volumetric Strain Concentration and Failure Surface Evolution with Respect to Rigid Retaining Wall Movement. 72

Figure 7.6. Localization of Cumulative Strains in Initially Loose Sand Based on as Obtained from PIV Analyses (a) Vector Field of Deformation, (b) Distribution of Shear Strains (ε_s), (c) Distribution of Volumetric Strains (ε_v). 73

Figure 7.7. Geometries of Several Active Failure Surfaces Obtained from PIV Analyses and the Corresponding Peak Dilatancy Angles (ψ_p) of the Model Backfill Soils. 74

Figure 7.8. Evaluation of the Influence of Wall Friction on Active Failure Plane Geometry. 75

Figure 7.9. B/H_w Data Obtained from Model Tests Plotted against the Dilatancy Angles (ψ_p) of Respective Backfill Soils. Data Points that Correspond to Different Tests can be Distinguished from the Colors of the Bullets and Their Respective ψ_p Angles. 76

Figure 7.10. Changes in Active Lateral Earth Pressure with wall Movement. . . 77

Figure 7.11. Changes in Active Lateral Earth Pressure Coefficient (K_a) with wall Movement. 78

Figure 7.12. Variation of Dilatancy Angle (ψ_p) within the Backfill with respect to Normalized Failure Surface Width (B/H_w) and Active Lateral Earth Pressure Coefficient (K_a). 78

Figure 7.13. Shape of the Assumed 2^{nd} Order Parabolic Failure Surface and the Depiction of the Geometrical Ratio a_b. 79

Figure 7.14. a_b-tan(ψ_p) Relationship Obtained using the Data Gathered from Retaining Wall Model Study at Active State. 81

Figure 7.15. Comparisons of Calculated Failure Surfaces to the Measured Ones Obtained Using PIV Analyses, Plotted on a Normalized Scale. . . 83

Figure 7.16. Displacement Vector Field for Initially Dense Sand with Different Horizontal Wall Displacement. 85

Figure 7.17. Determination of Slip Plane for Passive Failure state with using Plot Digitizer Software. 85

Figure 7.18. Geometries of Several Passive Failure Surfaces Obtained from PIV Analyses and the Corresponding Peak Dilatancy Angles (ψ_p) of the Model Backfill Soils. 86

Figure 7.19. Variation of Dilatancy Angle (ψ_p) within the Backfill with respect to Normalized Failure Surface Width (B_f/H_w) and Passive Lateral Earth Pressure Coefficient (K_p). 87

Figure 7.20. Changes in Passive Lateral Earth Pressure with wall Movement. . 88

Figure 7.21. Changes in Passive Lateral Earth Pressure Coefficient (K_p) with wall Movement. 88

Figure 7.22. a_b-tan(ψ_p) Relationship Obtained using the Data Gathered from Retaining Wall Model Study at Passive State. 89

Figure 8.1. Step-by-Step Flowchart of Intensity Profile. 90

Figure 8.2. Gray Scale Shear Strain Profile of Backfills with Different Dilation Angles (ψ_p). 92

Figure 8.3. Variation of Measured Shear Band Inclination with $(45+\phi'_p/2)$ and (ψ_p) at Active Failure State. 92

Figure 8.4. The Frequency of Shear Strain Magnitude along the Determined Cross-Sections. 93

Figure 8.5. Shear Strain Intensity Profile along the Cross-Section. 94

Figure 8.6. Shear strain intensity profile along the wall a) tan (ψ_p)=0.09 b) tan (ψ_p)=0.15 c) tan (ψ_p)=0.46. 96

Figure 8.7. Determination of Shear Band Thickness. 97

Figure 8.8. Shear Band Determination Based on Mean Grain Diameter at Active Failure State a) tan(ψ_p)=0.09 b)tan(ψ_p)=0.46. 99

Figure 8.9. Variation of Shear Band Thickness with tan (ψ_p) at Active Failure State. 100

Figure 8.10. Shear Band Formation with respect to Wall Movement i) Strain Maps for Three Different Stages of Test 1.5, 2.25 and 3 mm ii) Intensity Profile of Shear Band on the Proposed Cross-Section. . . 101

Figure 9.1. Influence of Dilatancy on Shear Plane According the Soil Plasticity Theory. 106

LIST OF TABLES

Table 3.1. Properties of Pressure Transducers. 42

Table 3.2. Properties of the Digital Camera. 44

Table 3.3. Properties of the Light. 45

Table 4.1. Specific Gravity Results. 50

Table 4.2. Basic Properties of Akpınar Sand. 52

Table 4.3. The Parameters Required for Calculating Model-Appropriate ϕ'_p and ψ_p for Akpınar Sand. 53

Table 6.1. Programs for using in PIV Applications. 60

Table 8.1. Average Shear Strain Magnitude along the Determined Cross-Sections for Figure 8.2 and Figure 8.4. 94

Table 8.2. The summary of recorded θ values for shear band inclination. . . . 98

Table 8.3. Summary of Recorded (t) Values for Shear Band Thickness. 99

LIST OF SYMBOLS

a	Constant for parabolic active slip plane function
a_b	The ratio of the width of the parabolic failure surface to the width of the planer failure surface at ground surface
b	Constant for parabolic active slip plane function
B	Horizontal distance from the retaining wall to the estimated slip plane at a particular depth z
$B_{1,2,...,n}$	Horizontal coordinates of all points along the experimental slip plane
B_f	Width of the experimental slip plane at ground surface
c	Cohesion
c	Constant for parabolic active slip plane function
c'	Effective cohesion
C_c	Coefficient of curvature
CK_oDC	Conventional drained triaxial compression tests consolidated under K_o conditions
C_u	Coefficient of uniformity
D_i	Grain size corresponding to i % fines
D_r	Relative density
e	Void ratio
e_{max}	Maximum soil void ratio
e_{min}	Minimum soil void ratio
G_s	Specific gravity of soil solids
$H_{1,2,...,n}$	Vertical coordinates of all points along the experimental slip plane
H_w	Wall height
I_D	Relative density (I_D=D_R/100)
K_a	Coefficient of active earth pressure
K_o	Coefficient of earth pressure at rest
K_p	Coefficient of passive earth pressure
L	Size of the search patch in pixels

m_ψ	Unit-independent empirical soil constants for calculating dilatancy angle according to Çinicioğlu *et al.*, (2013)
P	Reaction force
p'_i	Mean effective stress
P_a	Active forces
p_a	Atmospheric pressure
P_p	Passive force
p_{pixel}	Precision error
r	Line-fitting parameter for calculating peak friction angle according to Bolton equation (1986)
R	Reaction on the slip plane
R_{ave}	Average roundness or angularity
S_{ave}	Average sphericity
t	Shear band thickness
u_n	Patch coordinates along the x axis
v_n	Patch coordinates along the y axis
W	Soil weight in failure wedge
z	Vertical coordinate of the estimated slip plane

α	Angle of failure line to horizontal (45+ϕ/2)
γ	Unit weight
δ	Interface friction angle (soil-wall)
δ_c	Critical state oil-wall interface friction (soil-wall)
δ_{mob}	Mobilized internal friction angel (soil-wall)
δ_{pb}	Interface friction angle (plexiglass-wall in this study)
δ_{wb}	Interface friction angle (soil-wall in this study)
ε_s	Cumulative shear strain
ε_v	Cumulative volumetric strain
σ'_x	Horizontal effective stress
σ'_z	Veritical effective stress
θ	Angle of shear band inclination

ψ	Dilatancy angle
ϕ	Internal friction angle
ϕ'	Effective internal friction angle
α_ψ	Unit-independent empirical soil constants for calculating dilatancy angle according to Çinicioğlu *et al.*, (2013)
ϕ'_p	Peak internal friction angle
ψ_p	Peak dilatancy angle
ϕ_r	Residual friction angle

LIST OF ABBREVIATIONS

$ASTM$	American society for testing and materials
$ASCE$	American Society of Civil Engineering
AOI	Area of interest
DIC	Digital images correlation method
FOV	Fraction of the field of view
OCR	Overconsoildation ratio
PIV	Particle image velocimetry method

1. INTRODUCTION

Correct estimation of lateral earth pressures plays a pivotal role in the design of geotechnical structures that retain soil. In practice, classical theories proposed by Coulomb (1776) and Rankine (1857) for active failure and Coulomb (1776), Rankine (1857) and Terzaghi (1943) for passive failure are conventionally used towards the estimation of lateral earth pressures. These theories are based on limit equilibrium methods. In limit equilibrium methods, it is assumed that failure is triggered through the assumed slip plane and that, the shear stress at every point of this slip plane reach a limit shear strength which is controlled by soil shear strength parameters such as cohesion and internal friction angle (Shiau and Smith 2006). However, limitation of the limit equilibrium method is a requirement for the definition of the geometry of the slip plane in advance (Shiau and Smith 2006). It is well known that the fundamental assumption of classical earth pressure theories is that the slip plane formed in the backfill at the ultimate state is a straight line.

In active failure state, experimental evidences (Terzaghi 1936, 1943; Tsagareli 1965; Fang and Ishibashi 1986; Toyosawa *et al.*, 2006, Pietrzak and Lesniewska 2012) and results of numerical modelling studies (Goel and Patra 2008; Benmeddour *et al.*, 2012) suggest that backfill failure plane is nonlinear. This difference between classical theories and real behavior results in computed earth pressures that deviate from actual values. Many researchers made assumptions regarding the geometry of the slip plane with the intention of investigating the lateral earth pressures and their distribution (Matsuzawa and Hazarika 1996; Paik and Salgado 2003). As expected, results obtained in these studies are dependent on the validity of the assumed failure surface geometries. Terzaghi (1936, 1943), investigating the results of model tests, suggested a curvilinear failure surface. On the other hand, Caquot and Kerisel (1948) theoretically assumed log spiral shape. Later, Tsagareli (1965) experimentally investigated fixed walls and proposed curvilinear failure surfaces that can be mathematically defined with a power function. Spangler and Handy (1984) agreeing with Tsagareli on the curvilinear nature of failure surfaces, proposed a parabolic function for their quan-

tification. Toyosawa *et al.*, (2006) conducted centrifuge model tests using a movable earth support apparatus, investigating the influence of mode of wall movement on the geometry of failure surfaces. The results of their study suggested that different modes of wall movement lead to different failure surface geometries. Benmeddour *et al.*, (2012) numerically examined the influence of the presence of a slope on the backfill soil and concluded that the shape of the failure surface is influenced by the location of the slope toe. Pietrzak and Lesniewska (2012) performed model tests to evaluate and observe active failure in granular materials retained by rigid walls using particle image velocimetry method (PIV). Based on the PIV results, Pietrzak and Lesniewska (2012) observed that curvilinear failure wedge generates behind retaining walls. Even though there is no consensus over the general shape of the active failure plane, it is an established fact that its geometry is affected by many factors, such as the properties of the backfill, the imposed stress state, and the mode of wall movement. The parameter that embodies both the mechanical properties of the backfill and the influence of the imposed stress state is dilatancy. Several researchers attempted to account for dilatancy effect by considering the mechanism of arching (Handy 1985, Fang and Ishibashi 1986, Goel and Patra 2008, Nadukuru and Michalowski 2012, Sadrekarimi and Damavandinejad Monfared 2013), but arching is a complex mechanism which is difficult to quantify practically.

In passive failure state, besides Coulomb (1776) and Rankine (1857) theories, Terzaghi (1943) suggested a failure mechanism with a log spiral slip plane. However, the logarithmic spiral earth pressure theory is less popular than the Rankine and Coulomb theories owing to its complexity. Several researchers assumed Terzaghi's proposition to be valid in their studies (Caquot and Kerisel 1948; Kerisel and Absi 1990; Janbu 1957; Sheilds and Tolunay 1973; Kumar and Subba Rao 1997; Shiau *et al.*, 2008, Reddy and Mohapatra 2013). The validity of these theories is still discussed. As a result of an extensive literature survey, it has been noticed that most of the studies over passive earth pressures consider internal friction angle and soil-wall interface friction angle as the only parameters controlling the coefficient of passive earth pressure (Hanna and Khoury 2005). Besides these parameters, only a few researchers investigated the effects of wall movement and overconsolidation ratio (OCR) on passive earth pressures.

However, almost no attempts were made to investigate the influence of dilatancy on passive failure mechanism for cohesionless soils.

Another important issue for understanding the behavior of soil masses behind retaining structures requires investigation of strain localization (Slominski *et al.*, 2006). If the stability condition of a wall changes and initiates displacements, strain will not be homogenously distributed within the soil body, instead it will be confined to a localized area. This localized straining, starting from toe of the wall, results in the formation of a failure wedge. Depending on dilative properties of the backfill, this intense shearing zone can form a distinct or discrete shear band, which provides an estimation of induced loads during failure and also pre-determination of failure wedge geometries. To put in other words, the generation of the shear band in granular soil mass may eventually yield to the formation of a sliding plane.

Thus, in this study attention was focused on the effect of dilatancy on both the geometry and the formation of slip planes under plane strain conditions. Additionally, influence of dilatancy on the slip surface geometry is investigated experimentally for the first time in literature. For this purpose, comprehensive experimental and analytical studies were made. To understand the influence of dilatancy on failure surface geometry, the effect of the mode of wall movement is ignored and only translation type of movements is considered. This is achieved by conducting 1 g small scale retaining wall model tests. Active state is simulated with the model wall translated horizontally away from the backfill and passive state is simulated with the model translated horizontally towards the backfill. The dilatancy angles (ψ_p) of the backfill soils in these tests are estimated as functions of pre-testing conditions using a novel equation proposed by Çinicioğlu *et al.*, (2013). During the experiments, attention was paid to the observation of the formation of slip planes within backfills that have different dilative properties. Geometries of the slip surfaces were obtained using particle image velocimetry (PIV) method. Using PIV, it becomes possible to visualize both the slip surface and its evolution with wall movement. This way, the relationship between dilatancy angle and slip surface geometry could be investigated. Finally, obtained results are used to propose a new method for calculating the shapes of active failure surfaces as

functions of in-situ backfill properties and investigate the shape of passive slip plane depending on the dilative property of the cohesionless backfill.

This thesis first describes the physical model set-up, the properties of the testing material and then explains how the peak friction (ϕ'_p) and peak dilatancy (ψ_p) angles of the model backfill soils are calculated. Following, method for the identification of backfill deformations is introduced. According to the results of model tests, generated slip planes are identified based on the results of PIV analyses and the influence of dilatancy on failure surface geometry is investigated. Then, an equation is proposed to determine the slip surface geometry for active states as a function of dilatancy angle (ψ_p). Validity of the proposed equation is evaluated by comparing the estimated slip plane geometries with those obtained from model tests. Following that, the effect of dilative behavior on passive slip plane is explained according to model test results and particle image velocimetry (PIV) method analyses. After that, the results of shear band formation and progressive failure mechanism for the case of the active state will be given. Based on the obtained observations, variations of strain behind the model wall are quantified using both shear and volumetric strain intensity profiles. Finally, obtained results and proposed relationships are discussed.

2. LITERATURE REVIEW

2.1. Active Earth Pressure and Slip Plane Geometry

Accurate estimation of lateral earth pressures is necessary for designing geotechnical structures that are both safe and economic. Classical earth pressure theories proposed by Coulomb (1776) and Rankine (1857) based on the limit equilibrium method are conventionally used in practice for the design. Besides, different theories can be found in literature for calculating active earth pressures (e.g. Caquot and Kerisel 1948, Dubrova 1963, Wang 2000, Paik and Salgado 2003, Goel and Patra, 2008). All theoretical solutions are sensitive to the internal friction angle. However, none is capable of closely capturing the effect of dilatancy visualized in experiments.

When retaining wall moves away from the backfill, shearing behavior localizes and a sliding plane is formed which is referred to as "active slip plane". In literature, slip planes are also called slip surfaces, failure surfaces, failure planes, shear surfaces or shear planes. Both Rankine's and Coulomb's theories which are based on limit equilibrium have the same basic assumption that the slip plane is a straight line. Besides, limit equilibrium method and limit analysis theory assume associated flow, which restrict the direction of the plastic flow such that $\psi = \phi$ (Shiau and Smith 2006). However, the effect of dilative behavior on slip plane has never been investigated in detail by conducting model tests coupled with carefully employed visualization techniques.

Little attention has been paid to study the geometry of slip planes at active state in literature and it has never been studied solely. Several researchers criticized the planarity of the slip plane, but few of them have carried out investigations to identify the shape of the active failure surface realistically.

2.1.1. Coulomb Theory

Coulomb (1776) is considered to be the first scientist to develop a theory to predict the earth pressure coefficients. He suggested a mathematical solution for the calculation of magnitude of earth pressure behind retaining walls by considering soil-wall friction angle (δ). In theory, the stability of a wedge of soil between a retaining wall and a trial failure plane are considered and the generated force between wedge and wall surface is calculated by the equilibrium of forces acting on the wedge. Coulomb (1776) assumed that the generated failure surface is planar, as shown in Figure 2.1. This is the main disadvantage of the Coulomb theory. In addition to this assumption, Coulomb (1776) also assumed that:

- Soil mass is in isotropic conditions and homogeneous.
- Soil has both internal friction and cohesion.
- Failure is a plane strain problem.
- The failure wedge is a rigid body undergoing translation.
- The friction resistance is distributed uniformly along the rupture surface and soil-to-soil friction coefficient is $f = tan\phi$.
- Friction forces generate between the wall and the soil.

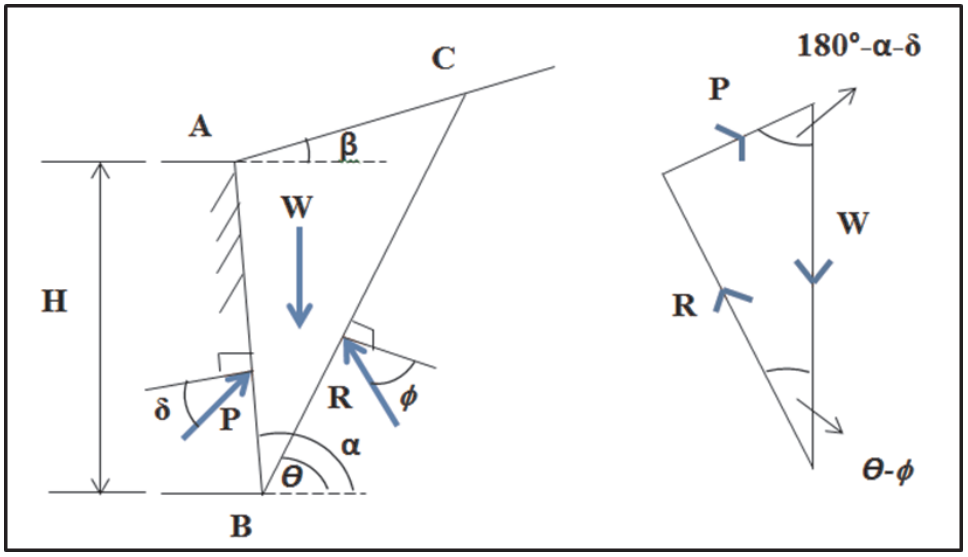


Figure 2.1. Active Case with c = 0, Coulomb Theory (After Craig 2004).

In Coulomb's theory, the soil wedge is in equilibrium under the actions of its own weight (W), the reaction force (P) due to the soil wall interface friction (δ) and the reaction on the slip plane (R). If the vertical retaining structure moves horizontally (or tilts), the soil mass expands. Accordingly, at the state when soil shear strength is fully mobilized; the direction of R makes an angle ϕ with the normal of the planar failure plane (Craig 2004). The directions of the three forces and the magnitude of W are known so that the magnitude of P can be determined from the triangle of forces as shown in Equation 2.1:

$$P_a = \frac{1}{2} K_a \gamma H^2 \tag{2.1}$$

In which, P_a, K_a, and γ are active force, active earth pressure coefficient, and unit weight of the soil, respectively.

$$K_a = \left[\frac{\sin(\alpha - \phi)/sin\alpha}{\sqrt{\sin(\alpha + \delta)} + \sqrt{\frac{\sin(\phi+\delta)\sin(\phi-\beta)}{\sin(\alpha-\beta)}}} \right] \tag{2.2}$$

In Coulomb theory, the point of application of the total active thrust is not given. However, generally it is assumed to act at a distance of 1/3H above the base of the wall (Craig 2004).

Experimental evidence suggests that, the slip plane is curved near the bottom of the wall in both active and passive failure states. But according to the Coulomb theory, slip planes are assumed to be plane in each case (Craig 2004). However, in the active case, the curvature is slight, so error is small and also negligible. This is also true for the values of interface friction, δ, less than $\phi/$ 3 in passive case, but for higher values of δ the errors become large (Craig 2004).

2.1.2. Rankine Theory

William John Macquorn Rankine (1857) proposed a theory to calculate lateral earth pressures with considering soil in a state of plastic equilibrium in the theory and using essentially the same assumptions as Coulomb. In Rankine's theory, the different thing from the Coulomb's theory is that there is no interface wall friction or soil cohesion. Shear failure occurs along a plane at an angle of $45^o+\phi/2$ to the major principal plane as shown in Figure 2.2. According to Rankine theory, the active earth pressure (P_a) is expressed as:

$$P_a = K_a \gamma z - 2c\sqrt{K_a} \tag{2.3}$$

In which,P_a,K_a, and c are active force, earth pressure coefficient, and cohesion of the soil respectively.

$$K_a = \frac{1 - \sin\phi}{1 + \sin\phi} \tag{2.4}$$

If the horizontal stress becomes equal to the active pressure, the soil is in the active Rankine state.

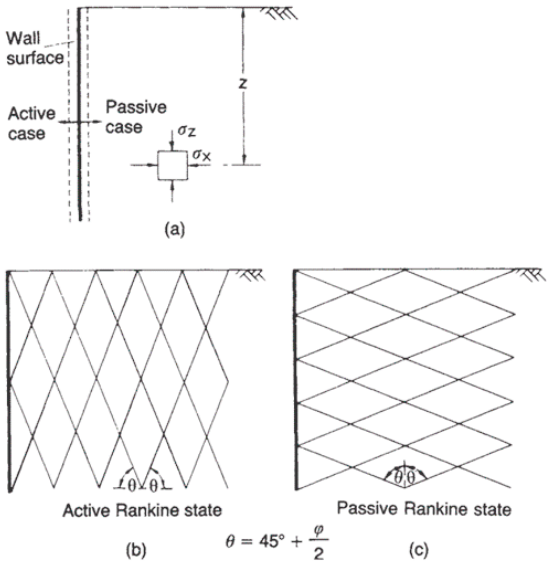


Figure 2.2. Active and Passive Rankine States (Craig, 2004).

2.1.3. Others Researchers

Terzaghi (1936) carried out a series of experiments to investigate the influence of the mode of wall movement on earth pressures and reported that the change in wall pressure from at-rest to active or passive state is a function of the wall movement. Moreover, Terzaghi claimed that resulting slip planes are approximately parabolic due to arching effects. The term of arching was expressed by Terzaghi (1936) as the stress redistribution process by which stress is transferred around a region of soil mass, which as a result reduces the stresses on the soil mass. Following that Terzaghi (1943) continued his study on earth pressures and suggested that the shape of generated failure surface at active state depends on both soil-wall interface friction angle (δ) and the yielding mode of retaining wall. According to his study, the slip surface is a plane if δ=0, but for a rough wall ($\delta \neq$0), the slip surface formed as a curve irrespective of the yielding mode. The same results were obtained by Fang and Ishibashi (1986). Terzaghi (1943) also state that when the wall rotates about the base, the failure surface is formed as a curved shape near the base of the wall and planar near the top, as shown in Figure 2.3. When the wall rotates about the top, the failure surface generates as a curved shape and intersects the horizontal surface of the backfill at right angles. If the wall yields horizontal translation, the slip plane forms with a more complex shape.

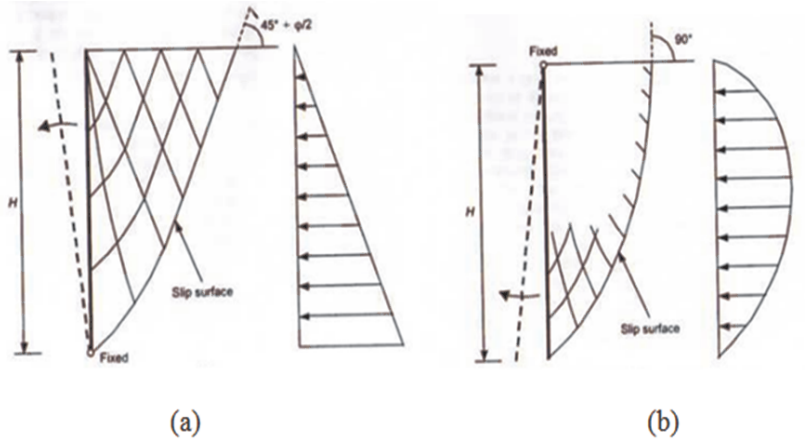


Figure 2.3. Generated Failure Surface within the Backfill Resulting from a) Rotation about the Base b) Rotation about the Top (Paik and Salgado, 2003).

Tsagareli (1965) carried out experimental study to determine the character of the slip surface with fixed walls and proposed curvilinear failure surfaces that can be mathematically defined with a power function. He proposed Equation 2.5 to determine the slip surface as follows:

$$Y = C(3.6\phi + 0.5)^{\frac{X}{C}} \tag{2.5}$$

where ϕ is the angle of internal friction of the earth in radians; C is a coefficient having the dimensions of length. Based on the experimental results, Tsagareli (1965) concluded that slip wedge has a curvilinear boundary. Additionally, the slip line is the same for different wall heights (Figure 2.4) and can be calculated with using proposed equation (Tsagareli 1965).

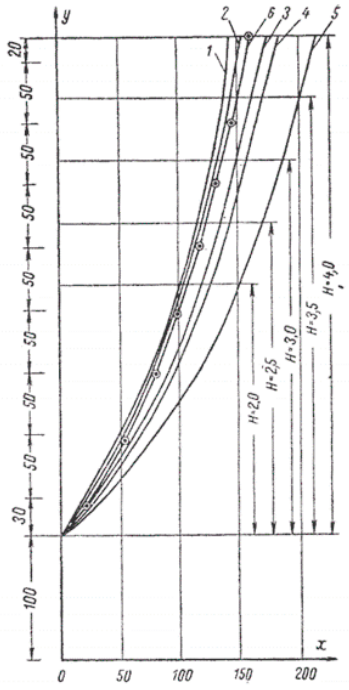


Figure 2.4. Slip Surfaces Plotted from Equation 2.5 and Experimental Data a) $\phi = 40^o$; b) $\phi = 37^o$; c) $\phi = 32^o$; d) $\phi = 30^o$; e) $\phi = 25^o$; f) Experimental Curves for $\phi = 37^o$.

Spangler and Handy (1984) suggested that the critical slip plane for a retaining wall is curvilinear in nature. However, the researcher reported that the use of a planar

slip plane would not yield very large errors in calculation of lateral earth pressures.

Fang and Ishibashi (1986) investigated the distribution of active earth pressure against retaining wall rotating about its top. Based on the results, Fang and Ishibashi (1986) indicated that the distribution of active earth pressure against retaining wall rotating about its top is nonlinear and the non-linearity results from the soil arching and the magnitude of the arching stress increased with increasing density of soil.

Matsuzawa and Hazarika (1996) made a numerical study to understand the influence of wall movement mode on the distribution of active earth pressures (Figure 2.5) by finite element modelling method and assuming an elasto-plastic soil behavior. Based on the analysis, Matsuzawa and Hazarika (1996) claimed that the wall movement modes govern the generation of active failure pattern. Additionally, resultant active earth pressure as well as its application point depends on the wall movement modes and soil density.

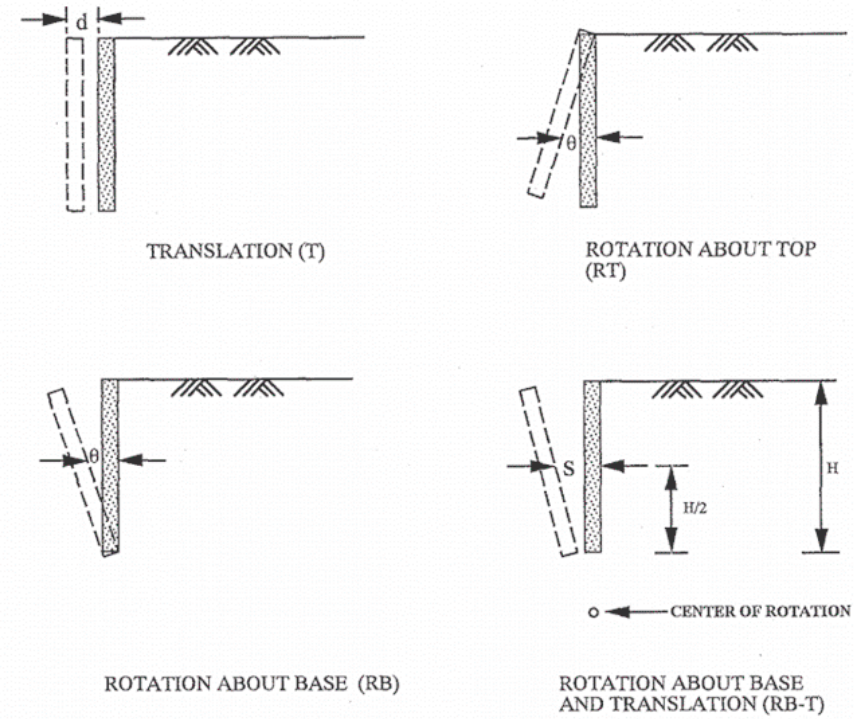


Figure 2.5. Modes of Wall Movement (Matsuzawa and Hazarika, 1996).

Paik and Salgado (2003) conducted a parametric study with considering the arch-

ing effects in the calculation of active earth pressures on a horizontally translating rigid wall and tried to propose a new formulation which satisfactorily predicts both the earth pressure distribution and the lateral active force on the translating wall. Paik and Salgado (2003) suggested that the distribution of active earth pressure behind the wall is non-linear and the earth pressure distribution differs depending on the mode of wall movement. This is due to arching effects in the retained soil, which results from the frictional resistance between the wall and the soil.

Toyosawa *et al.*, (2006) carried out a series of centrifuge tests to investigate the redistribution of earth pressures during the deflection of the wall by using an in-flight movable earth support apparatus Figure 2.6 which controls the deformation of the model wall under a 50 G centrifugal field, to simulate various types of wall deformations. Dry Toyoura sand (D_{50}=0.16 mm) was used in their study. Sub-tracking method, which is image processing technique, was used to visualize the deformation within the backfill. Toyosawa *et al.*, (2006) observed that failure surface is different for each modes (rotation about base, rotation about top and translation) and not always planar, and also the deformation progressed along this failure surface. Furthermore, Toyosawa *et al.*,(2006) suggested that the mode of wall movement and possibly arching action influence the redistribution of earth pressure.

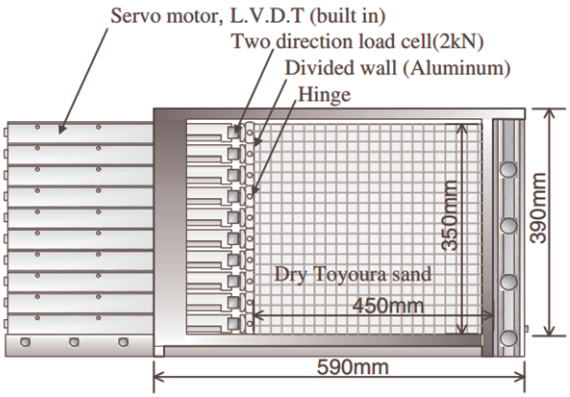


Figure 2.6. Movable Earth Support Apparatus (Toyosawa *et al.*, 2006).

Goel and Patra (2008) investigated active earth pressure distribution on rigid retaining walls by considering arching effects and critical failure surface shape by using

various configurations of critical failure surface and arch shapes, namely planar failure surface with a parabolic arch and parabolic failure surface with a parabolic arch. Based on the results, Goel and Patra (2008) claimed that predictions based on the assumption of planar failure surface with parabolic arch shapes are closest to the experimental values.

Loukidis and Salgado (2012) made a numerical study by using finite element method for understanding the evolution of the active earth pressures behind a gravity retaining wall and the shear patterns developing in the backfill and foundation soil. Loukidis and Salgado (2012) suggested that the inclinations of the shear bands are affected by the relative density (I_D).

Benmeddour *et al.*, (2012) conducted a numerical study with using Fast Lagrangian Analysis of Continua code (FLAC) in order to observe the influence of backfill inclination, soil-wall interface friction angle (δ) and proximity of a slope on earth pressure coefficients. Based on the results, the researchers concluded that the shape of the slip plane is affected by the ratio of the slope toe located at variable distances and wall height.

Nadukuru *et al.*, (2012) made a numerical study using discrete element method (DEM) to investigate arching effect with modes of wall movement (rotation about the top, rotation about the base and translation) in cohesionless backfill behind retaining walls. Nadukuru *et al.*, (2012) concluded that strain along the slip surface varies with rotational modes of wall.

Khosravi *et al.*, (2013) performed an experimental model study to investigate arching effects behind the wall in granular materials at active state. Rigid retaining wall was subjected to horizontal translation and the variation of lateral earth pressure was measured with using miniature pressure cells. Particle image velocimetry (PIV) was employed to visualize the deformation within the backfill through a transparent container. Air-dried silica sand No. 8 with a relatively fine particle size (D_{50}= 0.10 mm) was used as sample material. Khosravi *et al.*, (2013) instrumented a physical

model system consisting of an acrylic container (400x400x200 mm^3) with the particular configuration shown in Figure 2.7. The researchers monitored that the pattern of the failure zone behind the wall changed with wall displacement and become clearer. However, as the wall displaced, no obvious change in soil pattern could be observed and the failure zone could obviously be distinguished from the stationary zone. Additionally, Khosravi *et al.*, (2013) reported that the experimental results obtained from model study showed good agreement with arch-action-based theories, therefore arching effects the deformation in backfill behind the retaining wall at active translation mode.

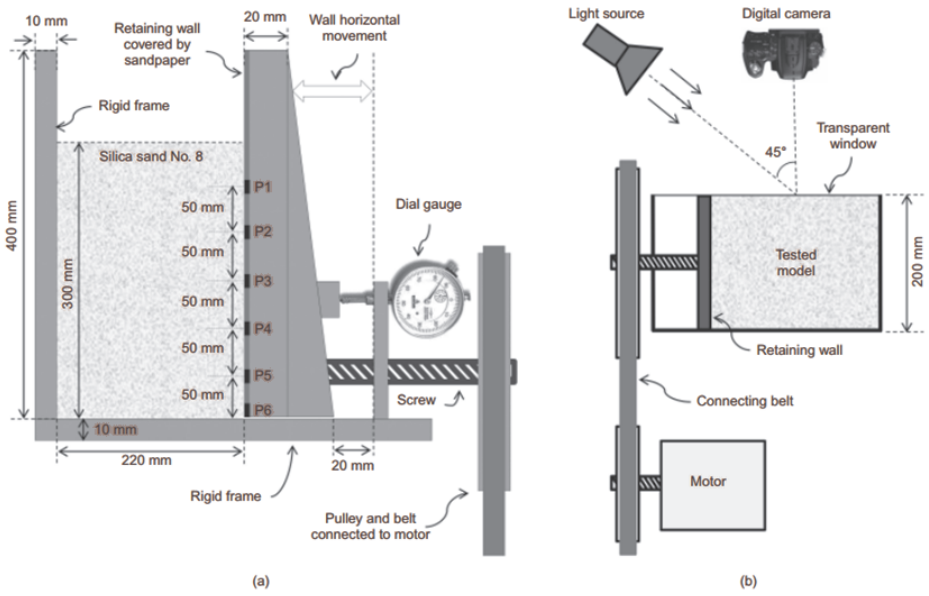


Figure 2.7. Schematic Diagram of Retaining Wall Model: (a) Container Geometry and Moving Scheme; (b) Experimental Set-up (plan) (Khosravi *et al.*, 2013).

2.2. Passive Earth Pressure and Slip Plane Geometry

When the vertical retaining structure moves horizontally or tilts towards to a backfill, passive earth pressures generate within the soil mass, therefore horizontal stresses occur within the backfill. These pressures take a crucial role on a wide range of geotechnical engineering problems. They resist lateral movement of structures and it provides a stabilizing force, especially for the retaining walls. In some cases, the passive earth pressure can cause detrimental effects on the performance of retaining structures. Therefore, correct calculation of passive earth pressure has an important effect in soil-

structure interaction. The Coulomb (1776), Rankine (1857) theories are widely used in engineering practice to calculate passive resistance because of simplicity. The log spiral theory proposed by Terzaghi (1943) has been known to offer a more accurate estimation of passive earth pressure, but due to its complexity engineers would not prefer to use it in design. These theories are based on limit equilibrium methods and these methods are based on the assumption that failure is triggered along an assumed slip plane. The shear stress at every point on this slip line reach a limit shear strength that controlled by shear strength parameters such as cohesion and friction (Shiau and Smith 2006). Also, it is known that passive earth pressure is related to the shearing resistance of soil along the slip plane (Fang *et al.*, 2002). Limitation of the limit equilibrium method is required to identify the form of the slip plane (Shiau and Smith 2006).

In the literature, mode of wall movement, cohesion and friction, interface friction and adhesion, and structure shape are considered as parameters that affect the passive failure mechanism (Duncan and Mokwa 2001). It is well known that classical limit equilibrium method assumes an associated flow rule, which restrict the plastic flow direction such that $\psi = \phi$ (Shiau and Smith 2006). In non-associated materials, dilation angle cannot be greater than friction angle. To be more precise, dilation angle is smaller than internal friction angle in soils. That's why, the calculated passive resistance is overestimated due to the usage of associated flow (Shiau and Smith 2006). However, the effect of dilatancy on slip plane geometry at passive failure state has not been investigated with experiments in previous studies.

2.2.1. Coulomb Theory

Coulomb (1776) is considered to be the first scientist to develop a theory to predict the passive earth pressure coefficient. He suggested a mathematical solution for the calculation of magnitude of passive earth pressure behind the retaining walls. Friction between the wall and adjacent backfill is taken into account in Coulomb's theory (Craig 2004). Coulomb (1776) considered the stability of a wedge of soil between a retaining wall and a trial failure plane. In this theory, the generated force between wedge and wall surface is calculating the equilibrium of forces acting on the wedge with the assumption

that the generated failure surface is planar. The main disadvantage of the Coulomb theory stems from this assumption.

In the passive case, from Figure 2.1, the reaction P acts at angle δ above the normal to the wall surface (or δ below the normal if the wall was to settle more than the adjacent soil) and the reaction R at angle ϕ above the normal to the failure plane. In the triangle of forces, the angle between W and P is 180^o-α+δ and the angle between W and R is θ+ϕ Figure 2.1 (Craig 2004). The total passive resistance, equal to the minimum value of P, is given by;

$$P_p = \frac{1}{2} K_p \gamma H^2 \tag{2.6}$$

where;

$$K_p = \left[\frac{\sin(\alpha + \phi)/sin\alpha}{\sqrt{\sin(\alpha - \delta)} - \sqrt{\frac{\sin(\phi+\delta)\sin(\phi+\beta)}{\sin(\alpha-\beta)}}} \right] \tag{2.7}$$

In which,P_p,K_p and γ are passive force, passive earth pressure coefficient, unit weight of the soil, respectively.

However, Craig (2004) discussed that due to the friction between the wall and the soil, the shape of the slip plane is curved near the bottom of the wall in both the active and passive cases as shown in Figure 2.8, but in the Coulomb theory the slip plane is assumed to be planar in each case. In the active state, the curvature is slight and the error is relatively small and might be ignorable. This is also correct in the passive case for values of δ less than ϕ / 3. But for the higher values of δ, the Coulomb theory overestimates the passive resistance due to a curved portion of the slip plane (Fang *et al.*, 2002; Craig 2004; Cole and Rollins 2006, Benmeddour *et al.*, 2011).

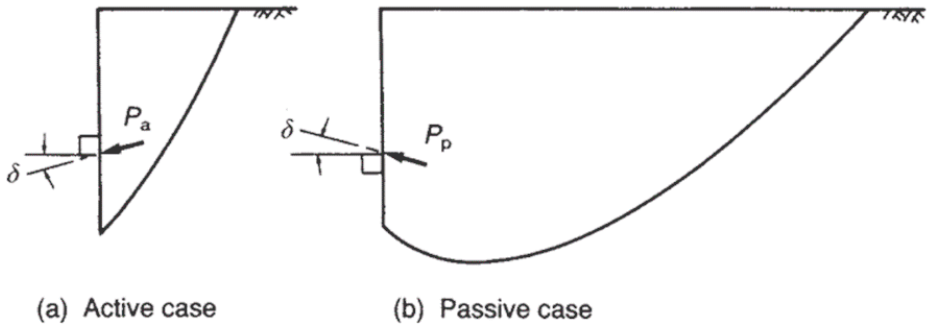


Figure 2.8. Curvature due to the Wall Friction (Craig 2004).

2.2.2. Rankine Theory

Rankine (1857) offers a simple prediction of the peak passive earth pressure. Rankine's method of calculating the passive pressure considered soil in a state of plastic equilibrium and used essentially the same assumptions as Coulomb. In particular, Rankin (1857) assumed that there is no friction between wall-soil interface (δ= 0) or soil cohesion. According to Rankine theory, the active effective stress is expressed as:

$$P_p = K_p \gamma z + 2c\sqrt{K_p} \tag{2.8}$$

where;

$$K_a = \frac{1 + \sin\phi}{1 - \sin\phi} \tag{2.9}$$

in which, P_p, K_p, γ, ϕ and c are passive force, passive earth pressure coefficient, unit weight of the soil, friction angle and cohesion, respectively.

In most cases, the assumption of smooth wall (δ= 0) is not accurate. Therefore, in these cases, the prediction obtained by employing Rankine passive pressure theory tends to under-estimate the actual available resistance (Kramer 1996, Terzaghi *et al.*, 1996).

2.2.3. Terzaghi Theory

Terzaghi (1943) modified the Coulomb earth pressure theory and suggested logarithmic spiral earth pressure theory. According to this log spiral theory, the failure surface consists of two parts, logarithmic spiral and straight plane as shown in Figure 2.9. However, log spiral method is less widely used than the Rankine and Coulomb theories due to its complexity, but it offers more accurate results of passive pressures for conditions where the interface friction angle between soil and backfill is more than about 40% of the angle of internal friction (Duncan and Mokwa 2001).

Terzaghi solution provides lower K_p values than Coulomb's for wall-soil interface friction values $\delta > \phi/3$. The log spiral shape of the failure plane has generally been borne out by experiments, and hence the Terzaghi solution is generally preferred over that of Coulomb's.

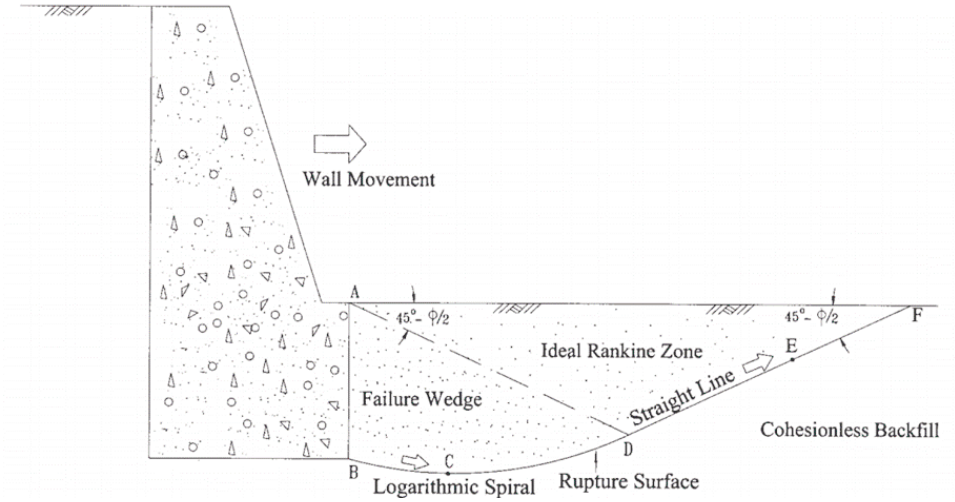


Figure 2.9. Log Spiral Failure Mechanism after Terzaghi (Fang *et al.*, 2002).

2.2.4. Other Researchers

Caquot and Kerisel (1948) proposed a solution for passive earth pressure acting on a wall. They showed that the mobilized internal friction angel (δ_{mob}) depends on the types of wall movement and suggested charts for the passive earth pressure coefficient (K_p) based on the curved slip plane for cohesionless backfill for the case of $\phi' = \delta$.

Brinch-Hansen (1953) carried out an experimental study on the failure planes under different types of wall movements. For this purpose, a small scale model with a wall having dimensions of 15 cmx15 cm was instrumented. Based on the results; the researcher reported differences in the shape and size of the slip wedges under different wall displacements and with different wall frictions.

Narain *et al.*, (1969) performed an experimental study in order to determine the slip plane formed behind a retaining wall which rotates around its bottom or top and moves translation mode for loose and dense backfill. He concluded that the magnitude of the earth pressure varied with the type of the wall movement. The maximum values of passive earth pressure were reached when the wall was rotated around its bottom and the minimum values were reached when the wall was rotated around its top.

Shields and Tolunay (1973) adopted Terzagi's Log Spiral failure mechanism and used the method of slices (Figure 2.10) to compute the values of passive earth pressure.

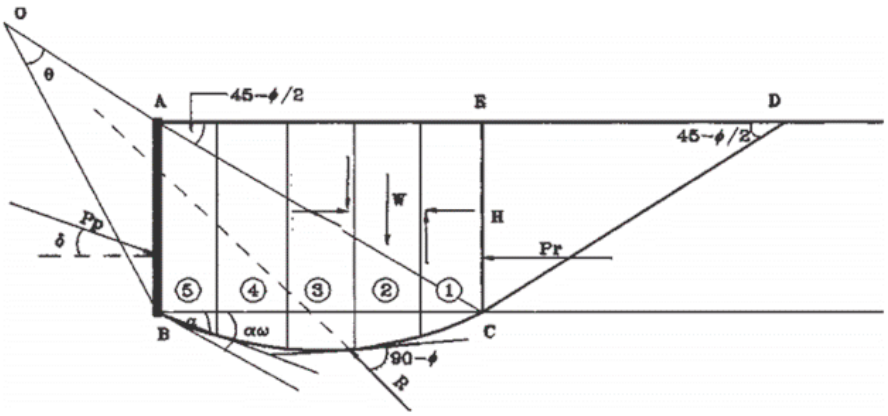


Figure 2.10. Method of slices (After Shield and Tolunay 1973).

Rowe and Peaker (1965) instrumented an apparatus to investigate the passive earth pressure generated within the cohesionless backfill on a vertical wall moved by translation against a horizontal fill. Based on the test results, Rowe and Peaker (1965) observed that the soil-wall interface friction (δ) changed in relation to the rate of wall displacement. Additionally, they suggested that the geometry of the failure surface occurs as the result of progressive deformation and volume changes throughout the

mass up to the peak wall load. Also, they stated that the influence of the wall movement on the soil's friction angle (ϕ) and the soil-wall interface friction (δ) should be taken into account in the use of all the theories.

Kumar and Subba (1997) suggested charts to calculate passive earth pressure coefficients based on an assumed slip plane consisted of a plane parts and a logarithmic spiral. According to this study, the slip plane inclination depends on the internal friction angle, vertical inclination of the wall, and the friction between soil and the wall. Additionally, the researchers asserted that the slip plane angle respect to the horizontal controls the curvature of the slip plane.

Duncan and Mokwa (2001) made an investigation to understand the factors that control the passive earth pressures and to discuss the strengths and weaknesses of the theories that are used to calculate passive earth pressures. According to this study, the passive resistance of the soil depends on the amount and direction of the wall movement, cohesion and friction of the soil, interface friction and shape of the structure. Based on the experimental results and theoretical studies, they concluded that the log spiral theory provides an accurate result for computing ultimate passive pressures.

Fang *et al.*, (2002) performed model tests with different relative densities to investigate distribution of passive earth pressure and variation of passive earth pressure coefficient in granular backfills. The movable model retaining wall was instrumented (Figure 2.11) for investigation. They used Air-dry Ottawa sand for backfills and backfills were prepared by air pluviation method for loose backfill and a vibratory compactor for dense backfill. Based on the results, they suggested that the passive soil thrust reaches a constant value when wall displacement (S/H) exceeds the value of 0.12 regardless of the initial density of backfill. Addition to this, Fang *et al.*, (2002) inferred that soils along the slip plane had reached the critical state, and the shearing strength on the plane could be properly represented with the residual ϕ_r angle. Also, the researchers recommended that one should consider the dilation and the strength reduction of dense backfill when calculated passive pressures.

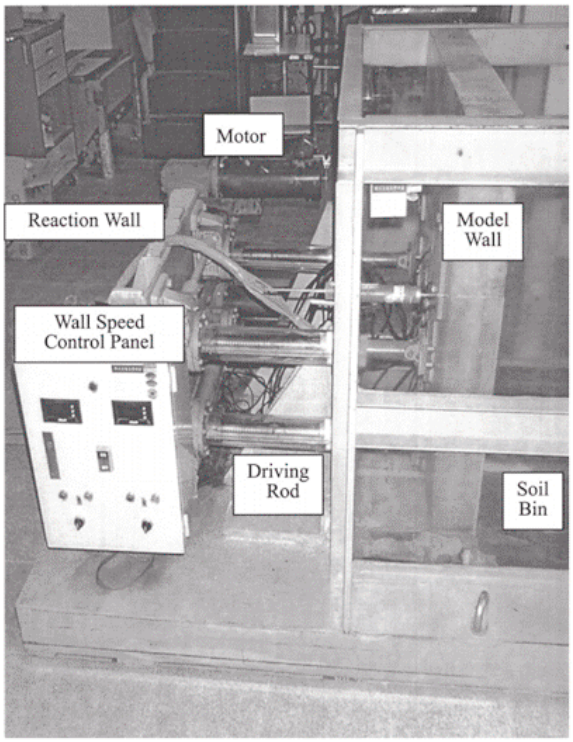


Figure 2.11. Model Retaining Wall (Fang *et al.*, 2006).

Hanna and Khoury (2005) carried out an experimental study to observe the effect of overconsolidation ratio on passive earth pressures. For this purpose, a prototype model of a vertical rough wall and retaining horizontal backfill was instrumented. Well-graded sand was used in this investigation as backfill material. Overconsolidated sand was obtained by placing the sand in thin layers and compacting each of them mechanically for a period of time when needed. Experiments were conducted with both the homogeneous overconsolidated sand, and overconsolidated sand backfill overlying the deep sand layer. In analysis, they employed Shields and Tolunay failure mechanism consisting of two parts: logarithmic spiral and plane portions. According to results, they asserted that, overcosolidation ratio (OCR) and the soil condition below the founding level influence the passive earth pressure coefficient.

Shiau and Smith (2006) made a parametric study to investigate the influence of using associative ($\psi = \phi$) and non-associative ($\psi \leq \phi$) flow rules on the magnitude of the passive earth pressure coefficient. For this purpose, Shiau and Smith (2006) used the commercial finite difference computer code (FLAC) for the numerical simulations

to calculate the passive earth pressures acting on a retaining wall. The constitutive model was used to represent soil behavior included the elastic-perfectly plastic Mohr-Coulomb model with the application of both associative and non-associative flow rules. They considered the boundary effect, associated and non-associated flow rule, and the effect of soil-wall friction in their study. Shiau and Smith (2006) concluded that using a non-associated flow rule yields more accurate results with what may be monitored in reality. The researchers also noted that the use of associated flow overestimates the passive resistance since the dilation angle would range between zero and the internal friction angle. Based on the results, they reported that the dilation angle was shown to have a significant effect on the calculated ultimate passive resistance of the backfill.

Tejchman *et al.*, (2007) focused on influence of initial density of cohesionless soil on evolution of passive earth pressure and the formation of shear zones in a dry sand body behind a retaining wall. The evolution of shear localization, dilatancy and contractancy, micro-rotation and earth pressure behind a very rough and rigid retaining wall undergoing a horizontal translation against the backfill under plane strain condition was numerically investigated using the finite element method and a micro-polar hypoplastic continuum model. At the end of the investigation, they concluded that initially dense material experiences strong dilatancy during passive wall translation within the localized zones. At this point, dilatancy is accompanied with a reduction of the resulting earth pressure. Same conclusion also obtained by Lade (2002). In turn, compaction of the material is observed in the case of the initially loose material. Tejchman *et al.*, (2007) also reported that the maximum passive earth pressure strongly depends on the magnitude and distribution of the initial density, pressure level and mean grain diameter. The peak friction angle for an initially dense material and a low pressure level can be very high which leads to a high maximum earth pressure. After the peak, the earth pressure is reduced with continuous passive wall translation. For the initially loose material, the earth pressure increases during passive wall translation and shear localization takes place without a reduction of the resulting earth pressure. The researchers also asserted that the distribution of the initial void ratio slightly affects the geometry of shear zones (thickness and inclination angle).

Wilson and Elgamal (2010) conducted large scale model tests and made a numerical simulation to investigate the passive earth pressure generated behind the wall. The schematic view of their model system is shown in Figure 2.12. They carried out two large scale passive earth pressure tests with dense sand under low interface friction angle (δ) conditions with using soft foam in backfill. These foams were used to monitor the shape of the slip wedge. For the backfill material, they used sand with non-plastic silt and fine gravel. Additionally, they made FE simulations for the cases of larger δ. Based on these studies; they suggested that passive failure wedge was occurred to be fully formed near the peak measured load and the shape of the failure wedge was monitored as a triangular for low δ shown in Figure 2.13.

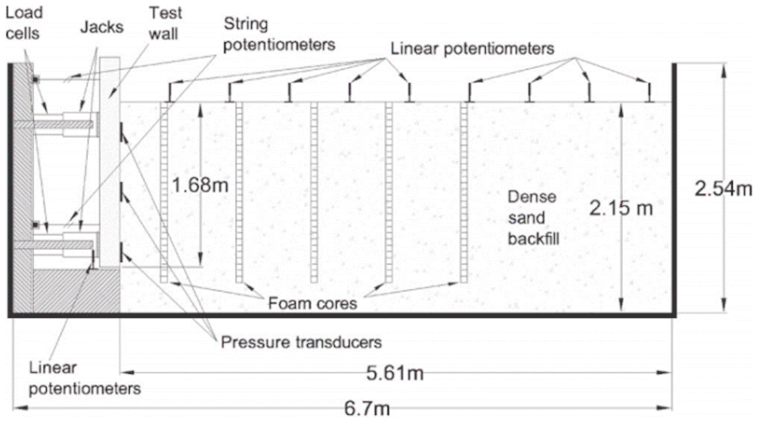


Figure 2.12. Schematic Elevation View of Passive Earth Pressure Experiment with Instrumentation Layout (Wilson and Elgamal 2010).



Figure 2.13. Broken Foam Cores Showing Shape of Failure Wedge (Wilson and Elgamal 2010).

2.3. Strain Localization and Visualization

Observing the mechanism of the formation of shear zones gains importance since first they act as a precursor to ultimate soil failure and second for a realistic estimation of forces transferred from the surrounding granular body to the structure, especially in the problems of earth retaining structures.

Strain localization in deforming granular geomaterials has been intensively investigated by many researchers both numerically and experimentally. In spite of numerous researches conducted on the problem of earth pressure on retaining walls over more than 200 years, there is still a gap between theoretical solutions and experimental results due to the complexity of the deformation field in granular soil mass near the wall caused by localization of deformations. However, recent research studies utilizing novel image analysis techniques provide valuable insight into strain localization phenomenon. These investigations contribute to our measured and quantified strain localization in the laboratory. Shear band formation is an outcome of the microstructural characteristics of soils, and thus evolution of shear band, its thickness, and also distribution of volumetric and shear strains inside it play a key role on the mobilization of the failure mechanism and so slip plane formation. Furthermore, formation of shear zones control a global post-peak response, so it requires to pay attention to understanding the nature of granular geomaterials behavior within shear zones in order to identify the softening and critical state material response at the macro level (Widulinski *et al.*, 2011).

Experiments have been carried out on granular media by several researchers to identify appearance and patterns of shear bands. Most of these studies were concentrated on localization characteristics, such as shear band thickness, inclination and orientation. On the other hand, some studies investigated the influences of important engineering properties of soils; mean grain diameter, pressure level, initial void ratio, direction of deformation, grain roughness and grain size distribution. Present study makes a significant contribution to identify the shear zones formation and to monitor distributions of shear bands, however, merely few studies have concentrated on quantification of shear band thickness and inclination angles appeared behind translated

rigid wall at active failure state. Unfortunately, shear strain localization could not quantify at the passive failure state in this study due to steel braces located on the plexiglass side walls. Future studies will be conducted by modifying the testing tank without steel braces and then, the strain on slip plane would be quantified.

In the literature, Coulomb (1775) was first mentioned the concept of shear zones in his study. He carried out an investigation to understand the occurrence of shear zones during the generation of earth pressure.

Rowe (1969) performed an experimental and theoretical investigation in order to show that the surface friction affects the shear strength and dilatancy, the way the particles packed. These findings support the idea that the localization of strain will be influenced by the shape of the particles "packing" and by the surface roughness that controls the friction.

Desrues and Hammad (1989) conducted a series of experiments to observe the effects of mean stress level on shear band in sand by using a plane strain biaxial apparatus, as shown in Figure 2.14. They used two types of sand in experiments namely; the Hostun RF sand (D_{50}=0.32, uniformly graded) and the Manche sand (calcareous sand). To measure the displacement fields in the specimen, false relief stereophotogram metric method was used. For this purpose, photographs were taken during the test and analyzed for determining shear band locations and directions in the soil mass. At the end of the experiments, they suggested that shear band localization is affected by the confining pressure level and the localization is retarded by increasing mean stress level and by decreasing sample density. Additionally, Desrues and Hammad (1989) asserted that shear band also formed in materials which shows contracting behavior in terms of volume change.

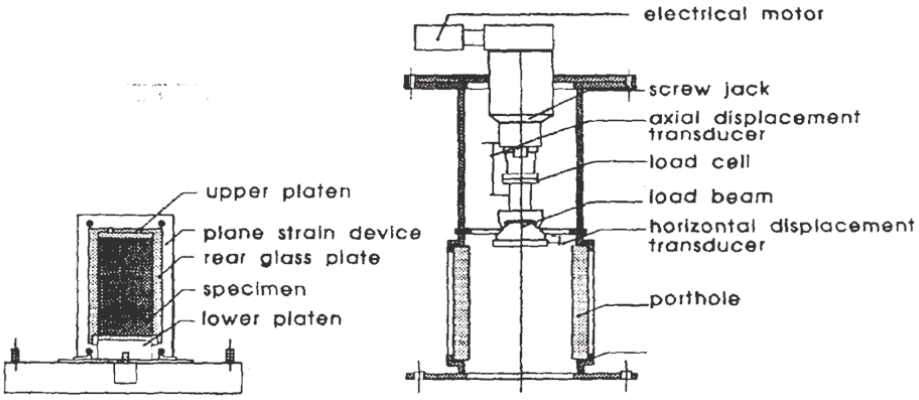


Figure 2.14. Biaxial Apparatus (Desrues and Hammad, 1989).

Lesniewska and Mroz (2001) performed model experiments to investigate the evolution of shear band systems in sand retained by flexible wall. The goal of their study was to provide a simple analysis aimed to explain the development of shear band pattern for the case of a granular material retained on one side by a flexible wall. To detect the shear bands in granular backfill X-rays visualization technique was used. Lesniewska and Mroz (2001) used Leighton Buzzard sand in all tests which is rounded coarse quartz sand. Their model constitutes a modified version of an extension of the classical Coulomb wedge analysis by assuming that soil parameters are varying during the deformation process and the initial configuration at which limit equilibrium occurs evolves toward a new equilibrium configuration. With this model, they provided to discuss the transition between the states of continuous and localized deformation observed in reality and to understand the possible role of flexible wall on shear band forming.

Nübel and Weitbrecht (2002) visualized the localization in grain skeletons with particle image velocimetry (PIV) method in plane strain conditions. They are one of the first researchers used PIV method in geotechnical experiments. Nübel and Weitbrecht (2002) made an experimental study that can be used for the verification and physical interpretation of numerical models that made for investigation of shear band formation. Obtained results by utilizing PIV method are shown in Figure 2.15. At the end of the study, they stated that density fluctuations can be monitored much better than X-ray

method. The underlying reason for this conclusion is that PIV method observes only the grains in direct conjunction with the glass wall. In addition to these, they suggested that many applications are possible with using PIV method, such as velocity field and wave propagation can be monitored with using high speed cameras.

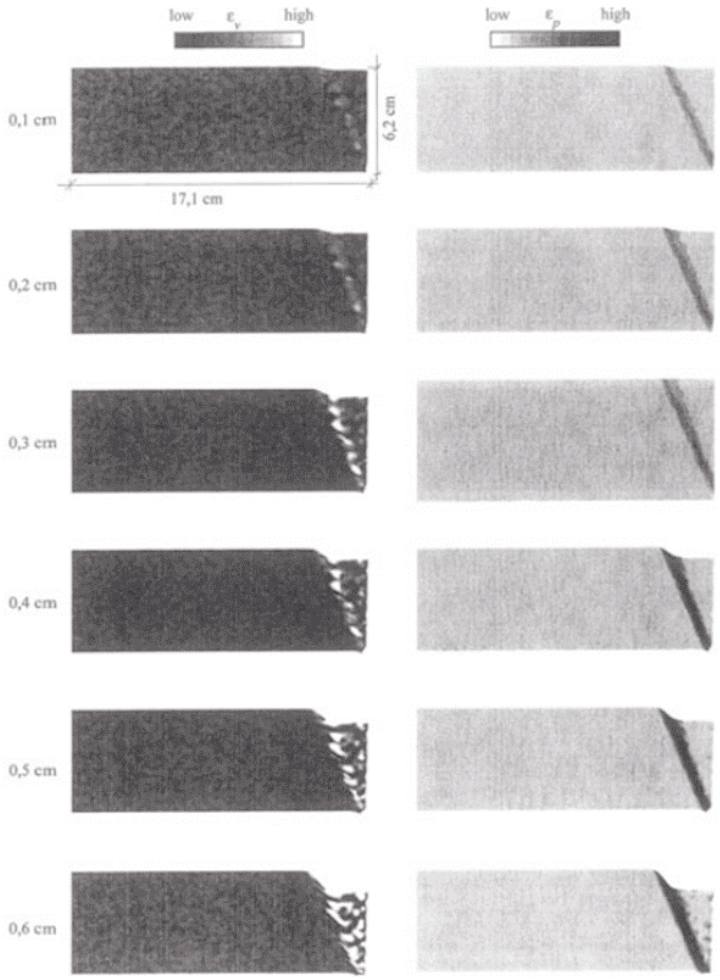


Figure 2.15. Evolution of the Localized Zone with employing PIV in the Active Case (Nübel and Weitbrecht, 2002).

Desrues and Viggiani (2004) made an experimental study with plane strain (bi-axial) apparatus, shown in Figure 2.16, to monitor strain localization in sand by means of stereophotogrammetry method. They performed 80 tests on loose and dense Hostun sand, a fine-grained, angular siliceous sand coming from the Hostun quarry (Drome, France). The mean particle diameter of Hostun sand (D_{50}) is 0.35 mm. They concluded that the thickness and orientation of shear bands, as well as the strain level at which a

shear band first forms, depend on a number of factors including the initial state of the material (mean effective stress and void ratio), its grading (grain size, uniformity, etc.), and the size and slenderness of the specimen. Desrues and Viggiani (2004) also indicated in their conclusion that with the development of new visualization techniques; such as particle image velocimetry (PIV) and the digital images correlation (DIC), the process of strain localization will be observed more realistically.

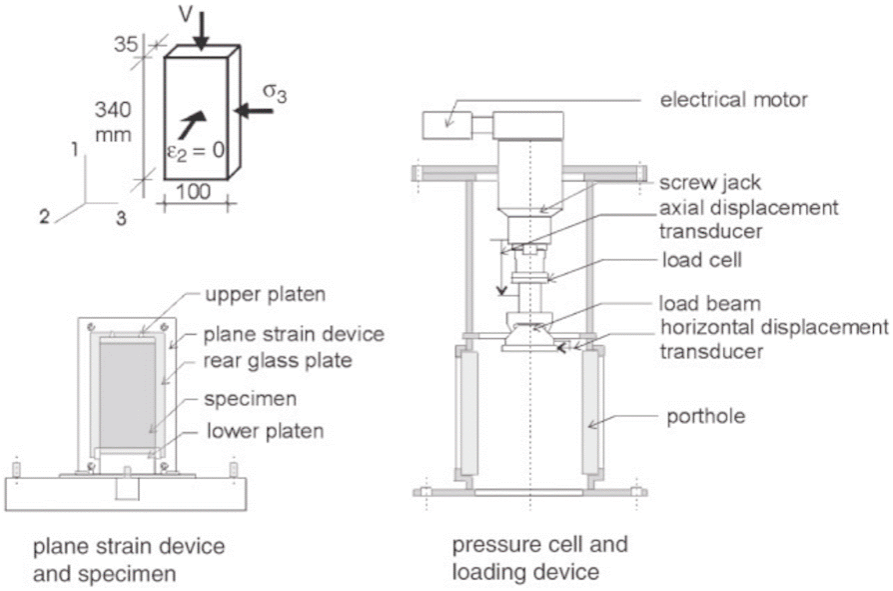


Figure 2.16. Schematic Diagram of the Plane Strain Apparatus.

Slominski *et al.*, (2006) made a study to visualize deformation in granular bodies employing particle image velocimetry technique (PIV). The aim of their investigation was showing the potential of the particle image velocimetry (PIV) technique to measure directly internal displacements in plane strain specimens of cohesionless sand during the pull-out test of a wall and confined granular flow in a model silo. They conducted the tests with Karlsruhe sand (mean grain diameter D_{50}=0.5 mm, uniformity coefficient C_u=2). Slominski *et al.*, (2006) instrumented the glass container having the length 0.5 m, width 0.25 m and height 0.2 m to conduct the experiments, as illustrated in Figure 2.17. By changing the surface roughness of the metal wall, they tried to observe the effect of roughness on the strain localization. Based on the results, they concluded that particle image velocimetry (PIV) method can be used as a useful visualization technique to detect deformations in granular media without any physical contact, so it is a highly

accurate technique. They detected the strain accumulation in silos during the sand pouring. Additionally, based on the pull-out tests, they observed that dilatant region varies with relative density and for the dense sand behind the wall, dilatant region inclined under the angle of 65^o-70^o with respect to the bottom in the case of a very rough and rough wall and 45^o in the case of a smooth wall.

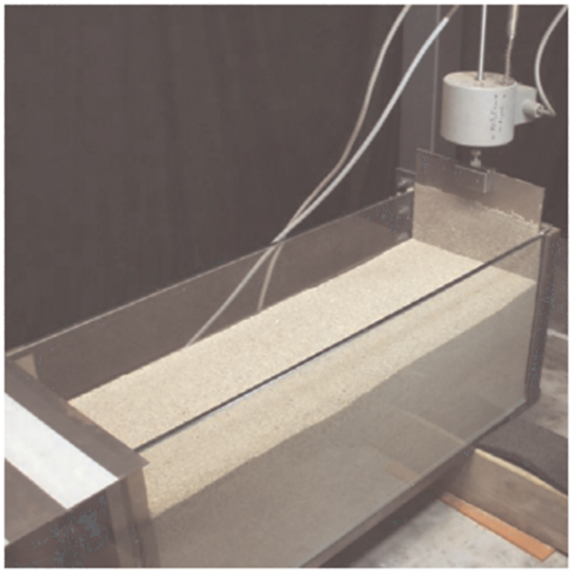


Figure 2.17. Experimental Set-Up for Pull-Out Test (Slominski *et al.*, 2005).

Rechenmacher (2006) performed a study to observe initiation of shear band by comparing the behavior conducted both plane strain and triaxial tests employing digital image correlation (DIC) method. He conducted consolidated-drained plane strain compression tests and also drained triaxial compression tests by preparing the sample either by dry pluviation or vibratory compaction method. Four types of sand was used in this experiments, namely concrete (D_{50}=0.62), Delaware Beach (D_{50}=0.50), Levering (D_{50}=0.40), Mason (D_{50}=0.32). Rechenmacher (2006) completed this study with these conclusions; multiple and conjugate shear bands were seen at the initiation of shear band formation in the hardening regime, but persistent shear band was not observed clearly until softening in plane strain condition. Formation of shear band is affected by boundary conditions in triaxial test and DIC technique is a useful technique to visualize the process of shear band deformation.

Tejchman (2008) made a series of studies to investigate shear localization in granular bodies. At the end of the studies, Tejchman (2008) asserted that finite element calculations are more realistic than analytical solutions for investigation of strain localization. According to him, the underlying reasons for this suggestion are that finite element calculation can take into account advanced constitutive laws describing the granular material behavior and second, they can predict the evolution of localization of deformation. Also, the researcher illustrated that the geometry of shear zones are influenced by the direction and mode of wall movement. Additionally, Tejchman (2008) reported that the smallest active earth pressures are generated when the wall moves horizontal translation mode and the largest during the wall rotate about the top. Besides, he claimed that earth pressures significantly vary with the wall displacement. Addition to these results, Tejchman (2008) also indicated that shear zone thickness increases as increasing initial void ratio, pressure level, mean grain diameter.

Lesniewska and Wood (2011) conducted model test to compare the stress generated in a soil mass with the observed deformation fields. Glass-sided box, which has a glass thickness of 20 mm, was used in this study as shown in Figure 2.18. Photoelastic method was used to obtain stress field and particle image velocimetry (PIV) technique was employed to obtain deformation in a granular material. The glass granules were used as the granular material to visualize the stress field in the mass. Lesniewska and Wood (2011) suggested that photoelastic images contain information about the variation of stress state in individual particles through the thickness of the sample. Additionally, they stated that PIV analysis allows us to obtain continuous experimental displacement and strain fields with great accuracy. Therefore, according to experimental results, comparison of stress and strain increment fields would be possible by superimposing corresponding images obtained from photoelastic and PIV technique.

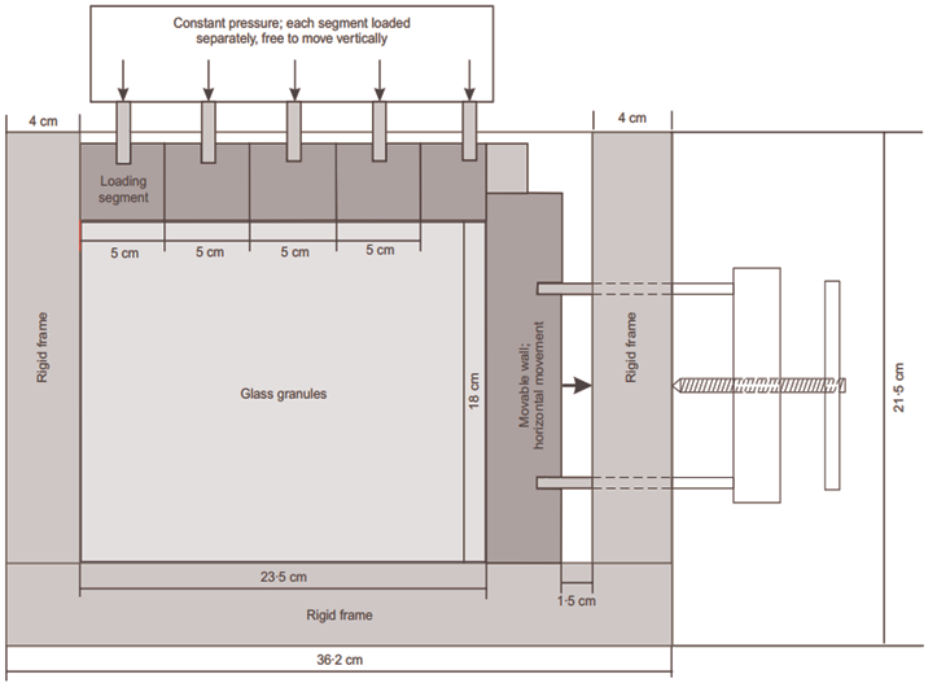


Figure 2.18. Test Box Geometry and Loading Scheme for the Active "Wall" Model (Lesniewska and Wood, 2011).

Niedostatkiewicz *et al.*, (2011) conducted a model test with instrumented psychical model (Figure 2.19) to observe characteristic features of the shear zones formation in deforming granular materials by means of particle image velocimetry (PIV) technique. In their experiments, the small scale wall translated for simulating an active failure condition. Two different granular materials were used in their experiments namely; sand grains (D_{50}=0.8) and glass granules (D_{50}=1.1). Glass granules were employed for taking photo-elastic images to obtain the information on changes in the average stress field, accompanying the specimen deformation. In their study, the main objective was to observe the influence of the initial density, grain coarseness and magnitude of wall displacement on shear localization within a strain field. Therefore, they visualized the strain accumulation in granular soil mass and also observed both volumetric and shear strain changes with wall displacement. Based on the results, they suggested that strain localization and changes in the stress field are closely correlated. Besides, Niedostatkiewicz *et al.*, (2011) concluded that PIV methods can quantify deformations with using measured displacement in granular backfill. Additionally, according

to PIV results, arrangement of shear zone changes with the type of the wall movement and shear zone occurs at both initially loose and dense backfills. Furthermore, the researchers stated that the thickness of the shear zone in granular material is smaller in initially dense backfill than loose backfill. Also, inclination of the zone is higher in initially dense backfill.

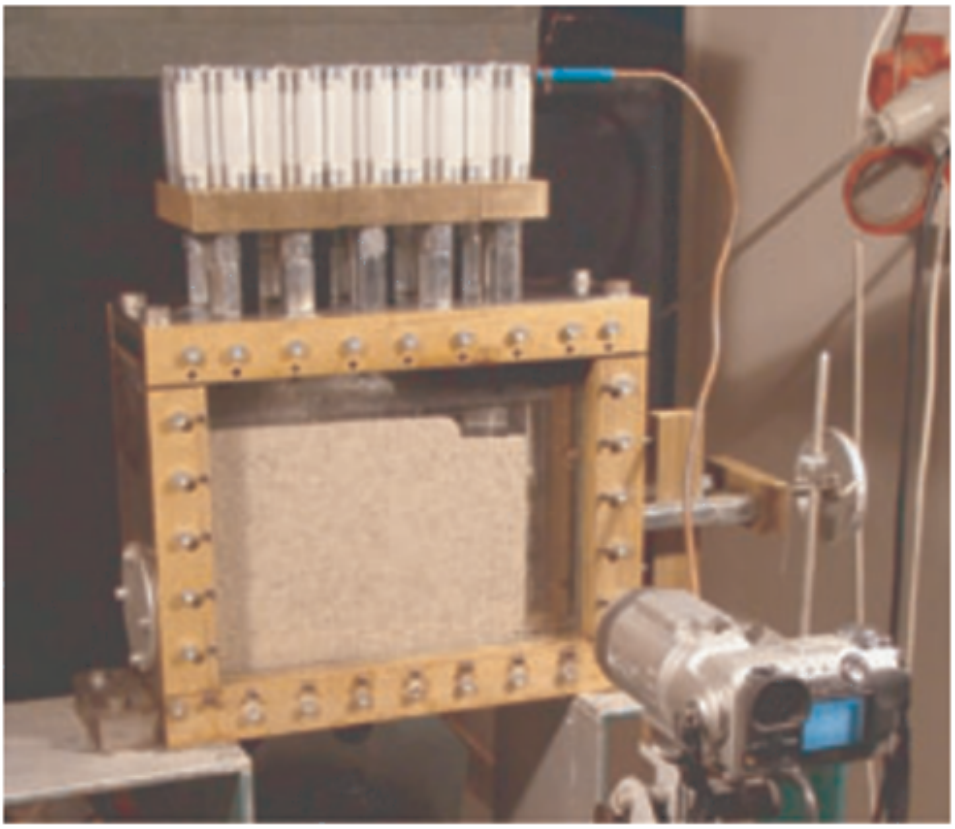


Figure 2.19. Experimental Set-up (Niedostatkiewicz *et al.*, 2011).

Rechenmacher *et al.*, (2011) performed an investigation to detect shear band deformation in granular materials with employing digital image correlation (DIC) technique. They used plane strain apparatus as shown in Figure 2.20 which is the same as Desrues and Viggiani (2004) used. Three types of material were used in their study namely; Concrete (C) sand (D_{50}=0.62 mm), Masonry-Coarse (MC) sand (D_{50}=0.84 mm) and Silica-Coarse (SC) sand (D_{50}=0.42 mm). Rechenmacher *et al.*, (2011) measured the shear band thickness with using DIC results and concluded that shear band thickness was ranged between 6 and 9.5 times D_{50}. Based on the DIC results and analysis, they indicated that grain shape, angularity, and grain size distribution may

also affect observed shear band thickness. Additionally, Rechenmacher *et al.*, (2011) concluded that DIC technique can be utilized to understand the tie between micro- and macroscopic sand response.

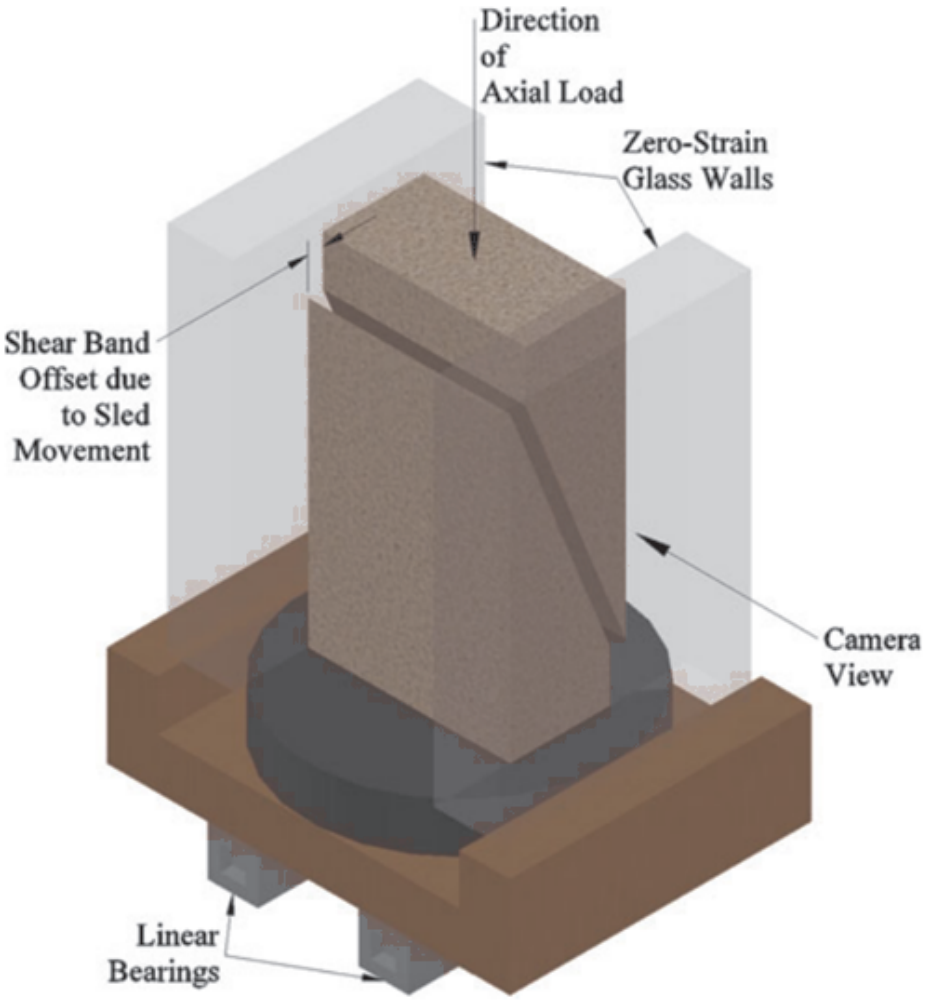


Figure 2.20. Conceptual Representation of Plane Strain Test Specimen and Surrounding Hardware (Rechenmacher *et al.*, 2011).

Borja *et al.*, (2012) carried out an investigation to show the influence of spatial heterogeneity in density on the shear band. For this purpose, they combined experiment results obtained by using plane strain compression test with finite element modeling on symmetrically loaded sand specimens. X-ray computed tomography (CT), digital image correlation (DIC) imaging technique and finite element (FE) method was used in their analysis. According to results, the reseachers concluded that dilatancy have

an important effect on a shear band.

Pietrzak and Lesniewska (2012) performed model tests with dense specimen to evaluate and observed active failure within granular material using particle image velocimetry (PIV) method. They instrumented a small scale model as shown in Figure 2.18 and Figure 2.19 as Lesniewska and Wood (2011) and Niedostatkiewicz *et al.*, (2011) were used, and used Starlitbeads1000 spherical glass granules (D_{50}= 1.1 mm) as a backfill material. Based on the PIV results, they observed that curvilinear failure wedge generates behind the wall and dilation prevails within the shear band. Compression is also observed inside the failure wedge. Furthermore, Pietrzak and Lesniewska (2012) observed some cyclic changes within the granular sample behind retaining wall; however they could not explain the reason of these cycles.

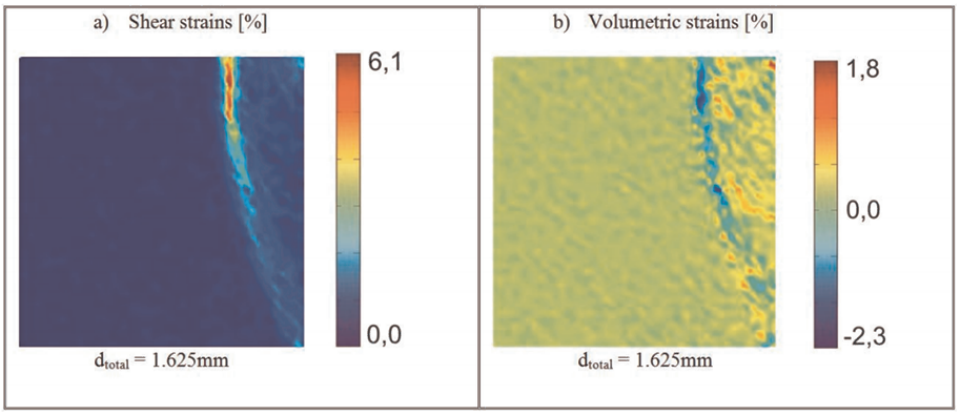


Figure 2.21. Evolution of Strains During Test (Pietrzak and Lesniewska, 2012).

Rechenmacher and Finno (2014) focused their investigation on measuring the localized displacements in sands. In this study, digital image correlation (DIC) technique was employed to detect and quantify localized displacements in a granular material. Two type of sands namely was used in their study; masonry sand (D_{50}=0.32 mm), which is a uniform, fine, subangular to subrounded quartz sand, and concrete sand (D_{50}=0.62 mm), which is slightly more well-graded with a larger median grain size. They tracked the volumetric evolutions to critical state within the shear bands in dense sample and measured the shear band thickness. Rechenmacher and Finno (2014) reported that when the peak stress occurred, shear band generated abruptly. Also, concluded that a

larger mean grain size leading to a thicker shear band in granular material.

Tehrani *et al.*, (2014) performed a study to monitor active failure behind flexible walls under pure rotation with using digital image correlation (DIC) method. The researchers aimed to observe the effect of the initial sand density on the distribution of volumetric and maximum shear strains as a function of wall displacement undergoing rotation around its base with. The experiments was carried out with using a small-scale test box (Figure 2.22 and Figure 2.23) having flexible wall in plan strain condition. Silica sand was used in this experiments (D_{50}=0.78 mm) and it was placed with using air pluviation method with different relative densities (D_r=15% and 77%). The digital image correlation (DIC) technique was employed to monitor shear band evolution with progressive outward movement of the wall. At the end of the experimental study, Tehrani *et al.*, (2014) stated that the sliding wedge remains constant with increasing wall outward movement. Also, sliding plane inclination with the horizontal for the loose backfill is slightly less than the dense backfill. Addition to these, based on their results, they asserted that the angle of the sliding plane with the horizontal was in good agreement with Rankine's theory using the critical-state friction angle of the soil for both loose and dense backfill. However, to obtain best prediction of wedge base inclination, dilatancy angle also needs to be considered.

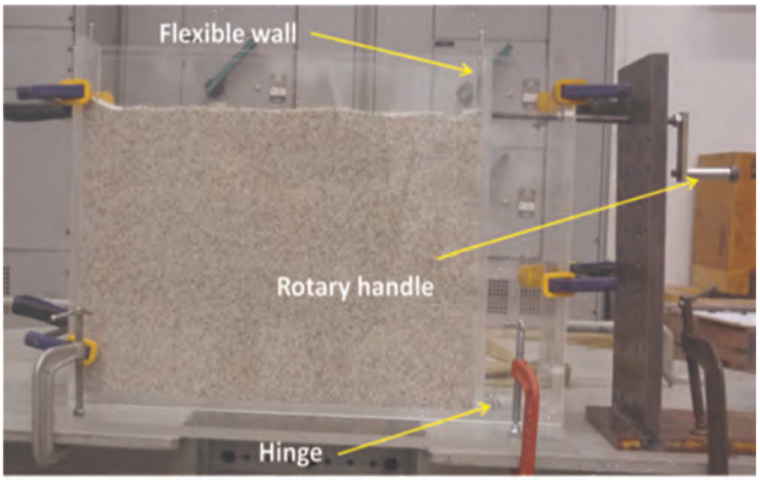


Figure 2.22. Test Box (Tehrani *et al.*, 2014).



Figure 2.23. Test and Camera Setup (Tehrani *et al.*, 2014).

2.4. Dilatancy

Dilatancy is defined simply in soil mechanics as a volume change during shearing. As the imposed stresses increase in granular material during shearing, volume expansion takes place. So, when granular particles do not have any freedom to move horizontally or vertically, they start to slide over each other.

It is well known that dilatancy is a distinguishing property of granular materials. Many researchers have conducted investigations to identify the dilatancy phenomenon (Reynolds 1885, Terzaghi 1920, Taylor 1948, Rowe 1969, Bishop 1972, Vaid and Sasitharan 1992, Schanz and Vermeer 1996, Lade 2002, Chakraborty and Salgado 2010), but unfortunately there is no detailed investigation to observe the influence of dilative behavior on generated slip surface geometry in cohesionless soil behind the retaining wall. However, dilatancy is an important phenomenon of shear localization, and so geometry of slip plane, since it relates a softening response particularly in geomaterials (Tejchman and Wu, 2010).

Reynolds (1885) was shown as the first scientist who made a study to observe the expansion of dense sand during shearing. Reynolds (1885) claimed that particle movements during deformation and failure are not necessarily in the direction of the

applied shear stresses. He called this mechanism “dilatancy”.

Later, Terzaghi (1920) indicated the influence of dilatant behavior on the generation of lateral earth pressures and referred to any earth pressure theory that ignores the granular nature of soils as old earth pressure theories.

Then, Taylor (1948) made an investigation to separate the dilatant component of strength from the frictional component. Taylor (1948) proposed a theory based on the dissipation of work in a frictional soil.

Rowe (1969) proposed a stress-dilatancy theory for granular assemblies according to the minimum energy ratio principle.

Bolton (1986) carried out experiments in plain strain condition to understand the effect of state of compaction and the confining pressure on peak angles of shearing resistance (ϕ'_p) and dilation (ψ_p). Bolton (1986) collected the available data from 17 different sands from the literature and suggested an empirical equation which uses the mean effective stress at peak shear strength (p'_p) as the quantity expressing confining pressure. This preference of using the stresses at failure obviously reduces the practicality of Bolton (1986) equation (Equation 2.10).

$$\tan(\psi_p) = 0.3\left[I_D\left(Q - \ln p'_f\right) - R\right] \tag{2.10}$$

Here I_D is the relative density (I_D=D_R/100), ranging from 0 to 1; Q and R are line-fitting parameters that depend on the inherent soil characteristics and the unit chosen for p'_f. To define the relationship between ϕ'_p and ψ_p, Bolton (1986) simplified Rowe’s stress-dilatancy relationship for plane-strain shearing through line-fitting (Equation 2.11).

$$\phi'_p = \phi'_c + r\psi_p \tag{2.11}$$

Here r is a line-fitting parameter and ϕ'_c is the critical state friction angle. A similar relationship has also been proposed by Bishop (1972). Bolton (1986) suggested 0.8 for the value of r.

Vaid and Sasitharan (1992) performed a series of triaxial tests on Erksak sand to investigate the influences of stress path and loading direction on the strength and dilatancy of sands. Based on the results, the researchers concluded that the peak friction angle is uniquely related to ψ_p, regardless of relative density, confining pressure, stress path, and mode of loading.

Schanz and Vermeer (1996) conducted an experimental study to investigate the differences between dilatancy angle obtained using plain strain test and triaxial test. According to results, Schanz and Vermeer (1996) reported that ψ_p is almost same in plane strain and axis metric conditions, whereas ϕ'_p differs considerably.

Lade (2002) made an experimental study to investigate shear bands and failure in granular materials. For this purpose, triaxial compression tests were carried out. In the light of the experimental investigation, Lade (2002) indicated that the reduced rate of dilation seems to be related with the appearance of the shear band and the achievement of critical state conditions within the shear plane in the compression test. Also, he stated that shear planes can be observed in granular materials that dilate and they generate after peak failure in triaxial compression.

Chakraborty and Salgado (2010) investigated the correlation between ϕ'_p, ϕ'_c, and ψ_p for low confining pressures by conducting plain strain compression and triaxial compression test on Toyoura sand. At the end of the studies, Chakraborty and Salgado (2010) defined the variation of the line-fitting parameter Q with pre-shear consolidation pressure for Bolton's equation (Equation 2.10).

3. SMALL SCALE RETAINING WALL MODEL

3.1. Physical Model

In the present study, in order to investigate the dependency of slip plane geometry on dilatant properties of granular assemblies and to observe the failure mechanism within the granular soil mass, 1 g small scale retaining wall model tests were conducted. The backfill soils in these tests were prepared with different relative densities (I_D) to achieve different dilatancy angles (ψ_p). Physical model set-up used for this purpose consists of a testing box, a model retaining wall that is capable of translating laterally, a sand pluviation system, a storage tank, a crane, and a data acquisition system (Figure 3.1a). The testing box is 140 cm in length, 60 cm in depth, and 50 cm in width (Figure 3.1b) and simulates plane strain condition. Based on the literature survey, it was decided that plane-strain state is an appropriate simplification of reality for understanding the behavior of backfill soils of retaining walls. Plane strain condition corresponds to the state of deformation during which the material is free to deform in two-dimensions while its deformation is fixed in the third dimension. Sides of the testing box are made of 50 mm thick Plexiglass, which are loaded by lateral pressures, allowing the observation and monitoring of the soil deformations. As a result, photographic images of the backfill at different stages of wall deformation can be captured for using in later analysis. Captured images are analyzed using particle image velocity (PIV) method for identifying the geometry of failure surfaces. The model retaining wall is an aluminum plate which is rectangular in cross-section. The height and width of the model wall are 35 cm and 50 cm, respectively (Figure 3.2a). In order to minimize the adverse effects of the rigid boundary at the bottom, the moving plate that simulates the vertical retaining wall is located 15 cm above the bottom of the test box. The model wall is capable of translating laterally either towards or away from the retained backfill. These tests correspond to passive and active failure conditions at the ultimate states, respectively. Five highly sensitive miniature pressure transducers were mounted along the vertical axis of the retaining wall model (Figure 3.2 and Figure 3.3) for monitoring the variations of lateral earth pressures along the face of the wall

throughout the tests. Furthermore, two pressure transducers were buried in the backfill during model preparation to measure vertical effective stress at different depths. The miniature pressure transducers used in the present study have 200 kPa capacity and the properties are shown in Table 3.1. The pressure transducers used in the model have high sensitivity, high stiffness and are insensitive to temperature variations. The top view and dimensions of transducers are shown in Figure 3.2b and Figure 3.2c, respectively. All transducers were calibrated prior to experiments in accordance with the manufacturer's guidelines. The crane used in this study is mobile and independent of the testing system which provides it with flexibility so that it can be used for other purposes within the laboratory shown in Figure 3.4. The load cell is connected to the back face of the wall as illustrated in Figure 3.5 in order to measure the horizontal thrust when it required. The type of the load cell is tension-compression cell that is stainless steel and its capacity is 5 kN.

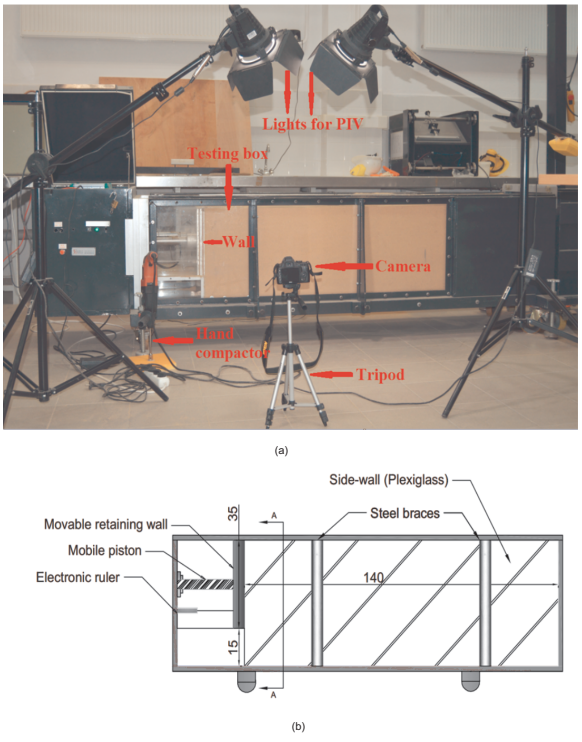


Figure 3.1. Retaining Wall Model Set-Up (a) Photograph c) (b) Horizontal Cross-Section.

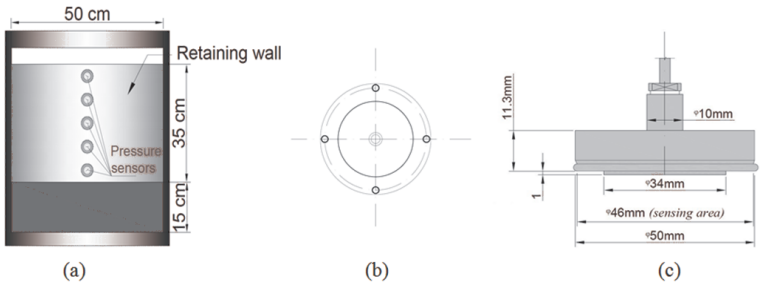


Figure 3.2. (a) Positions of the Pressure Transducers Along the vertical Axis of The Retaining Wall Model, (b) Face View of a Pressure Transducer, (c) Side View of a Pressure Transducer.

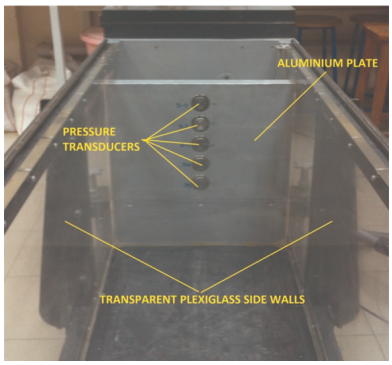


Figure 3.3. Location of Pressure Transducers and Transparent Side Walls.



Figure 3.4. Movable Part of Model System.

Table 3.1. Properties of Pressure Transducers.

Type	KDE-200 KPA KDF-200 KPA
Capacity	200 kPa
Rated output Approx.	0.3mV/V (600 x 10 - 6 strain)
Non-linearity	2%RO
Temperature range	-20∼+600C
Input/output resistance	350Ω
Recommended exciting voltage	Less than 3V
Allowable exciting voltage	10V
Cable drawing direction	KDE-PA : from side of body/KDF-PA : from back of body
Weight	160g

The horizontal translation of the wall was provided by an electrical motor-actuator system. The displacements of the model wall were measured by an electronic ruler as can be seen in Figure 3.5. Motor displacement steps also provide the means for validating electronic ruler measurements. Data were collected via a multi-channel data logger system which is capable of handling an aggregate data collection rate of 400 kHz, with a maximum per channel sample rate of up to 500 Hz (Figure 3.6). To obtain the images with high resolution, lighting system (LED169A) were used which illuminates the environment uniformly as illustrated in Figure 3.1.

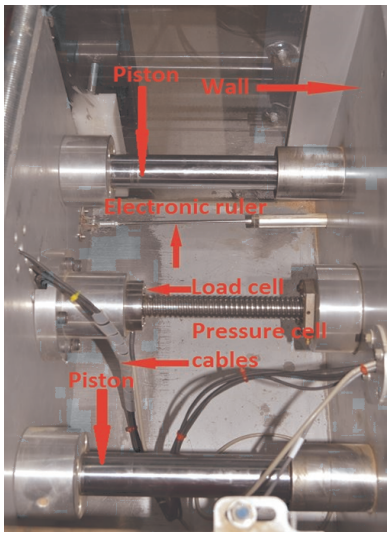


Figure 3.5. Back Face of the Wall.



Figure 3.6. Data Logger with 16 Channels.

3.2. Equipments Used in PIV Analysis

3.2.1. Digital Camera

To detect the deformation pattern behind the wall, PIV method needs consecutive images captured during the experiments. These required images were captured by a digital camera (Figure 3.7) when the model wall translated horizontally in both an active mode and a passive mode (away from the backfill and towards to the backfill respectively). The digital camera has an image resolution of 6000 x 4000 pixels (model reference: Nikon D3200). All images were recorded in .jpeg format for the PIV analysis. Shooting time between two frames effects the results of the analysis and the recording speed should be fast enough to capture more images which are needed to monitor the deformation within granular mass. The camera used in this study is able to shoot 4 frames/sec on continuous shooting mode and it is sufficient for the analysis. The properties of the camera are shown in Table 3.2.



Figure 3.7. Digital Camera and Remote Controller used in the Experiments.

Table 3.2. Properties of the Digital Camera.

Feature	D3200
Sensor	24.2 Megapixel CMOS
LCD size/resolution	3.0” / 921k pixel
Viewfinder magnification	0.78X
Continuous shooting (full res)	4 frames/sec
Movie max resolution	1920 x 1080 (30 fps)
Manual controls for videos	Yes
Dedicated movie rec. button	Yes
Remote controls	Wired, wireless
Stereo mic input	Yes
Wi-Fi support	Optional
Battery used	EN-EL14
Battery life (CIPA standard)	540 shots
Dimensions (W x H x D)	5.0 x 3.8 x 3.1 in.
Weight	455 g
Available colors	Black, red

3.2.2. Remote Controller

After conducted several experiments, it was observed that small vibrations of the camera lead to produce inaccurate results in the analysis. To put it in other words, wild vectors or wild displacements occur due to very small vibrations in the camera. That’s why; the results of the analysis of these images were insufficient to visualize the deformation pattern so the slip surfaces behind the wall. Therefore, to prevent vibration of the camera during the shooting, it was decided to use a remote controller, shown in Figure 3.2, thought the experiments.

3.2.3. Tripod

The camera was attached on a tripod during the testing to gain the undisturbed image. The camera was oriented perpendicularly to the plane of deformation by means of the tripod during the experiments. The tripod used in the experiments can be adjusted to the recording heights.

3.2.4. Lights

Two LED169A lights were used during the experiments to illuminate physical model set-up homogeneously. At the beginning of the experiments, some of the tests were performed without using LED lights. The images obtained without using these lights were not sufficient to use in PIV analysis to detect the deformation due to appearing of shadows on the invested area. Therefore, during the tests, two lights were located at each side of the camera to enlighten the plane surface of the testing tank homogenously. Moreover, light's brightness is dimming from 10%-100% and adjusted to obtain more clear texture of the sand particles. Properties of the lights are shown in Table 3.3.

Table 3.3. Properties of the Light.

Model	GL-LED169A
Light size	16 x 16 x 20 cm (6.3"W x 6.3"H x 7.87"D)
Weight	0.73kgs(1.61lbs)
Power	10W
Voltage	DC12V(AC adapter 110V-240V)
Color temperature	5600K or 3200K
Illuminance	1360Lux/61 cm

4. BACKFILL PROPERTIES AND SAMPLE PREPARATION

In the present investigation, the soil used as a backfill material is so-called Akpınar sand, which has a sufficient texture for application of the PIV technique. The properties of Akpınar sand is obtained by conducting laboratory tests, such as sieve analysis, specific gravity, minimum maximum index densities, direct shear tests and triaxial tests.

4.1. Backfill Properties of Akpınar Sand

4.1.1. Sieve Analysis

Sieving analysis tests can be performed in either wet or dry conditions. Dry sieving is used only for soils with a negligible amount of plastic fines, such as gravels and clean sand; whereas wet sieving is applied to soils with plastic fines namely clays and silts. In this study, dry sieving test was conducted to obtain the grading of backfill material. The sieving analysis test was conducted according to (ASTM D422-63, 2007) Standard Test Method for Particle-Size Analysis of Soils.

4.1.1.1. The Result of Sieve Analysis. The sieving analysis test was performed with using different mesh size to obtain the gradation of backfill material according to Standard Test Method for Particle-Size Analysis of Soils (ASTM D422-63, 2007). Based on the results, Akpınar sand gradation curve was obtained as shown in Figure 4.1.

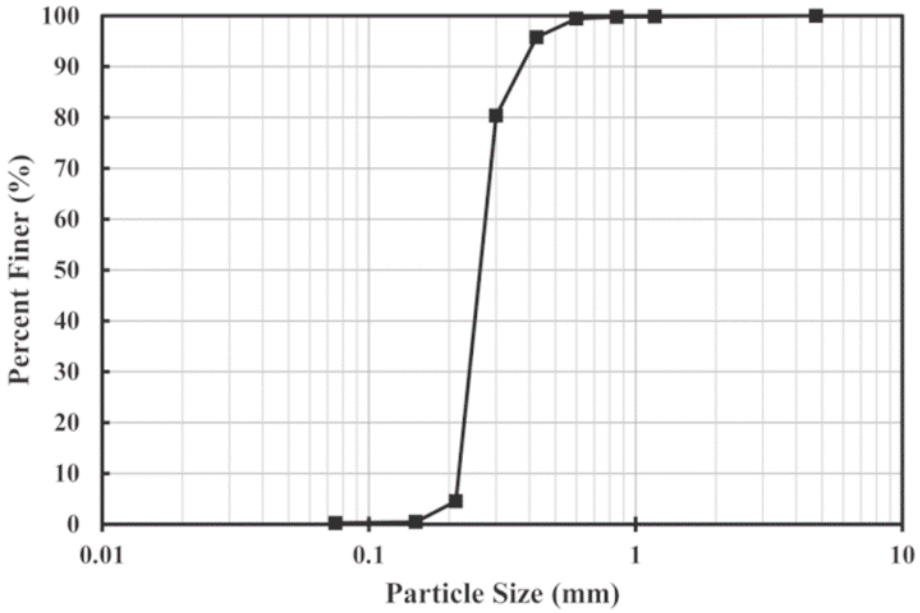


Figure 4.1. Particle Grading Curves for Akpınar Sand.

4.2. Particle Shape of Akpınar Sand

Shape properties of tested sand particles were investigated according to two important scales, which are used in the literature, namely sphericity (S), roundness or angularity (R). These properties of tested sand were determined based on the grain shape charts (Figure 4.2) proposed by Cho *et al.*, (2006) modified from Krumbein and Sloss (1963). For this purpose, sand particles were visualized by means of stereomicroscope. Randomly chosen particles were photographed for the determination of shape characteristics as shown in Figure 4.3. Following that, sphericity and roundness values of 100 selected particles were determined according to the shape determination chart (Figure 4.4). Later, average values of shape properties (S_{ave} and R_{ave}), as shown in Table 4.2, were used to characterize particle shapes of Akpınar sand.

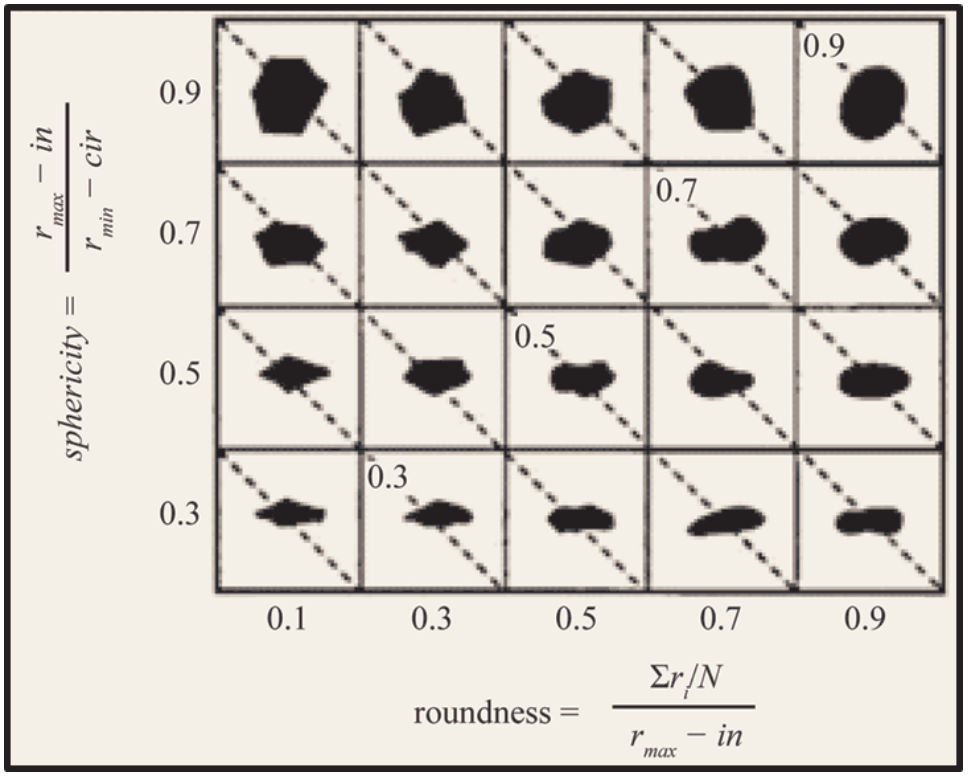


Figure 4.2. Particle Shape Determination-Sphericity (S) and Roundness (R) (Cho *et al.*, 2006).

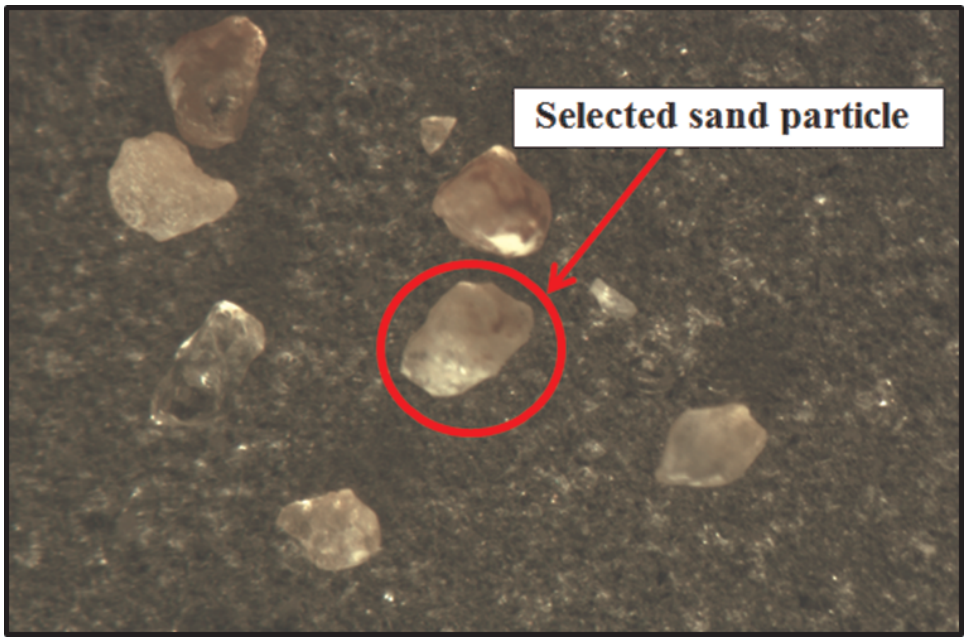


Figure 4.3. Particle Shape Determination-Sphericity (S) and Roundness (R) (Cho *et al.*, 2006).

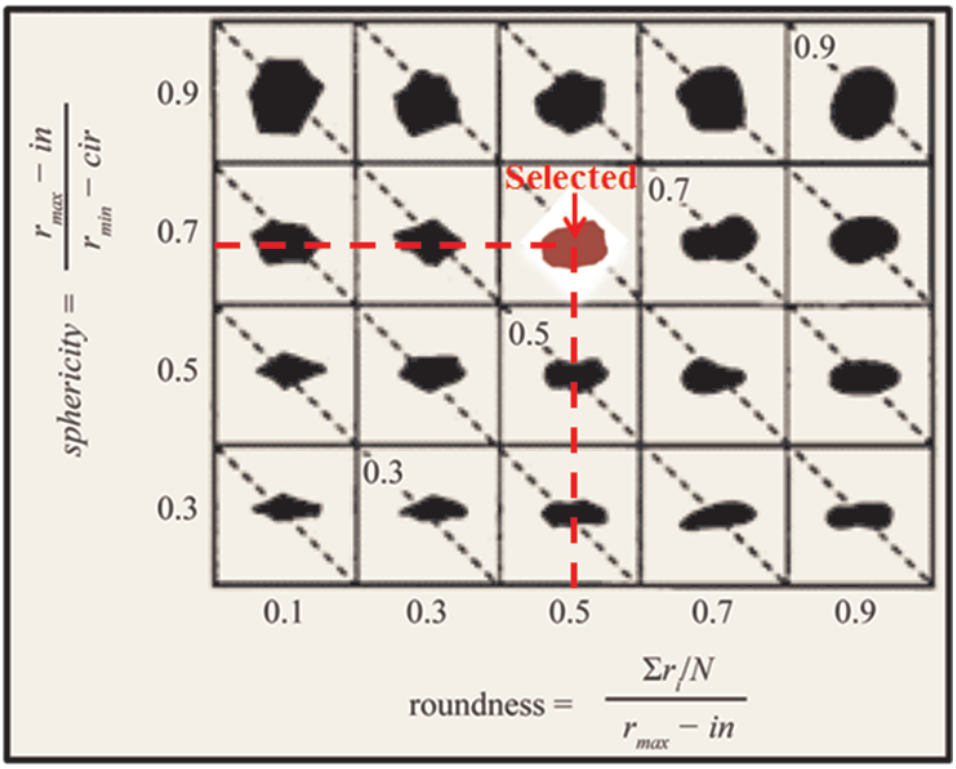


Figure 4.4. Particle Shape Determination on Shape Chart.

4.2.1. Determination of Specific Gravity

The specific gravity of soil solids is determined according to the ASTM standard D 854, Standard Test Methods for Specific Gravity of Soil Solids by Water Pycnometers. The test method includes the determination of the specific gravity of soil solids that pass the 4.75 mm (No. 4) sieve. Method *B* procedure from ASTM D 854 is suitable for oven dried specimens; therefore, this procedure is used for determining the specific gravity of the backfill material.

Three tests were carried out to determine the specific gravity and the average value of 2.63 was used for the calculations. The specific gravity analysis results are indicated in Table 4.1.

Table 4.1. Specific Gravity Results.

Soil	Specific Gravity
Sample 1	2.61
Sample 2	2.62
Sample 3	2.65
Average	2.63

4.2.2. Determination of Minimum and Maximum Relative Densities

The relative density of the tested material was identified according to the ASTM standard, ASTM D 4254- Standard Test Methods for Minimum Index Density and Unit Weight of Soils and Calculation of Relative Density and ASTM D 4253 - Standard Test Methods for Maximum Index Density and Unit Weight of Soils Using a Vibratory Table.

According to results, minimum (e_{min}) and maximum index (e_{max}) densities were measured as 0.58 and 0.87 respectively.

4.2.3. Direct Shear Test for the Determination of Interface Friction Angles

Direct shear type interface tests were conducted to measure the angles of shearing resistance between the retaining wall and backfill and also between backfill and plexiglass interfaces. The shearing resistance was determined by following the ASTM standard, D3080 - 04 Standard Test Method for Direct Shear Test of Soils under Consolidated Drained Conditions.

The procedures and test equipment are the same with the direct shear test which is conducted to determine internal friction angle of backfill sand except lower part of the direct shear box filled with the aluminum plate and the plaxiglass. In order words, upper part and lower part of the direct shear box are filled with the backfill sand and the aluminum plate or the plexiglass respectively. Therefore, interface friction angles,

namely the sand-moving aluminum plate and the sand-the plexiglass, are easily determined using the direct shear experiment with slight alteration in sample preparation part of the procedure. The results of the tests for loose backfill are shown in Figure 4.5 and Figure 4.6. Measured values of the friction angle for the interface between the sand and the aluminum plate and also for the interface between the plexiglass and the sand are shown in Table 4.2.

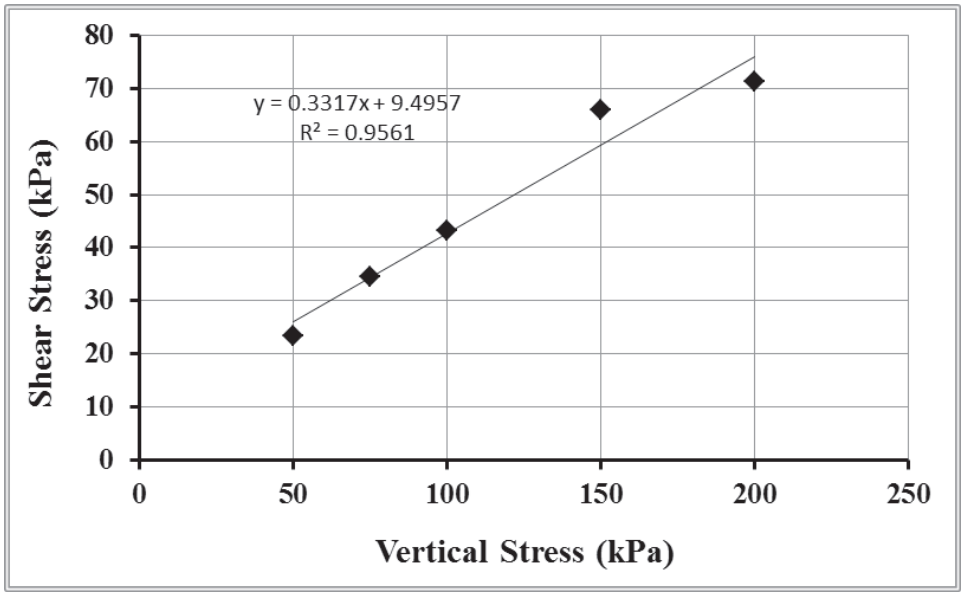


Figure 4.5. Wall-Backfill Interface Friction (δ_{wb}) Obtained by Conducting Direct Shear Test.

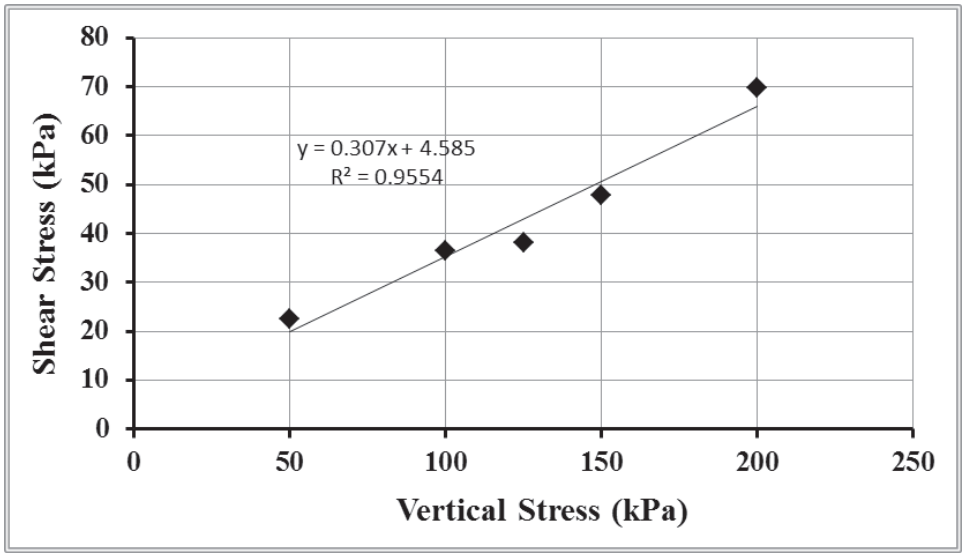


Figure 4.6. Plexiglass-backfill Interface Friction (δ_{pb}) Obtained by Conducting Direct Shear Test.

A summary of the physical characteristics of the tested sand is given in Table 4.2.

Table 4.2. Basic Properties of Akpınar Sand.

Property	*Value*
Classification	Poorly Graded (SP)
Max. void ratio (e_{max})	0.87 (ASTM)
Min. void ratio (e_{min})	0.58 (ASTM)
D_{10}	0.22
D_{30}	0.24
D_{50}	0.27
D_{60}	0.28
Uniformity coefficient (C_u)	1.23
Coefficient of gradation (C_c)	0.97
Specific gravitiy (G_s)	2.63
Average sphericity, S_{ave}	0.7
Average roundness, R_{ave}	0.5
Wall-backfill interface friction $\delta_{(loose)wb}(^\circ)$	19
Wall-backfill interface friction $\delta_{(mediumdense)wb}(^\circ)$	21
Wall-backfill interface friction $\delta_{(dense)wb}(^\circ)$	23
Plexiglass-backfill interface friction $\delta_{(loose)pb}(^\circ)$	17
Plexiglass-backfill interface friction $\delta_{(mediumdense)pb}(^\circ)$	18
Plexiglass-backfill interface friction $\delta_{(dense)pb}(^\circ)$	21
Critical state friction angle $\phi'_c(^\circ)$	33

4.2.4. Triaxial Test

Triaxial tests were conducted to obtain α_ψ and m_ψ constants, which are needed for calculating the dilation angle (ψ_p) of the backfill soil. The procedure for the determination of α_ψ and m_ψ constants are explained by Çinicioğlu *et al.*, (2013). All triaxial tests performed in the present study are conventional drained triaxial compression tests consolidated under K_o conditions (CK_oDC) (Figure 4.7) by means of the automatic

triaxial apparatus. Triaxial samples were consolidated underK_o conditions since model tests are also underK_o conditions. Soil sample were prepared by air-pluviation method and saturated using de-aired water. Saturation level was controlled by checking the B-parameter. K_o conditions was achieved by observing the radial strain, the absolute value of which was kept under 0.005%.CK_oDC triaxial tests were conducted and the necessary corrections were done following the guidelines of ASTM D-7181 (2011). The results of the triaxial tests are shown in Table 4.3. Detailed information about the test procedure can be found in Abadkon (2012).

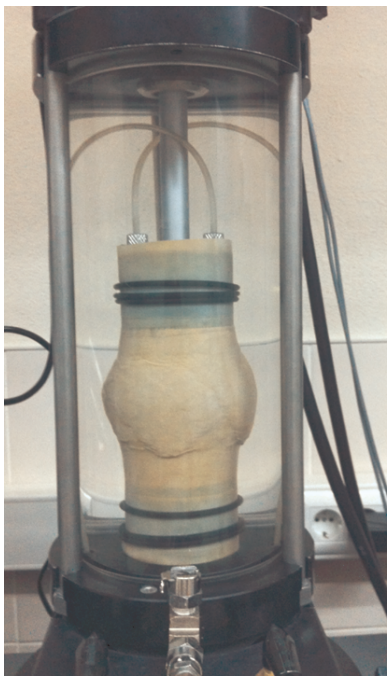


Figure 4.7. Triaxial Sample at Failure.

Table 4.3. The Parameters Required for Calculating Model-Appropriate ϕ'_p and ψ_p for Akpınar Sand.

Property	Value
Dilatancy effect on friction (r)	0.39
Stress-based dilatancy constant (α_ψ)	-0.066
Density-based dilatancy constant (m_ψ)	0.64

4.3. Sample Preparation

During model preparation, Akpınar sand was placed behind the model retaining wall by dry-pluviation through a hopper (Figure 4.8). The falling height of sand during pluviation can be adjusted to achieve the desired relative density in the backfill material. Backfill was compacted with a hand-held electrical compactor as necessary, whenever dry-pluviation was not sufficient to achieve target densities. Density cans (54 mm in diameter, 34 mm in depth) were used to measure the unit weight and to calculate relative density of the backfill during model tests. These cans were placed in a staggered scheme in the vertical direction. At the end of each experiment, density control cans were extracted carefully and weighed immediately for relative density calculations, shown in Figure 4.9. After backfill preparation, model tests were conducted by moving the model wall away from the backfill in a translational mode at a constant speed of 0.5 mm/s. Tests were continued until after active or passive failure state was reached. During the tests, images were captured through the transparent side-walls for every 0.1 mm of wall translation.



Figure 4.8. Preparation of Backfill with Dry-Pluviation Method.



Figure 4.9. Extraction of Density Can.

5. DILATANCY CALCULATION BASED ON IN-SITU PROPERTIES

This study attempts to investigate the influence of dilatancy on geometries of both active and passive slip planes and on strain localization. Theoretically, the influence of dilatant behavior on shear planes is acknowledged (Salençon 1977; Chen and Liu 1990; Atkinson 2007); however there are no experimental studies that attempt to monitor it for soil bodies except during element tests, such as plane strain and triaxial tests. The underlying reason for the absence of studies that explore the influence of dilatancy on shearing bodies of soil is the difficulty associated with the calculation of dilatancy angle from soil properties. However, in this study a recent novel equation proposed by Çinicioğlu and Abadkon (2014), which allows the computation of dilatancy angle from in-situ soil properties, is used. Çinicioğlu and Abadkon (2014) equation yields peak dilatancy angle (ψ_p) as a function of pre-shear soil properties, namely relative density (I_D) and mean effective stress (p'_i):

$$\tan(\psi_p) = \alpha_\psi \left(\frac{p'_i}{p_a}\right) + m_\psi I_D \tag{5.1}$$

Here, α_ψ and m_ψ are unit-independent empirical soil constants; andp_a is the atmospheric pressure. Relative density (I_D) varies between 0 and 1. The main advantage of this equation is that it is based on in-situ soil parameters (I_D and p'_i), and not on parameters that correspond to failure states. As a result, Equation 5.1 can be used to calculate dilatancy angle directly from the information collected during the preparation of cohesionless backfill. Additionally, the influences of p'_i and I_D on ψ_p are uncoupled (Çinicioğlu *et al.*, 2013). Thus, theoretically two strength tests at different p'_i-I_D combinations are sufficient to calculate soil-specific constants α_ψ and m_ψ. Accordingly, α_ψ and m_ψ constants for the backfill soil used in this study were obtained by conducting triaxial tests. Consequently, it became possible to calculate the variation of dilatancy angle within the model backfill, which rendered the investigation of the

influence of dilatancy angle on active failure surface geometry feasible. Equation 5.1 is given in Çinicioğlu and Abadkon (2014). The accuracy of Equation 5.1 is shown in Figure 5.1 for the different soils. Constants α_ψ and m_ψ for the soils shown in Figure 5.1 are obtained using the reported test data presented in the literature.

Additionally, as mentioned in the literature part, knowledge of ψ_p allows the computation of peak friction angle using Equation 2.11 as proposed by Bolton (1986). Therefore, in the present study, ϕ'_p is calculated also from backfill I_D and p'_p values by combining Equation 5.1 and Equation 2.11. The accuracy of the estimations of the resulting equation is shown in Figure 5.2 for different soils.

In order to compare and quantify active and passive slip surface geometries and deformations, backfill soils were prepared with different dilatant properties. This was achieved by varying the relative densities between tests, since it was not possible to significantly alter the stress states in 1g tests. Accordingly, backfill relative densities (I_D) varied within the range 0.20 to 0.90 for the present investigation. Such density variations allowed direct visualization of differences in slip planes and localized strains formed in granular backfills as functions dilatancy angles.

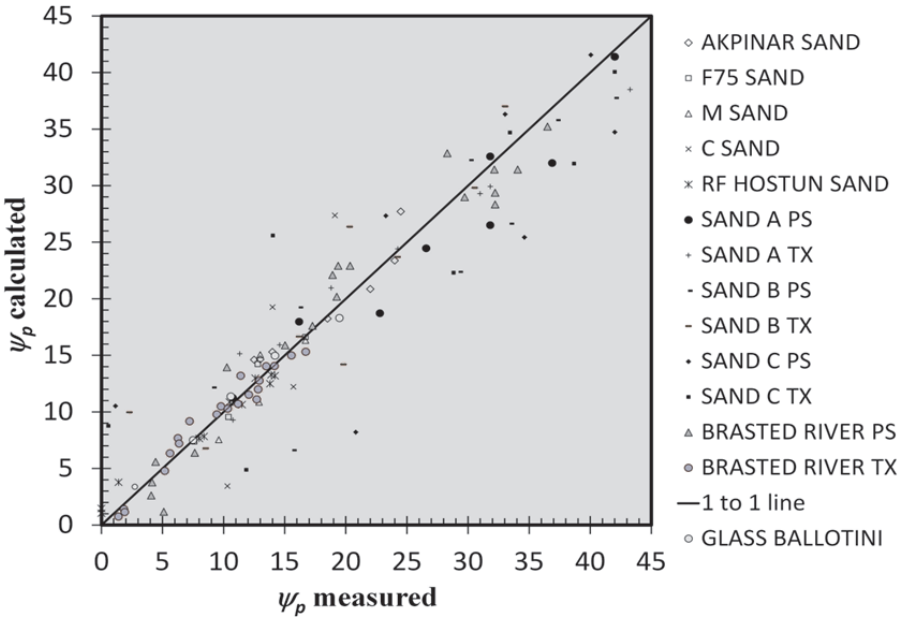


Figure 5.1. Comparison of Calculated and Measured ψ_p using Equation 5.1 (Çinicioğlu and Abadkon 2014).

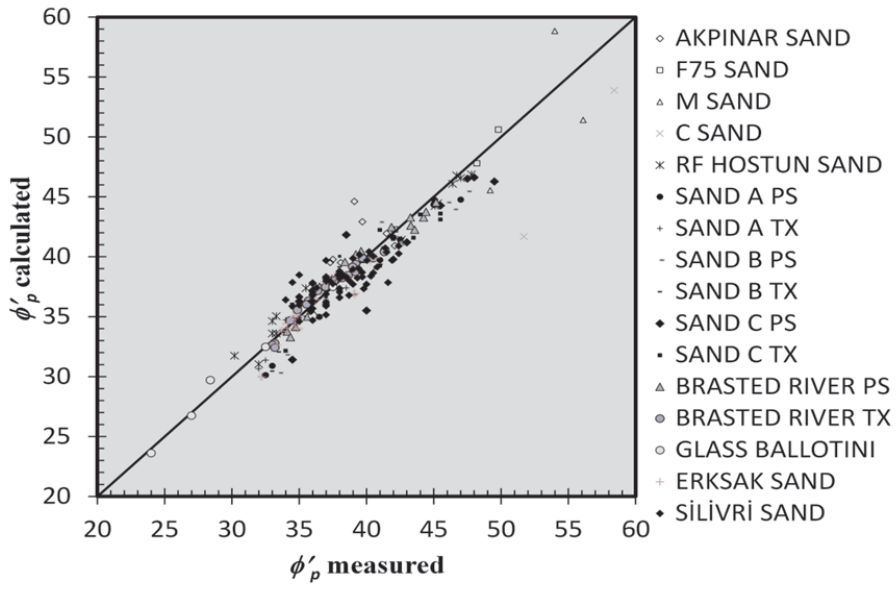


Figure 5.2. Comparison of Calculated and Measured ϕ'_p using Equation 2.11 (Çinicioğlu and Abadkon 2014).

6. VISUALIZATION OF DEFORMATION

Physical model studies require measurement of deformations and strains during testing. This is a difficult task considering the problems associated with instrumenting soil models. To overcome this difficulty, researchers developed different visualization tools that allow the deformations and strains to be computed from test records, such as false relief tereophotogrammetry (Butterfield 1970), X-rays (Roscoe 1963, Tejchman and Wu 1995), coloured layers and markers (Yoshida *et al.*, 1994), X-ray-tomography (Desrues 1996, Alshibli 2000), electrical capacitance tomography (Jaworski and Dyakowski 2001, Niedostatkiewicz *et al.*, 2008), photogrammetry and stereo-photogrammetry (Butterfield *et al.*, 1970, Desrues, J. and Viggiani, G. 2004), digital image correlation (DIC) or particle image velocimetry (PIV) (White *et al.*, 2003, Niedostatkiewicz *et al.*, 2011, Lesniewska and Wood 2011, Lesniewska *et al.*, 2012) and X-ray micro-tomography connected to DIC (Lenoir *et al.*, 2007). All these visualization techniques are usually supported by the computer loading, digital camera and also data acquisition systems. Such developments offer higher accuracy of measurements than what was obtained few years ago (Lesniewska 2000).

PIV is an example of a growing geotechnical image analysis technique which was developed for the fluid mechanics originally by Adrian (1991), and then modified it for geomechanics applications. PIV and DIC are the different names for similar concepts. Other names for similar approaches are: image cross-correlation, block or region matching method, surface displacement analysis and sub-region scanning computer vision (Viggiani *et al.*, 2012). Nowadays, particle image velocimetry (PIV), non-invasive method, has become very common into the worldwide. For the present study, particle image velocimetry (PIV) was employed for observing the deformations and detecting the slip plane geometry within the granular soil mass depending on the dilative behavior. PIV is an image processing tool that measures the displacement fields along a plane within a deforming zone of material.

PIV, a digital image-based surface displacement measurement technique, provides highly accurate measurements of the evolving deformation field. PIV tracks particle flow by examining the difference between a reference image and a sequence of deformed images. The most important advantage of using PIV in geotechnical problems is that, unlike hydraulics applications, PIV do not need extra target markers since soil grains have natural textures (White *et al.*, 2003). To put it in other words, the sand grains can serve as tracers for visualization of deformation within granular material. This is the major advantage of PIV that leads to use it in the present study.

6.1. PIV Programs used for the Applications

There are different types of programs developed for using PIV method in experimental applications and these are listed in Table 6.1. Listed programs were investigated separately and checked for usability or adoptability in the physical model test for monitoring the deformations. Unfortunately, most of the programs are originally developed for hydraulics and not appropriate to monitor the deformations within granular soil mass in the model retaining wall test due to the speed of the test and the particle density. Additionally, some of them need to lead markers to track the changes in fluids. Furthermore, volumetric and shear strain map could not be obtained easily almost from all of them except for GeoPIV. For instance, the results obtained from using PIVlab program are shown in Figure 6.1. As seen from Figure 6.1, although the displacement vector filed can be obtained using PIVlab, volumetric strain and shear strain map could not be obtained. However, GeoPIV provides both deformation maps and displacement vector fields.

Table 6.1. Programs for using in PIV Applications.

1. AnaPIV	4. JPIV	7. openPIV	10. PIV lab	13. PPIV
2.GeoPIV	5.MatPIV	8.OSIV	11.pivmat	14.pyPIV
3.GPIV	6.mpiv	9.PIV analyser	12.PivNet2	15.URAPIV

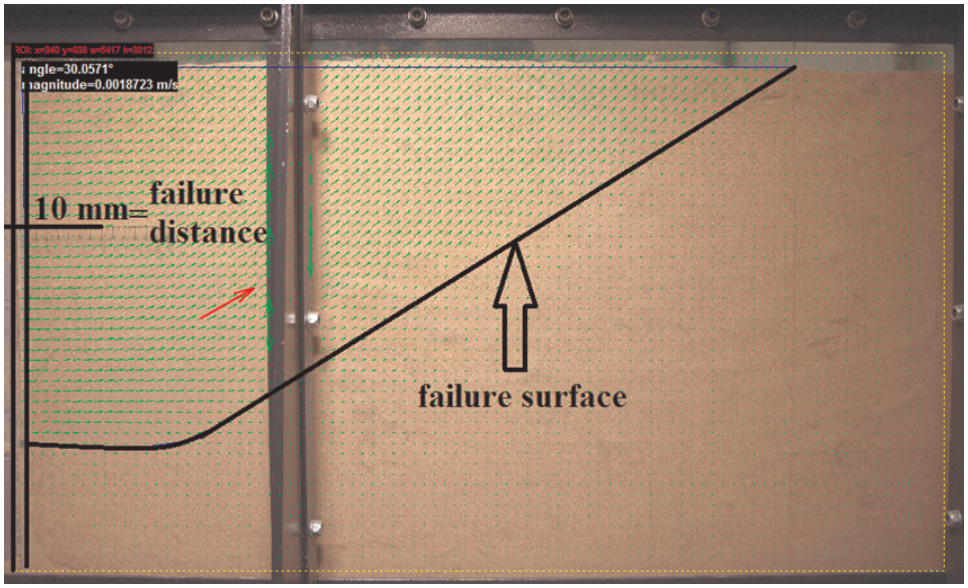


Figure 6.1. PIVlab Results for the Visialization of Deformation behind the Retaining Wall.

6.2. GeoPIV for the Slip Plane Geometry

In this study, GeoPIV was employed for measuring displacement fields so that the slip plane geometry and strain localization from successive digital images could be obtained. GeoPIV software was developed by Dave White and Andy Take during the period 1998-2004 at Cambridge University Engineering Department.

GeoPIV is a MATLAB module developed especially for the geotechnical applications (White *et al.*, 2003) and suitable for detecting deformations in granular media without any physical contact more reaslisticly (Nübel and Weitbrecht 2002, White *et al.*, 2003, 2005, Desrues and Viggiani 2004, Slominski *et al.*, 2007, Niedostatkiewicz *et al.*, 2011, Pietrzak and Lesniewska 2012). Therefore, it is becoming increasingly popular in the study of visualization of strain in granular materials.

As mentioned, GeoPIV is a MATLAB module, so the codes are required for the applications. Thanks to White and Take (developers), the required codes for the analyses were obtained from the data sheet that they have provided.

GeoPIV uses the principles of PIV to obtain displacement data from sequences of digital images captured during geotechnical testing (White and Take, 2002). The principles of PIV analysis are summarized by White and Take (2002) (Figure 6.2).

PIV operates by tracking the texture (i.e. the spatial variation of brightness) within an image of soil through a series of images. While using GeoPIV, initially the area of interest (AOI) is cut out of the digital image and divided into a grid of square patches. AOI must be covering the investigated strain field where the shear zone emerges. These patches are distinguished by their unique pixel intensity variation signatures, as shown in Figure 6.3a and Figure 6.3b. Afterwards, GeoPIV algorithm searches the specified zone within the deformed image to find a patch that has maximum similarity to the initial patch's signature. The correlation operations are most successfully performed in the frequency domain by taking the Fast Fourier Transform (FFT) of each patch (Niedostatkiewicz 2011). The difference between the target patch, measured in pixels, and the reference patch is visualized by the displacement vector as shown in Figure 6.3c. In order to obtain a precise displacement measurement, the patch texture should be as distinctive from the adjacent search zone. To put it in other words, consider one of these test patches, located at coordinates (u_1,v_1) in image 1 (Figure 6.2). In order to find the displacement location of this patch in the subsequent second image, the correlation between the patch chosen from image 1 (time=t_1) and a larger patch from the same part of image 2 (time = t_2) is evaluated. The location at which the highest correlation is detected shows the displaced position of the patch (u_2,v_2) (Figure 6.4).

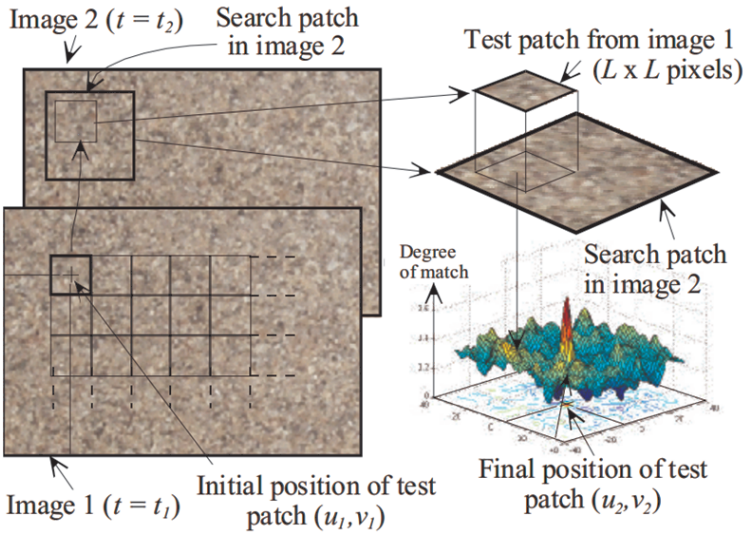


Figure 6.2. Principles of PIV Analysis (White and Take, 2002).

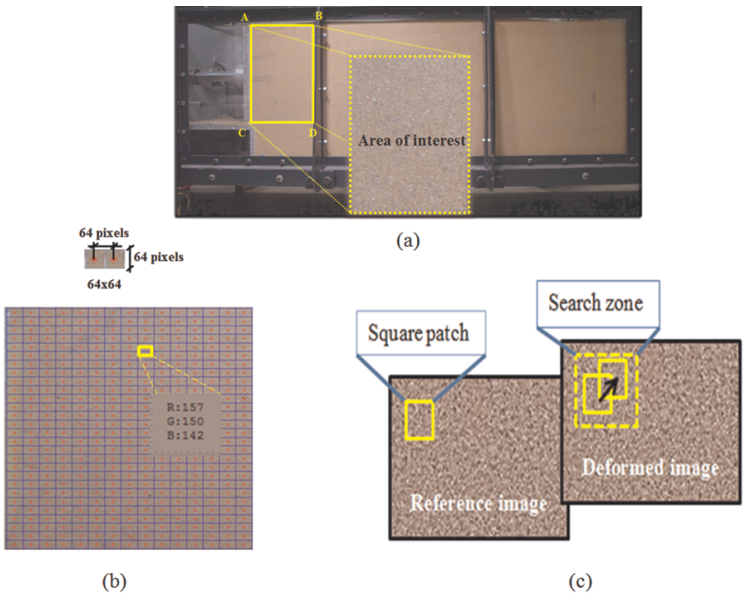


Figure 6.3. Determination of Displacement Vector Field a) Determination of Area of Interest b) Pixel Intensity Variation Signature c) Displacement Vector.

The analysis process used in GeoPIV is illustrated by the flowchart demonstrated in Figure 6.5.

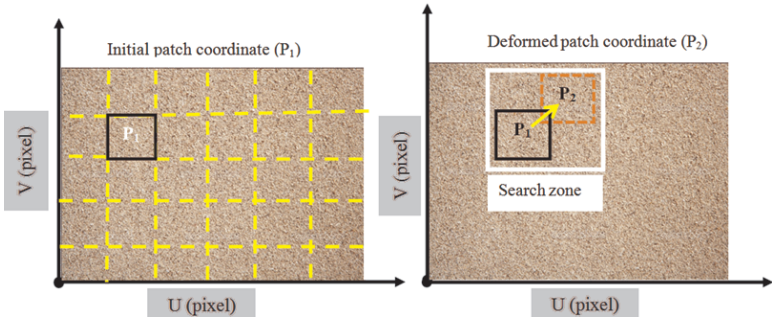


Figure 6.4. Deformation Determination in PIV a) Initial Image Divided to Square Patches b) Displacement Vector.

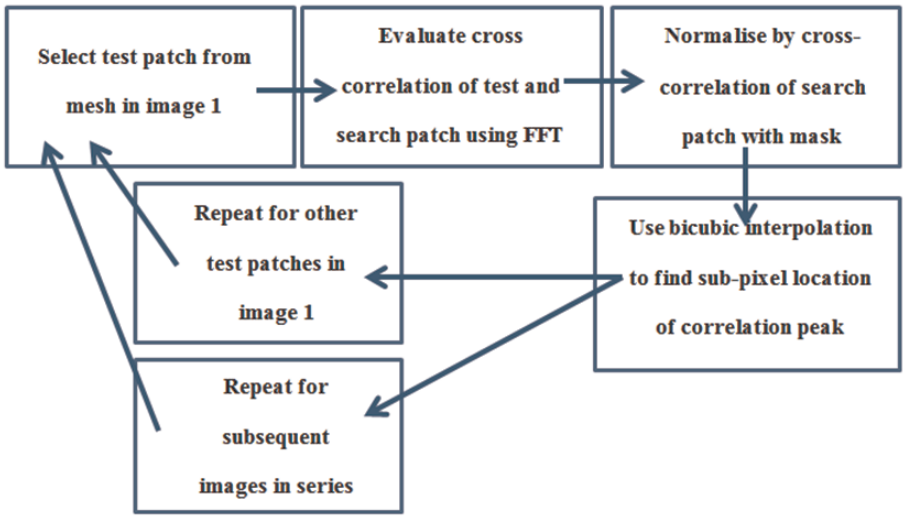


Figure 6.5. Flowchart of the GeoPIV Analysis Procedure (After White and Take, 2002).

This process is repeated for the entire mesh of patches within the image, and then repeated for each image within the series, to produce complete trajectories of each test patch.

White and Take (2002) indicated that the performance of a measurement system can be assessed by considering the errors associated with accuracy and precision. Accuracy is defined as the systematic difference between a measured quantity and the true value. Precision is defined as the random difference between multiple measurements of the same quantity. The accuracy depends on the process used to convert from image-space to object-space coordinates.

PIV is necessarily a 2-D procedure when used with geotechnical materials, whereas it is a fact that deformations generate in three dimensions. However, here it is assumed that the deformations observed on the surface are constant with depth into the material (Pan *et al.*, 2009).

Based on the results of GeoPIV analysis, shear and volumetric strain distribution maps, displacement vector filed and also patch deformation profile can be obtained shown in Figure 6.6. Therefore, strain distribution and geometry of the slip plane is able to detect with using these results more realistically.

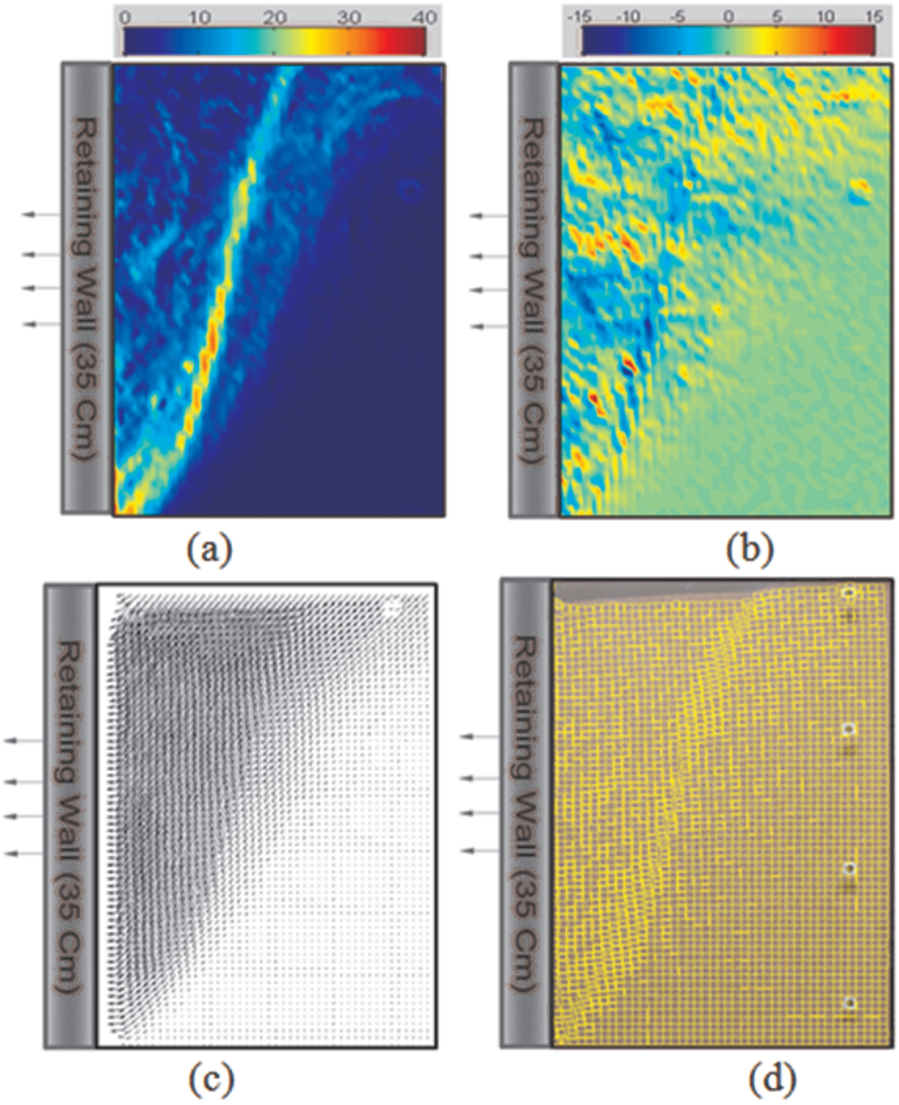


Figure 6.6. Typical PIV Results for Active Retaining Wall Translation a) Shear Strain b) Volumetric Strain c) Vector Field d) Patch Deformation Profile.

6.2.1. Determination of Patch Size

Patch size is an important factor for the precision of PIV results, since it is a strong function of defined patch size in initial mesh; the larger the patch size, the greater the precision is. According to White *et al.*, (2003), small patch size provides more details but also a greater potential for random data fluctuations. Additionally, if the patch size is too small, the GeoPIV software may not recognize the displaced patch. For this purpose, further analysis was performed to determine the optimum size (in pixels) for the test patches. A sequence of images for one specific test was analyzed considering six patch sizes to determine the most appropriate patch size for subsequent analysis. The patches measured in pixels were sized as 128*128, 64*64, 32*32, 128*64, 64*32 and 64*16. The calibrated shear strain and vector plots for each analysis are shown in Figure 6.7. At small patch sizes, unnecessary details are visible in strain maps that are the results of generated wild vectors in displacement field. Moreover, another disadvantage of very fine mesh is the long-time consumed during the analyzing process. However, with larger patch sizes, there are missing details in displacement field and also a crude shear strain map is observed (i.e. 128*128 pixel patches). Larger patch size leads to smaller scatter (Slominski *et al.*, 2006). It means that deformation could appear much smoother with selecting the coarser mesh of patches, but it would reduce the sensitivity of information like any other smoothing operation. A decision is made on choosing 64*64 pixel sized patches, of which optimized and appropriate for slip plane determination and visualization of deformation mechanism in an acceptable analysis time.

The disadvantages of the PIV method are that strains inside the material cannot be traced (only those on the surface of the specimen) and the size of the investigated specimen cannot be too large, otherwise evaluation of results takes too long (Slominski *et al.*, 2006, Niedostatkiewicz *et al.*, 2011). Additionally, due to the presence of soil-wall friction, the PIV analyses a displacement distribution under friction (Niedostatkiewicz *et al.*, 2011).

White *et al.*, (2003) suggest that an upper bound for their software's precision

error (p_{pixel}) is given by the empirically-derived expression. Dividing this error (p_{pixel}) by the image width in pixels, the precision can be expressed as a fraction of the field of view (FOV), as expressed in Equation 6.1:

$$p_{pixel} = \frac{0.6}{L} + \frac{150000}{L^8} \tag{6.1}$$

where L is the size of the search patch in pixels. For the present study, L = 64 pixels, so precision error is calculated as 0.009 pixel according to Equation 6.1. Dividing this by the dimension of the FOV (also in pixels) gives the precision as a function of field of view. Measurement precision was reached at 1/155000 of FOV and this is significantly superior to the precision of other image based deformation measurement systems (White *et al.*, 2003).

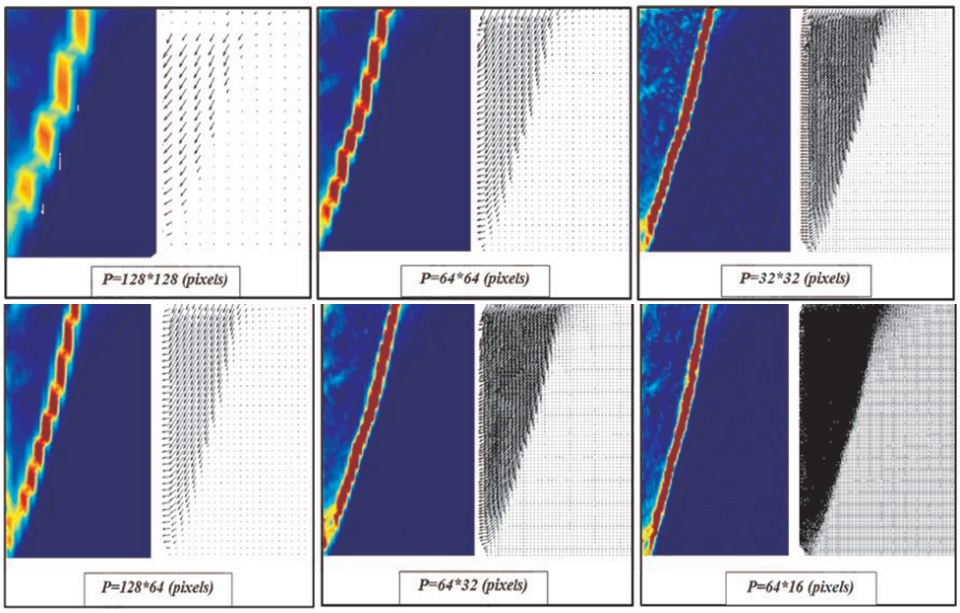


Figure 6.7. Determination of Patch Size.

Control markers were located at known intervals, which are 10 cm vertically and 5 cm horizontally, on the plaxiglass surface shown in Figure 6.8. They were placed on the investigated surface to transform "image-space" displacements (in pixels) into "object-space" displacements (in millimetres or equivalent). Control markers do not displace with respect to the boundary of the deforming material, so that tracking of these markers provides any movement of the capturing device to be eliminated (White,

2002). A disadvantage of the placed of control markers is that they must be placed close to the area of interest in the image, so that their existence may obscure some wild vectors.

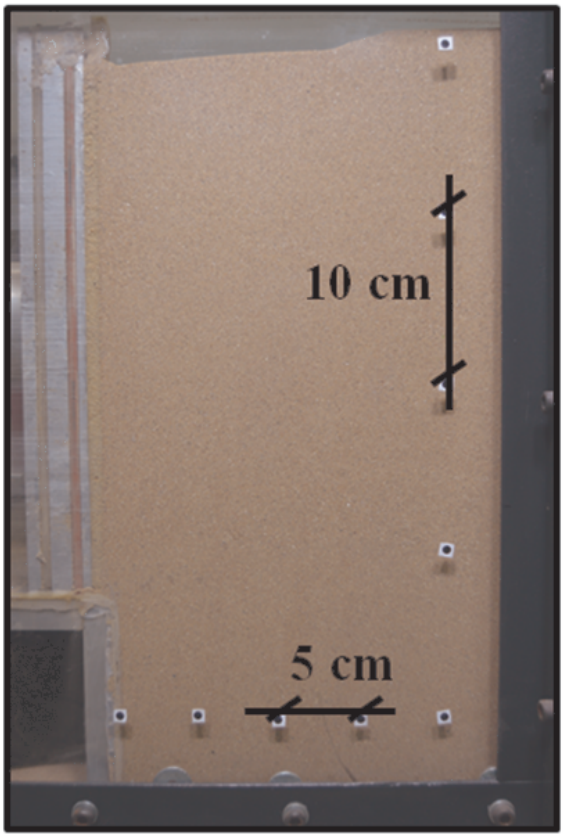


Figure 6.8. Control Markers on Side of the Wall.

7. RESULTS

7.1. Slip Plane Geometry based on PIV at Active State

GeoPIV provides detailed cumulative shear (ε_s) and volumetric strain (ε_v) maps for every stage of the tests. Through the analyses of these strain maps, shear strain localization can be detected and the evolution of slip plane geometry with wall displacement can be observed.

Strain maps are color-coded for visualization of strain magnitude distribution within the model. Following soil mechanics notation, contraction (volume decrease) is considered as positive (+) and dilation (volume increase) as negative (-). Color-scales of each image were adjusted to achieve highest visual contrast, so that slip surface would be easily distinguishable. A coordinate system with its origin located at the bottom of the model wall is established in order to be able to quantify slip plane geometry using Plot Digitizer program (Figure 7.1). Plot Digitizer is a Java program utilized for digitizing the scanned plots of functional data. This program offers users to take a scanned image of a plot (in GIF, in GIF, JPEG, or PNG format) and digitize values off the plot by clicking the mouse on each data point. Then the data points are obtained as a text file. This program can be used both linear and logarithmic axis scales. Additionally, Plot Digitizer can be used to digitize other types of scanned data, such as scaled drawings.

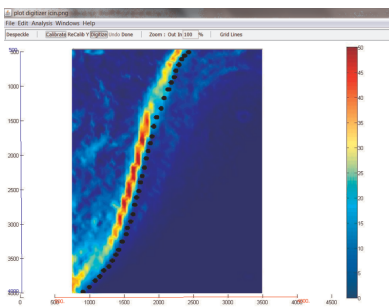


Figure 7.1. Control Markers on Side of the WallQuantification of Slip Plane Geometry with Using Plot Digitizer Program.

Furthermore, established coordinate system is made non-dimensional by normalizing the axes with model wall height (H_w). Then, unit-independent quantification of the failure surface becomes possible. X and Y coordinates of the points along the slip plane are measured as shown in Figure 7.2a and Figure 7.2b by means of the plot digitizer program. In this respect, outer edge of failure surfaces are marked with colored dots and quantified for both B (away from the model wall) and H (along the length of the model wall) directions as shown in Figure 7.2a and Figure 7.2b. Coordinates of all points along the slip plane, horizontal ($B_{1,2,..,n}$) and vertical ($H_{1,2,..,n}$), are measured with respect to the position of the wall prior to any displacement.

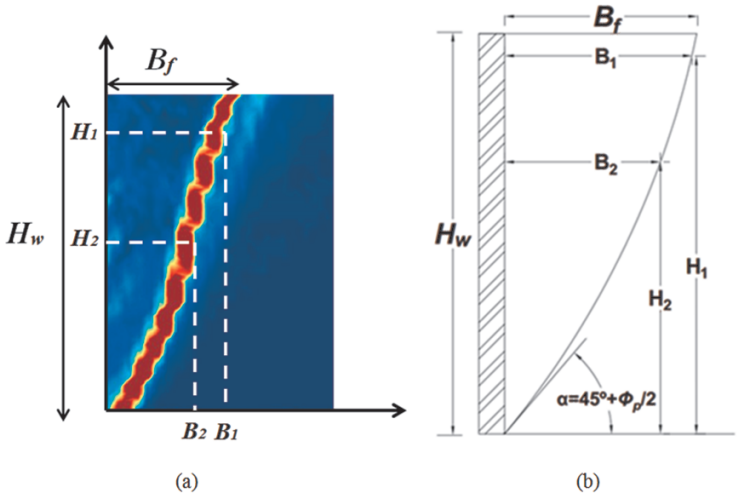


Figure 7.2. Detection of the Failure Surface Geometry a) as Plotted on the Cumulative Shear Strain Map and b) as Shown with an Illustration.

Using shear and volumetric strain maps, slip surface can be identified by following the locus of maximum strain points. Evaluating defined slip surfaces, it is observed that greater backfill densities correspond to steeper, more intense, uniformly distributed and better developed shear bands as shown in Figure 7.3 during active wall failures. This is an outcome of higher internal friction (ϕ'_p) and dilatancy (ψ_p) angles associated with greater relative densities. This fact is also supported by Loukidis and Salgado (2012) in their study based on FE simulations. Analyzing the consecutive stages of the test from start to finish for tests with high dilatancy angles, it has been observed that deformations concentrate to a continuous region even during the initial stages of

the test. This region, during the stages leading up to failure, evolves into slip surface (Figure 7.4). As soon as a slip plane forms, deformations become restricted to the region between the slip surface and the wall shown in Figure 7.4 and Figure 7.5. This area is referred to as the failure wedge. Furthermore, the slip surface becomes more and more distinct only with increasing wall movement (Figure 7.4 and Figure 7.5). This kind of shear localization yields to classical geotechnical problem of earth thrust on a retaining wall (Lesniewska *et al.*, 2012). To put it in other words, the deformation within the backfill is initially slightly diffused and with wall displacement it becomes more and more distinct. This idea was also supported by Lesniewska *et al.*, (2012). It is known that the incremental behavior of granular material may significantly differ from its averaged behavior (Lesniewska *et al.*, 2012). The evolution of dilatant behavior with displacement can be visualized using a volumetric strain map as shown in Figure 7.5. As a result, it can be stated that progressive deformation was monitored along the slip zones both in volumetric and shear strains.

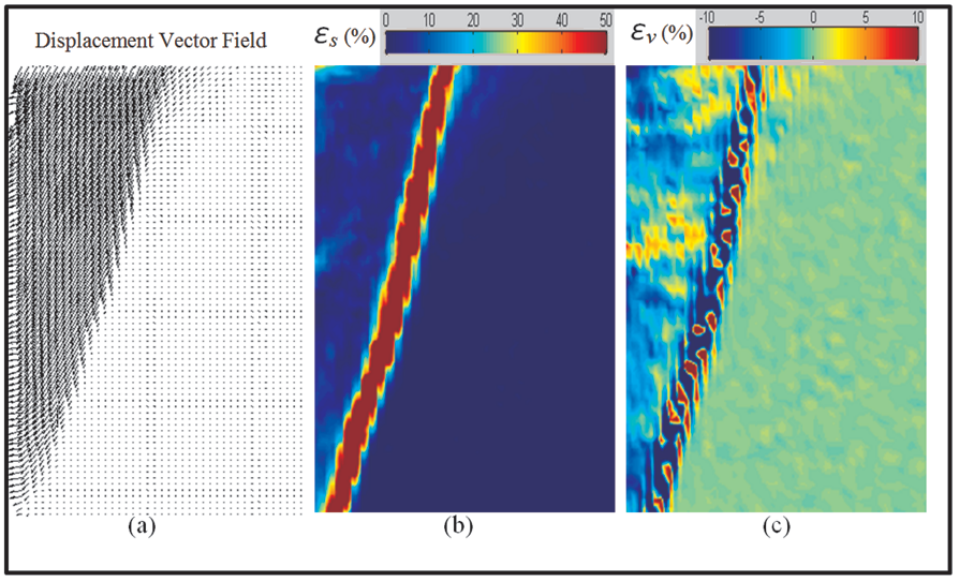


Figure 7.3. Localization of Cumulative Strains in Initially Dense Sand Based on as Obtained from PIV Analyses (a) Vector Field of Deformation, (b) Distribution of Shear Strains (ε_s), (c) Distribution of Volumetric Strains (ε_v).

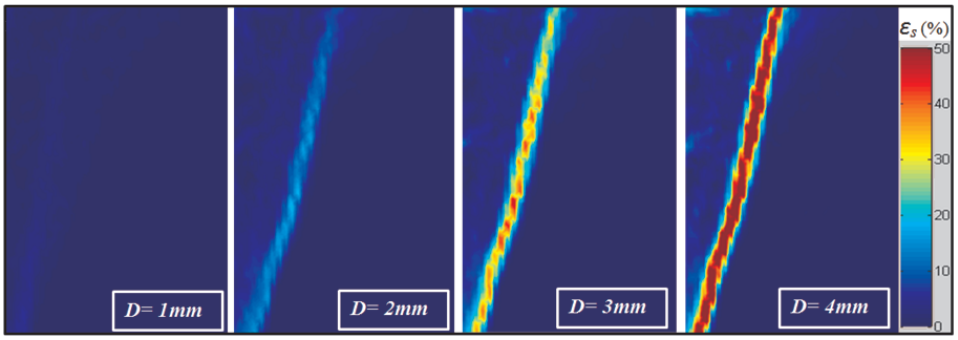


Figure 7.4. Shear Strain Concentration and Failure Surface Evolution with Respect to Rigid Retaining Wall Movement.

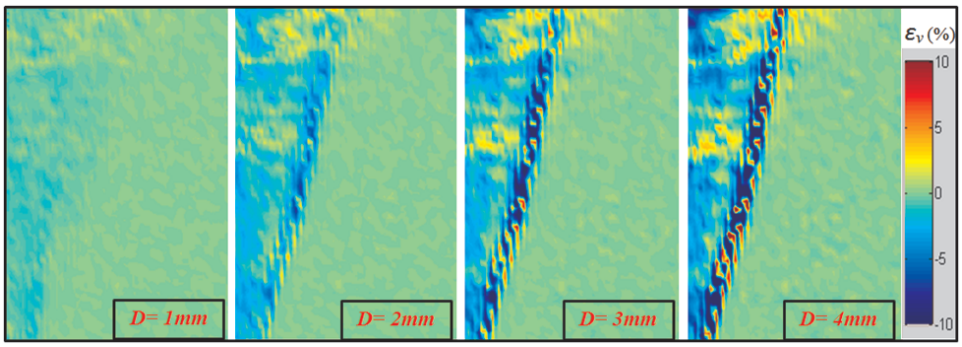


Figure 7.5. Volumetric Strain Concentration and Failure Surface Evolution with Respect to Rigid Retaining Wall Movement.

As observed in Figure 7.5, both dilative and contractive deformations can be identified on volumetric strain maps obtained from PIV analyses. Accordingly along the failure band, volumetric deformation is dominantly dilative for dense backfills from Figure 7.3b and dominantly contractive for loose backfills from Figure 7.6b. Evidently in Figure 7.3b, failure surface is hardly distinguishable for loose backfills unlike for dense backfills in which failure surfaces are clearly visible. The underlying reason for this observation is that in loose backfill, contractive behavior prevails within the failure wedge, but small dilatancy is also present. In other words, in case of loose backfills, wide contractive region of the wedge shape can be observed between wall and the free soil boundary. The zone of dilatancy is much smaller than the contractive zone. Furthermore, the shear band apparently shows a non-uniform strain distribution in initially loose backfill and strains are located much concentrated at the toe of the wall. These results show the influence of dilatancy on localization of shear strains in granular

materials.

Based on this observation, it is possible to propose that the geometry of shear planes can be quantified as functions of dilatancy angle. This proposition has its roots in plasticity theory for geomaterials (Atkinson 1981). A recent study by Niedostatkiewicz *et al.*, (2011) also supports the idea that deformation in shear zones is always related to dilatancy.

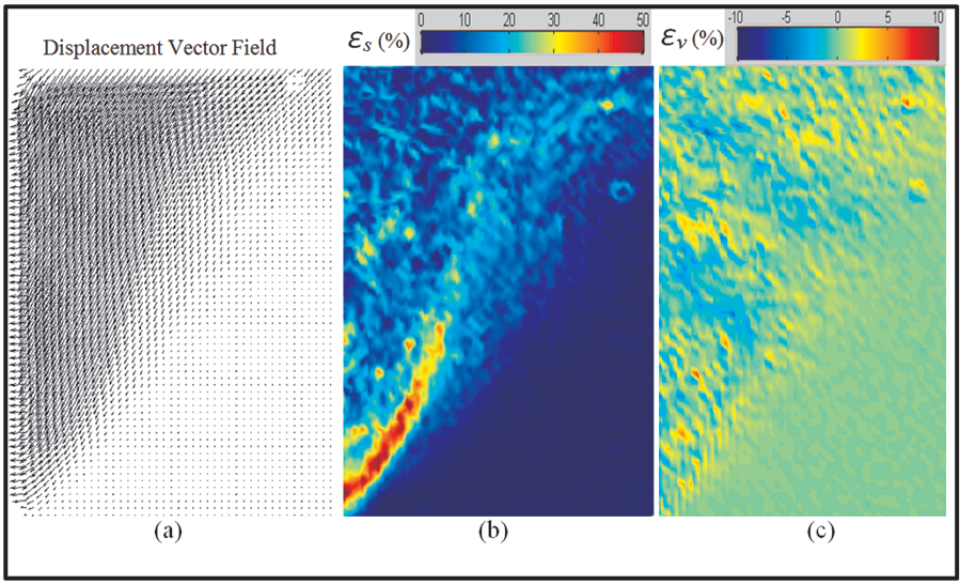


Figure 7.6. Localization of Cumulative Strains in Initially Loose Sand Based on as Obtained from PIV Analyses (a) Vector Field of Deformation, (b) Distribution of Shear Strains (ε_s), (c) Distribution of Volumetric Strains (ε_v).

According to the results of PIV analyses, general shapes of the failure surfaces were evaluated and plotted as shown in Figure 7.7. A new dimensionless coordinate system is established by normalizing the horizontal and vertical dimensions with wall height. The origin of the coordinate system is located at the initial position of the top backfill side corner of the model wall and positive directions are defined as shown in Figure 7.7. Results suggest nonlinear active failure surface geometry that links the toe of the rigid retaining wall to the surface of the backfill. Figure 7.7 shows the geometries of the failure surfaces identified in different model tests that correspond to failure states. Slip planes obtained from all model tests are not shown in Figure 7.7

for the sake of clarity. Dilatancy angles of backfills associated with different failure surfaces are also reported in Figure 7.7. From the analyses of slip planes, it can be clearly seen that slip plane geometries are dependent on dilatancy angles.

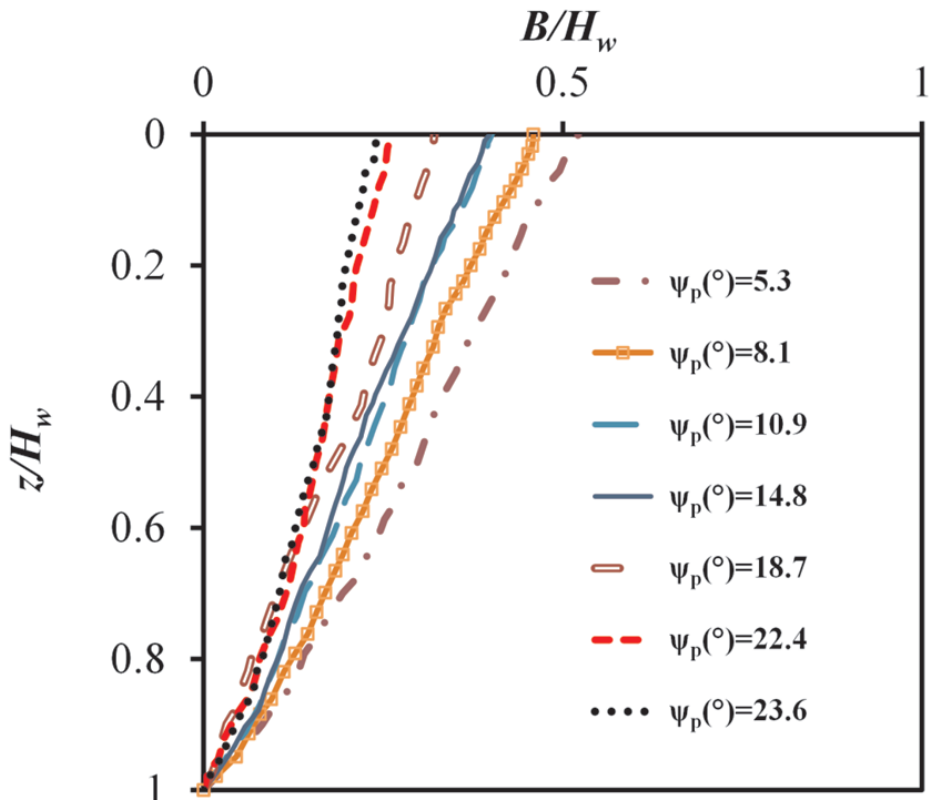


Figure 7.7. Geometries of Several Active Failure Surfaces Obtained from PIV Analyses and the Corresponding Peak Dilatancy Angles (ψ_p) of the Model Backfill Soils.

7.2. Influence of Interface Friction between wall and backfill at Active Failure

In order to observe the influence of interface friction angle between wall and backfill (δ), few model tests were conducted on backfills with different densities. To obtain a rough wall surface, sandpaper was glued to the face of the wall. The angles of friction between the sandpaper and the backfill were determined by conducting direct shear box tests. According to results, the produced angles of friction were varied in the range between 35^o and 45^o depending on the backfill densities.

The results of the tests are shown in Figure 7.8. Based on the results, it is clearly seen that the geometries of the slip planes are practically not affected by the variations in interface friction angles (δ). Therefore, it is stated that effect of wall friction on the shape of the slip surface is small and can be ignored at active failure state as suggested by Craig (2004).

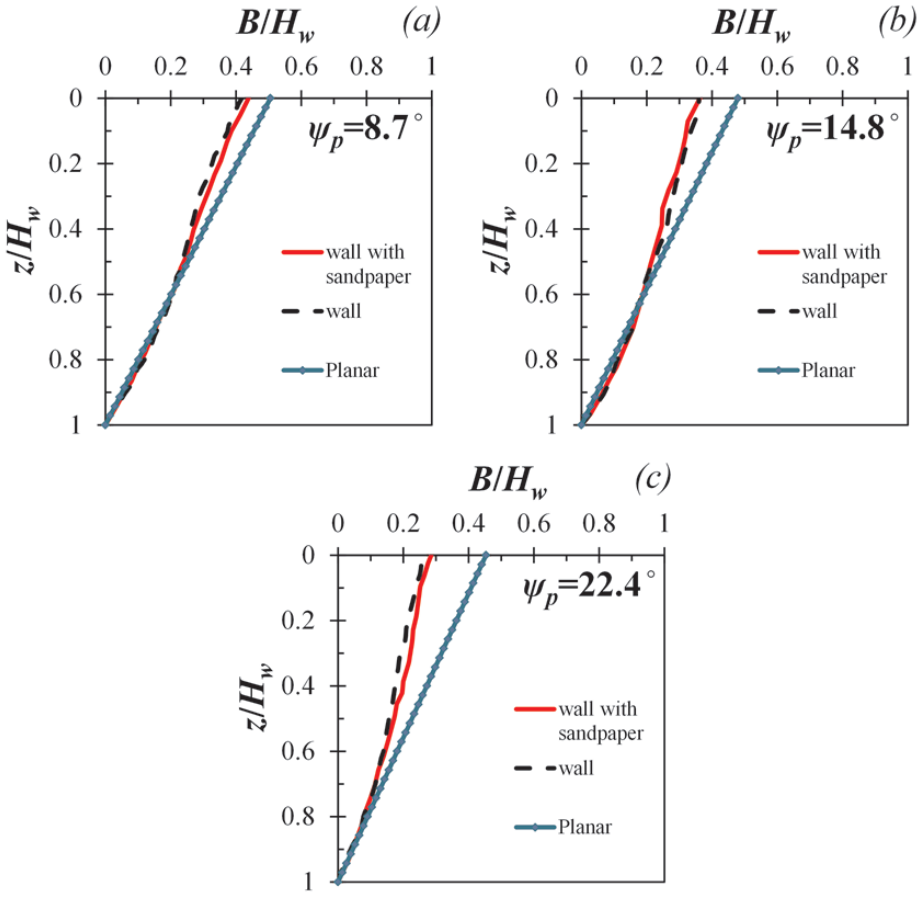


Figure 7.8. Evaluation of the Influence of Wall Friction on Active Failure Plane Geometry.

7.3. Influence of Dilatancy on Slip Plane Geometry at Active State

Results given in Figure 7.3, Figure 7.6 and Figure 7.7 showed that active slip plane geometry is dependent on the dilatant properties of the backfill. However, quantification is necessary to utilize this dependency for engineering purposes. Accordingly, relationships between general characteristics of the slip planes and the associated dilatancy angles are investigated. Using the normalized coordinate system defined in

Figure 7.2, the general characteristics are defined using normalized widths (B/H_w) at various depths. Figure 7.9 shows the normalized widths of the identified active failure surfaces versus the peak dilatancy angles of the backfill soils for three different depths; the first at the backfill surface (z/H_w=0), the second at depth z=0.4H$_w$, and the third one is at depth z=0.7H$_w$. Model tests are color-coded and the dilatancy angles of the backfills are reported in the legend of Figure 7.9. Clearly, active failure surfaces are dependent on ψ_p at all levels and results suggest inversely proportional linear ψ_p-B/H_w relationships for all the depths considered.

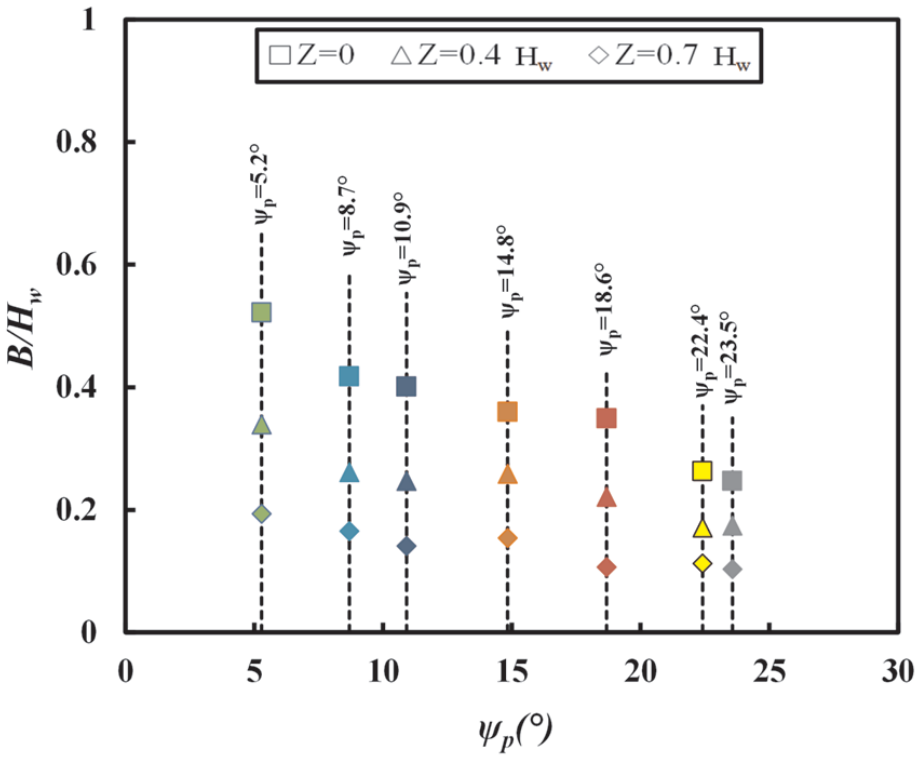


Figure 7.9. B/H_w Data Obtained from Model Tests Plotted against the Dilatancy Angles (ψ_p) of Respective Backfill Soils. Data Points that Correspond to Different Tests can be Distinguished from the Colors of the Bullets and Their Respective ψ_p Angles.

Moreover, highly sensitive sensors embedded on the model retaining wall provide the variation of lateral earth pressure with respect to wall movement. In order to calculate K_a values, pressure sensors data was used to obtain lateral earth pressure as shown in Figure 7.10. Then, vertical effective stress was calculated and K_a values were

calculated with using Equation 7.1.

$$K_a = \frac{\sigma'_x}{\sigma'_z} = \frac{\sigma'_x}{\gamma' z} \tag{7.1}$$

Here, σ'_x and σ'_z are horizontal and vertical effective stress, respectively; and z is the depth of the retaining wall and γ is the unit weight of the soil. Then, K_a values were obtained for each sensor (Figure 7.11). As a result, variations of active lateral earth pressure (K_a) values are available and are also plotted on Figure 7.12 with respect to dilatancy angle. It is clear that the form of the K_a-ψ_p relationship has the same form as that of $B_f/H_w - \psi_p$ relationship. Therefore, it is possible to deduce from Figure 7.12 that ψ_p controls both the geometry of the slip plane and the resulting K_a value. In other words, K_a value is a direct function of slip plane geometry which is dependent on the dilatant properties of the soil at its at-rest state. Furthermore, the relationships are quantifiable and prove that the influence of ψ_p on lateral earth pressures should be considered for calculating more accurate K_a values. This can be achieved through Equation 5.1 which allows the calculation of ψ_p using soil properties at the at rest state.

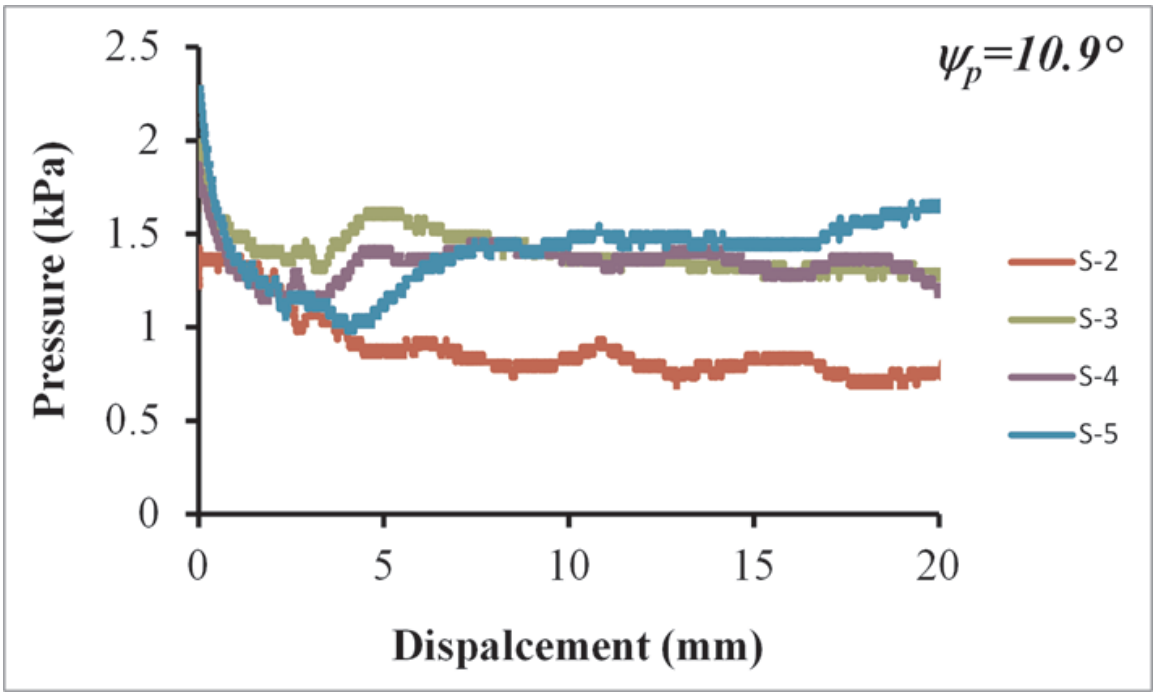


Figure 7.10. Changes in Active Lateral Earth Pressure with wall Movement.

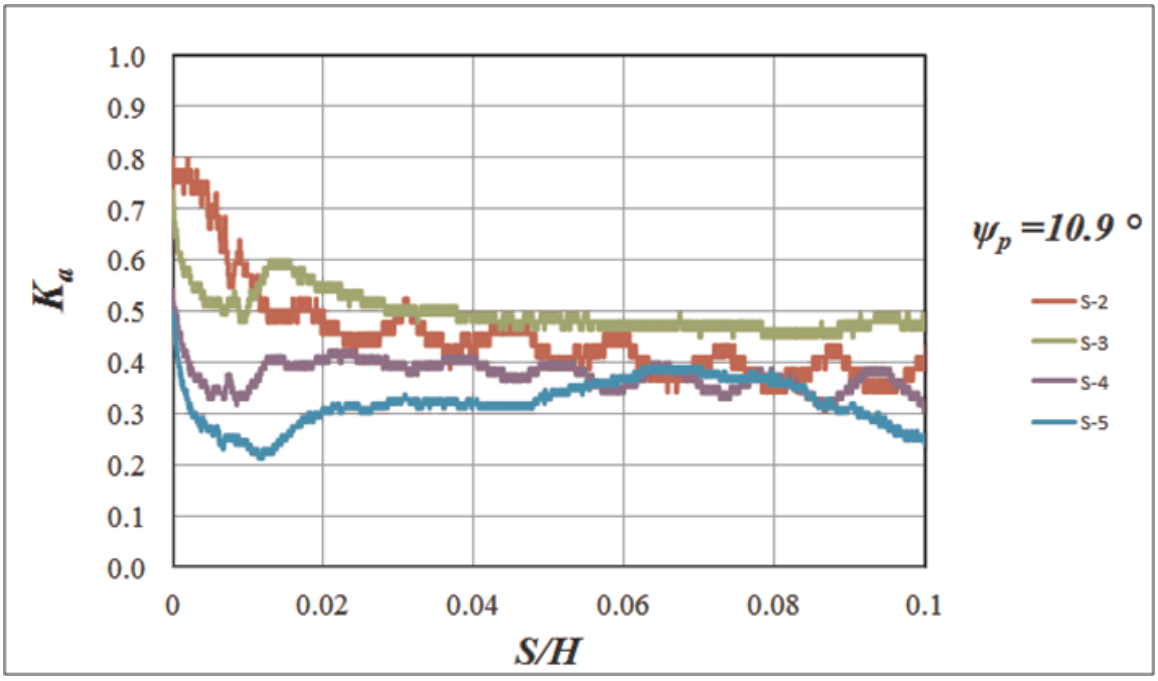


Figure 7.11. Changes in Active Lateral Earth Pressure Coefficient (K_a) with wall Movement.

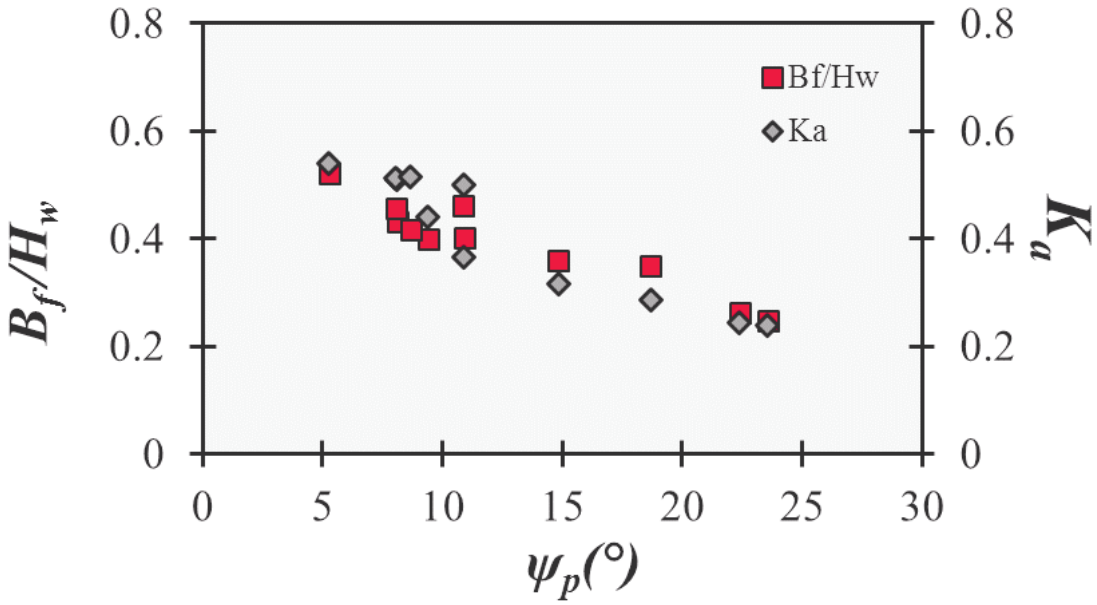


Figure 7.12. Variation of Dilatancy Angle (ψ_p) within the Backfill with respect to Normalized Failure Surface Width (B/H_w) and Active Lateral Earth Pressure Coefficient (K_a).

7.4. Determination of Slip Plane Geometry

PIV analyses of the images of model tests at failure revealed that active failure surface is not planar. When the general forms of the failure planes shown in Figure 7.7 are examined, parabolic function is identified as the most suitable mathematical function for numerical identification. In literature, the boundary conditions for a parabolic failure surface are defined by Spangler and Handy (1984). According to Spangler and Handy (1984), equation for parabolic failure surfaces as shown in Figure 7.13 is defined as a 2^{nd} order parabolic function as shown below:

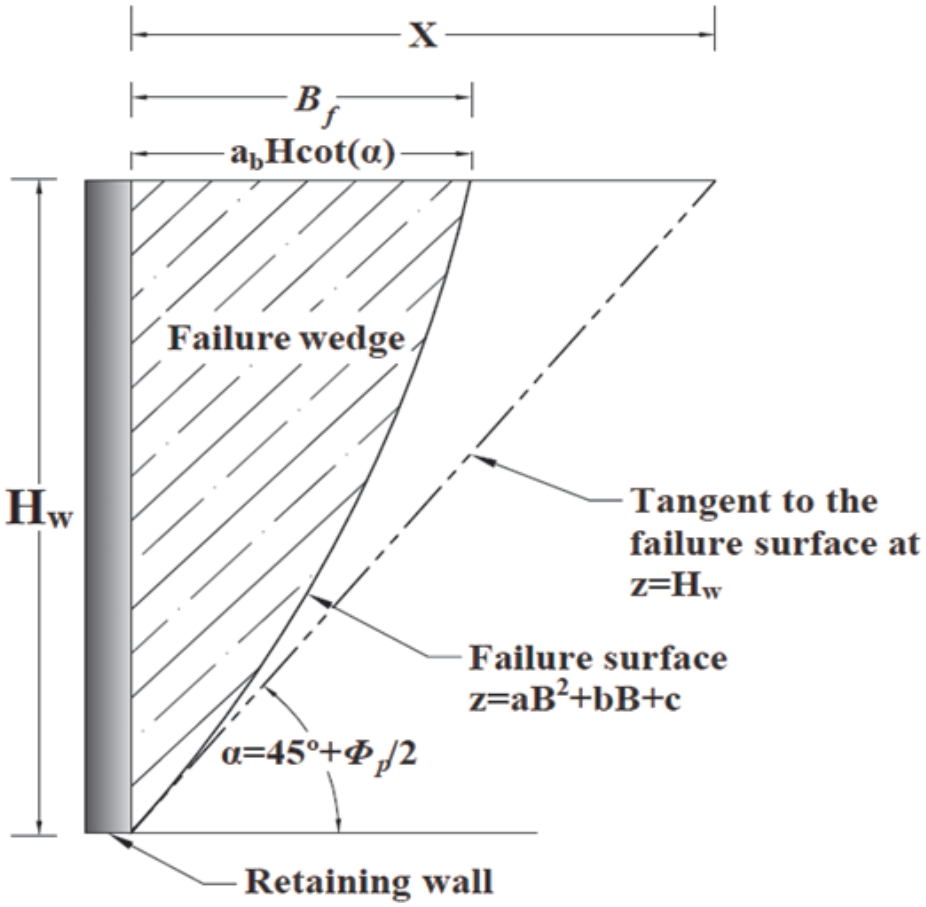


Figure 7.13. Shape of the Assumed 2^{nd} Order Parabolic Failure Surface and the Depiction of the Geometrical Ratio a_b.

$$z = aB^2 + bB + c \tag{7.2}$$

where z defines the vertical coordinate and B defines the horizontal distance from the retaining wall to the failure surface at a particular depth z as depicted in Figure 7.2. Using the boundary conditions, constants of the parabolic failure surface can be obtained as follows:

$$z = H_w, B = 0 \tag{7.3}$$

$$z = H_w \rightarrow \frac{dz}{dB} = -\tan(\alpha) \tag{7.4}$$

$$z = 0 \rightarrow B = (a_b) H_w \cot(\alpha) \tag{7.5}$$

where a_b is defined as the ratio of width of slip plane at ground surface for parabolic failure surface (B_f) to the width of planar slip plane (x) at ground surface. Distance x is measured horizontally between the wall and the point at which the tangent to the initial portion of the slip plane emerges at the backfill surface, as illustrated in Figure 7.13. As expected, magnitude of a_b is dependent on the peak dilation angle (ψ_p) of the backfill. Using the above three boundary conditions, the constants a, b, and c are obtained as follows:

$$a = \left[(a_b - 1) / ({a_b}^2 H_w) \right] \tan^2(\alpha) \tag{7.6}$$

$$b = -\tan(\alpha) \tag{7.7}$$

$$c = H_w \tag{7.8}$$

Inserting the constants given in Equation 7.6 Equation 7.7 and Equation 7.8 into Equation 7.2, parabolic equation for the active failure surface is obtained as:

$$z = \left(\left[{(a_b - 1)}/{(a_b^2 H_w)} \right] \tan^2(\alpha) \right) B^2 - \tan(\alpha)\, B + H_w \tag{7.9}$$

Even though α is based on soil properties and H_w is the height of the wall and therefore can be directly input into Equation 8, value of a_b is not defined as of yet. However, as shown in Figure 7.7 and Figure 7.9, geometry of the active slip plane is dependent on the dilatant properties of the backfill. Therefore, in order to investigate the relationship between a_b and ψ_p, a_b values measured at the active state for all model tests are plotted against $\tan(\psi_p)$ of backfill soils as shown in Figure 7.14.

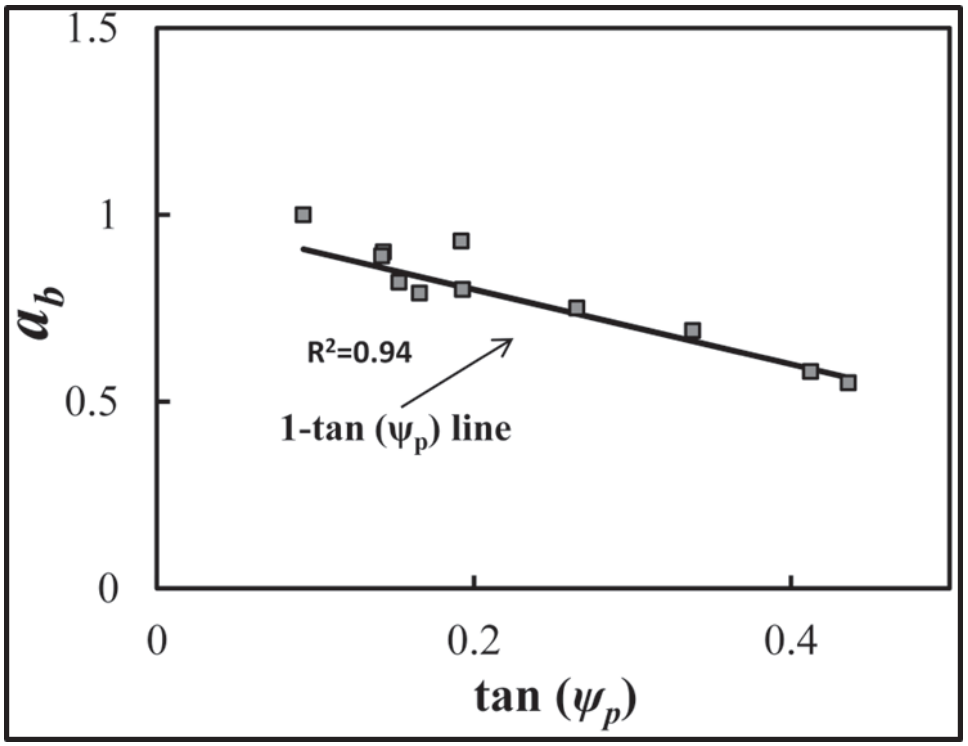


Figure 7.14. a_b-tan(ψ_p) Relationship Obtained using the Data Gathered from Retaining Wall Model Study at Active State.

The reason for using the tangent of ψ_p in Figure 7.14 is to obtain a unit indepen-

dent relationship. Clearly, empirical data agrees with the relationship shown below:

$$a_b = (1 - \tan \psi_p) \tag{7.10}$$

By defining a_b as a function of ψ_p, geometry of the active failure surface can be calculated as a function of soil properties (ϕ'_p and ψ_p) and problem geometry (H_w). Resulting parabolic function is given Equation 7.11.

$$\begin{aligned} z = &\left(\left[(-\tan(\psi_p))\Big/\left((1-\tan(\psi_p))^2 H_w\right)\right]\tan^2\left(45^\circ + \tfrac{\phi'_p}{2}\right)\right)B^2 \\ &- \tan\left(45^\circ + \tfrac{\phi'_p}{2}\right)B + H_w \end{aligned} \tag{7.11}$$

Accuracy of Equation 10 in predicting active slip planes is examined using the data of retaining wall physical model tests. For this purpose, active failure surfaces calculated using Equation 7.11 are compared to active failure surfaces obtained by PIV analyses. Results are shown in Figure 7.15. It is clearly seen that shapes of the predicted and measured failure surfaces are approximately the same.

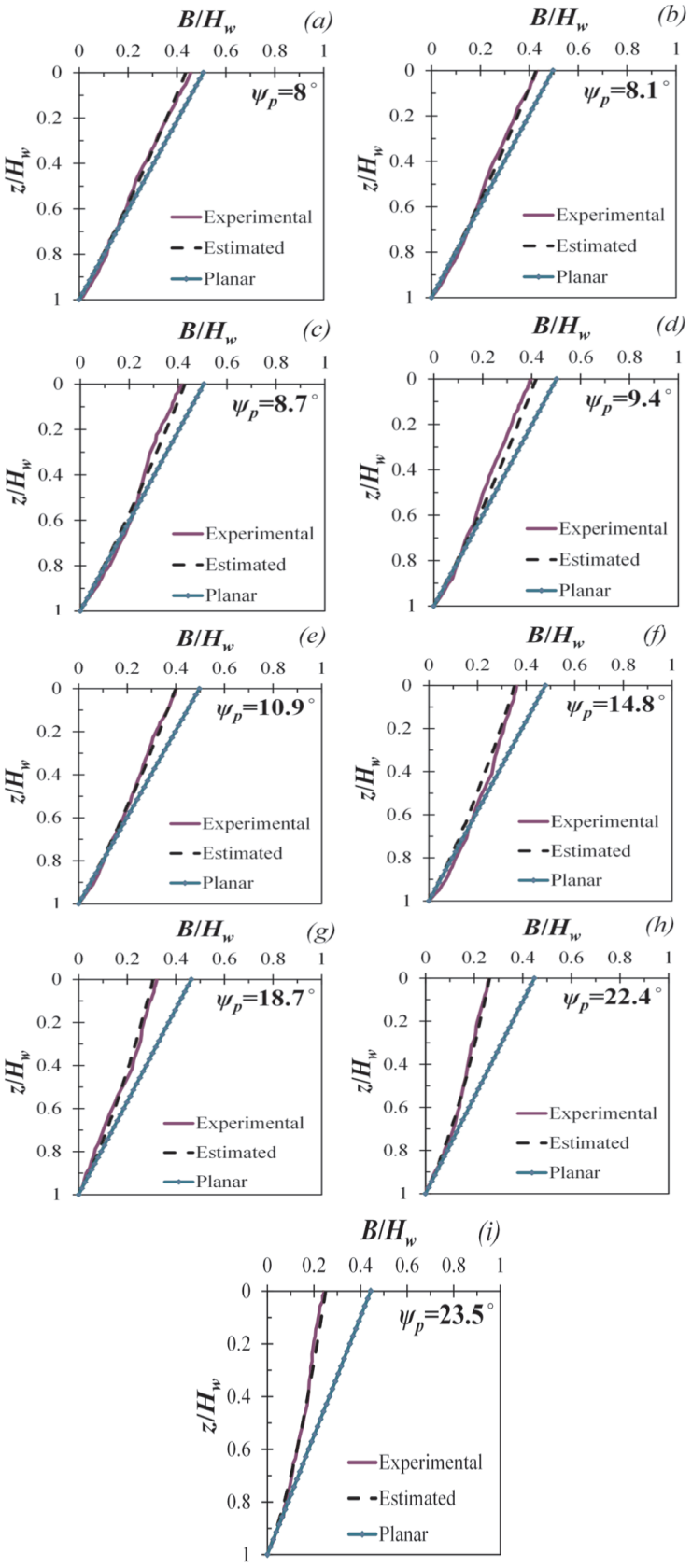


Figure 7.15. Comparisons of Calculated Failure Surfaces to the Measured Ones Obtained Using PIV Analyses, Plotted on a Normalized Scale.

7.5. Slip Plane Geometry based on PIV at Passive State

In order to simulate passive failure condition, the model wall slowly moved toward the soil mass in translational mode. According to PIV analyses, general forms of the slip planes were evaluated and plotted for different dilation angles (ψ_p) at the passive failure state with the same procedure described above for the determination of active slip plane geometry. In passive slip surface determination the only difference is that the displacement vector field (Figure 7.16) was used instead of strain map to identify the slip plane, since strain map could not be obtained for passive failure state due to presence of steel braces located on the plexiglass side walls. These braces lead to dark areas on the failure wedge so the slip planes cannot be observed entirely.

Therefore, displacement vector field was obtained for each image and some of them are shown in Figure 7.16. Briefly, a new dimensionless coordinate system is established by normalizing the horizontal and vertical dimensions with wall height by employing plot digitizer software (Figure 7.17). The origin of the coordinate system is located at the initial position of the top backfill side corner of the model wall and positive directions are defined as shown in Figure 7.7. Results show that nonlinear passive slip plane geometry that links the toe of the rigid retaining wall to the surface of the cohesionless backfill. Figure 7.18 illustrates the geometries of the slip planes identified in different model experiments at passive failure state. Slip planes obtained from all model tests are not shown in Figure 7.18 for the sake of clarity. Dilatancy angles of backfills related to different slip surfaces are also reported in Figure 7.18. Based on the analyses of slip planes obtained by model tests, it can be clearly seen that slip plane geometries are also dependent on dilatancy angles (ψ_p).

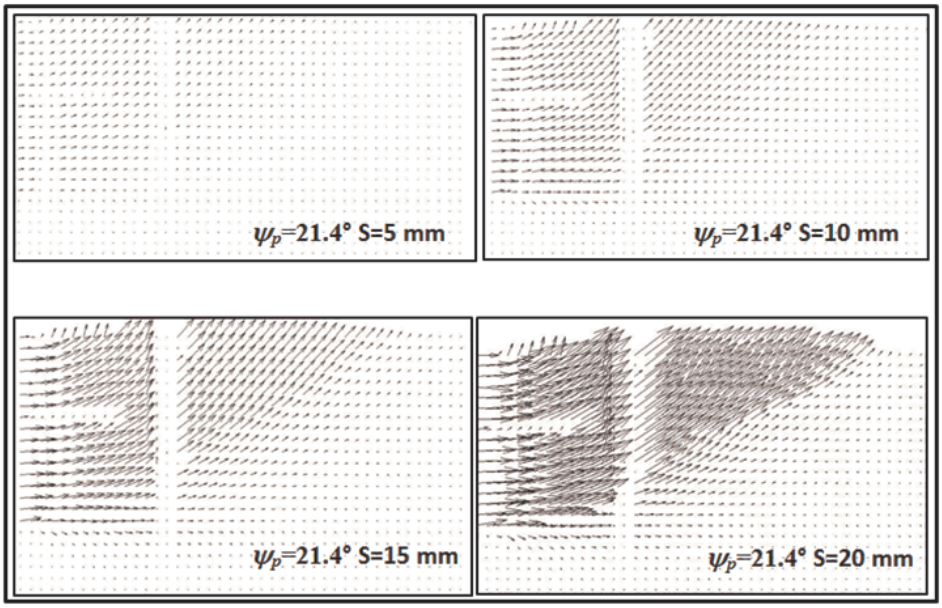


Figure 7.16. Displacement Vector Field for Initially Dense Sand with Different Horizontal Wall Displacement.

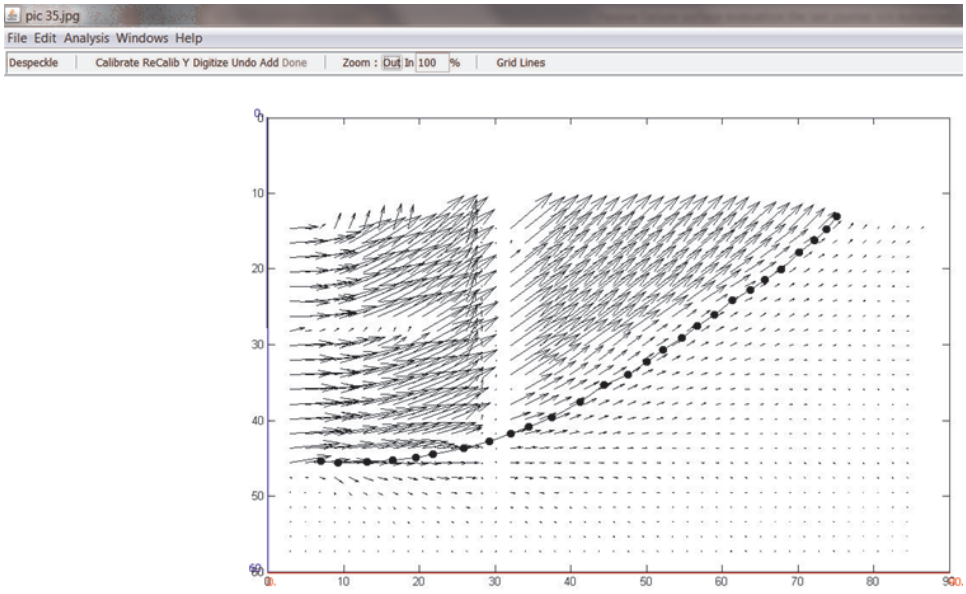


Figure 7.17. Determination of Slip Plane for Passive Failure state with using Plot Digitizer Software.

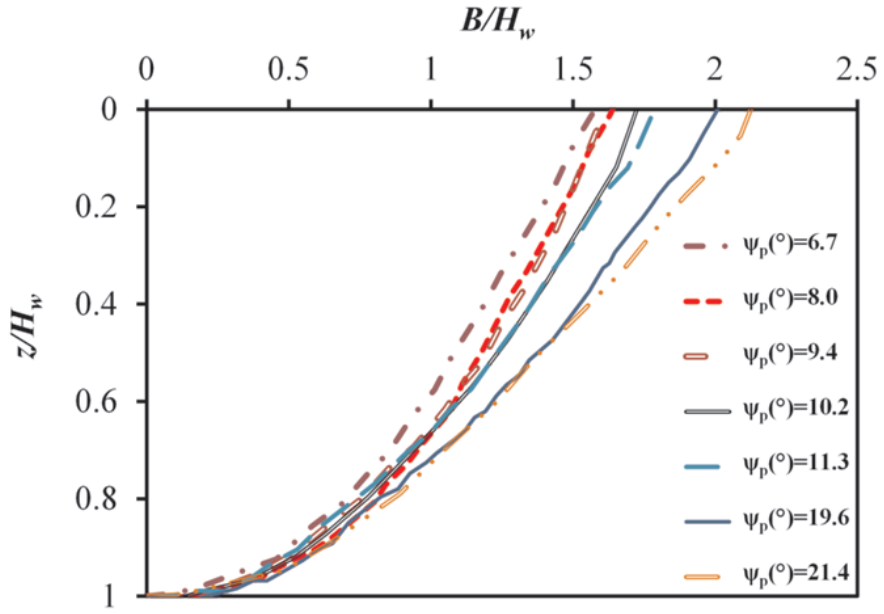


Figure 7.18. Geometries of Several Passive Failure Surfaces Obtained from PIV Analyses and the Corresponding Peak Dilatancy Angles (ψ_p) of the Model Backfill Soils.

7.6. Influence of Dilatancy on Slip Plane Geometry at Passive State

The identified passive failure surfaces at surface (B_f/H_w) versus the peak dilatancy angles of the backfill soils was plotted in order investigate the effect of dilatancy on passive slip plane (Figure 7.19). It should be noted from this figure that the relationship exists between the passive slip plane obtained with model tests and peak dilatancy angle (ψ_p). Therefore, it may be deduced that peak dilatancy angle also governs the passive failure mechanism. Moreover, highly sensitive pressure sensors embedded on the model retaining wall also provide the variation of lateral earth pressure with respect to wall movement for passive failure state. Therefore, calculation of K_p values were available. For this purpose, pressure sensors data was used to obtain lateral earth pressure as shown in Figure 7.20. Then, vertical effective stress was calculated and K_p values were calculated with using Equation 7.12.

$$K_p = \frac{\sigma'_x}{\sigma'_z} = \frac{\sigma'_x}{\gamma' z} \tag{7.12}$$

Here, σ'_v and σ'_z are horizontal and vertical effective stress, respectively; and z is the depth of the retaining wall and γ is the unit weight of the soil. Then, K_p values were obtained for each sensor (Figure 7.21).

As a result, variations of passive lateral earth pressure (K_p) values are available and are also plotted on Figure 7.19 with respect to dilatancy angle (ψ_p). It is possible to deduce from Figure 7.19 that there is a relationship between dilatancy angle (ψ_p) and the experimental value of passive earth pressure coefficient (K_p). It is clear that the form of the K_p-ψ_p relationship has the same form as that of $B_f/H_w - \psi_p$ relationship. Therefore, it is possible to deduce from Figure 7.19 that ψ_p controls both the geometry of the slip plane and the resulting K_p value. In other words, K_p value is a direct function of slip plane geometry which is dependent on the dilatant properties of the soil at its at-rest state. Furthermore, the relationships are quantifiable and prove that the influence of ψ_p on lateral earth pressures should be considered for calculating more accurate K_p values. This can be achieved through Equation 5.1 which allows the calculation of ψ_p using soil properties at the at rest state. Fang *et al.*, (2002) (based on the experimental study), Shiau and Smith (2006) and Tejchman and Tantono (2007) (based on the numerical simulations) also support these results and suggested that the dilation and the strength reduction of dense backfill should be considered in calculating passive earth pressure.

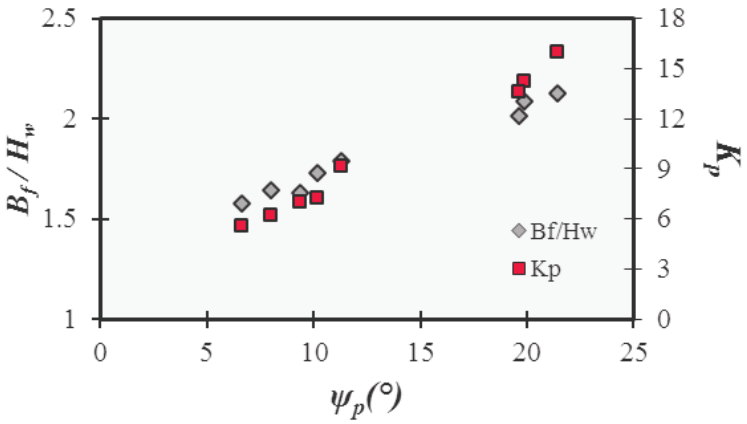


Figure 7.19. Variation of Dilatancy Angle (ψ_p) within the Backfill with respect to Normalized Failure Surface Width (B_f/H_w) and Passive Lateral Earth Pressure Coefficient (K_p).

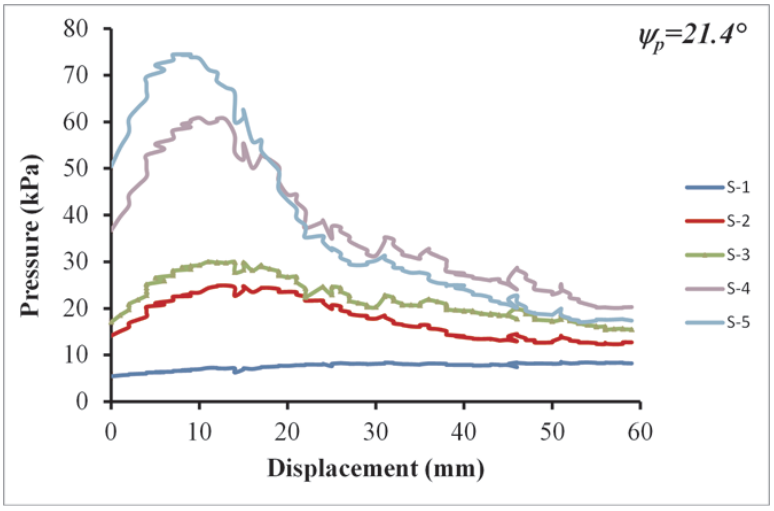


Figure 7.20. Changes in Passive Lateral Earth Pressure with wall Movement.

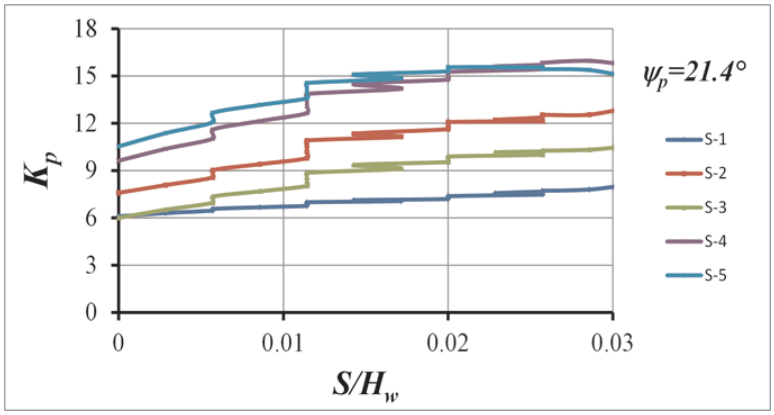


Figure 7.21. Changes in Passive Lateral Earth Pressure Coefficient (K_p) with wall Movement.

In order to investigate the relationship between a_b and ψ_p as mentioned in active failure condition, a_b values measured at the passive state for all model tests are plotted against tan (ψ_p) of backfill soils as shown in Figure 7.22. Evaluating the results, it is stated that dilatancy angle (ψ_p) influences passive slip plane. However, dilatancy angle (ψ_p) and internal friction angle (ϕ') are not enough to identify the passive slip plane. Since, the interface friction between wall and backfill gain much more importance for passive failure conditions and the resulting passive slip planes. Therefore, in order to identify the passive slip plane geometry by a simple equation, an experimental study considering different interface friction angles between wall and backfill should be conducted. Then, passive slip plane may be quantified using a 2^{nd} order parabolic

function.

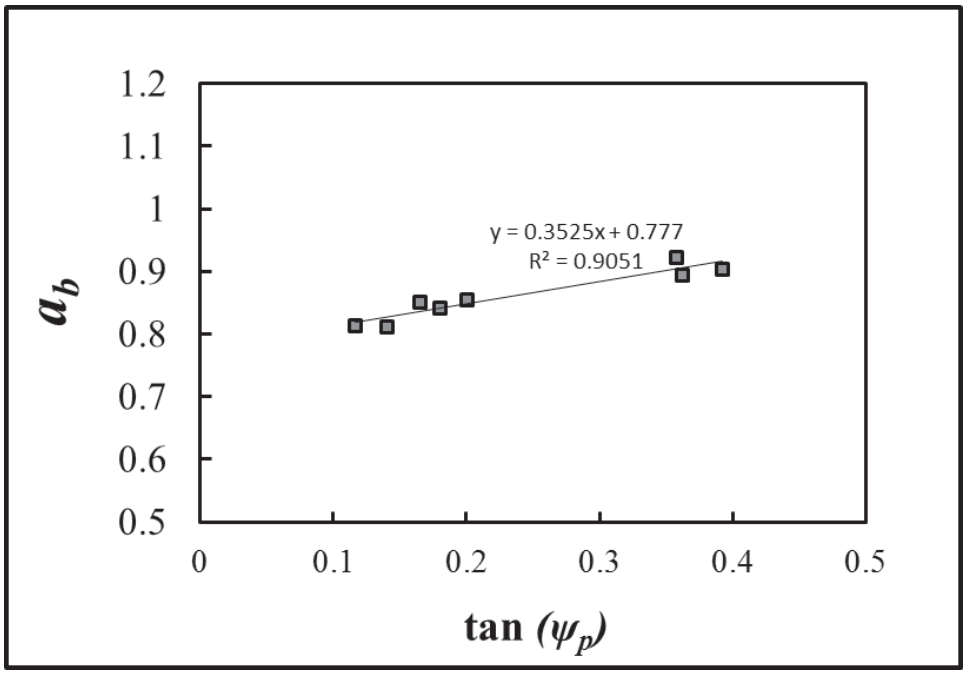


Figure 7.22. a_b-tan(ψ_p) Relationship Obtained using the Data Gathered from Retaining Wall Model Study at Passive State.

8. SHEAR BAND FORMATION

Strain map intensity profiles were used to have a quantified understanding of strain distribution within failure wedge behind retaining wall. A visual interpretation of the strain change patterns can be obtained using MATLAB to convert initially recorded RGB images to black and white images, based on 0-255 grey scale, the lowest possible intensity is then zero (black), and the highest 255 (white). In a gray-scale image, greater brightness corresponds to higher shear strains on shear strain map, whereas, it corresponds to reduction in volumetric strains on a volumetric strain map. Respectively, decreased brightness refers to a lower shear strain magnitude and simultaneously expansion in volumetric strain map. Figure 8.1 shows a flowchart for obtaining intensity profile of an image. The intensity profile of an image is a map for identifying the distribution of intensity values obtained from equally spaced points along a defined line segment. Some part of the procedure to obtain strain map intensity profile is recently proposed by Lesniewska and Wood (2011) and Lesniewska *et al.*, (2012), but they have not utilized it yet for detailed investigation of strain localization. Accordingly, results of active tests were analyzed using GeoPIV to quantify the strain distribution within the failure wedge and results of three tests on backfills with varying magnitudes of dilatancy angles are presented in Figure 8.2.

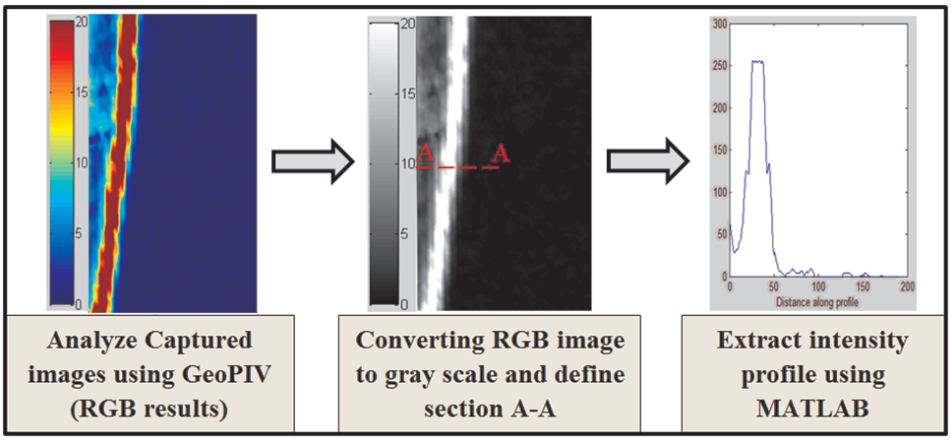


Figure 8.1. Step-by-Step Flowchart of Intensity Profile.

Based on the results, it was observed that the failure wedge and the shear band are hard to recognize within the initially loose backfill (Figure 8.2). The strain was not accumulated in the shear band; it is in a scattered form, involving multiple shear bands. However, for the initially medium dense backfill, the failure mechanism changes; although there are still non-localized shearing deformations, a distinguishable shear band appears with respect to wall movement, in which strains are remarkably greater than those in the neighboring zones. Furthermore, a dense backfill represents a totally localized shear band with intense shearing patterns. There is also a separated zone in the strain map, behind the shear band and away enough from the wall, which shows no deformation and therefore referred to as the stationary region of the backfill. The inclinations of the resulting shear bands were also measured using the strain maps and displayed in Figure 8.2. It is clearly observed from Figure 8.2 that as the dilation angle (ψ_p) increases, the shear band becomes steeper. These results are also supported by Niedostatkiewicz *et al.*, (2011) and Tehrani *et al.*, (2014). The angle of shear band inclination (θ) for each model tests were measured and the relationship between dilatancy angles (ψ_p) versus shear band inclination (θ) is presented in Figure 8.3. According to the results, it is revealed that θ varies from 58 to 72 degrees with respect to horizontal, which reveals a good idea of how density and stress state in granular media influences behavior. It is seen that shear band inclination (θ) decreased almost linearly with decreasing dilatancy angles (ψ_p). In other words, inclination of the band is higher in the backfill having higher ψ_p. So, it is stated that dilative behavior has an effect on the inclination of shear band. Saada et. al (1999) agreed with this conclusion and reported that shear band inclinations in granular material seem to depend on the internal friction angle (ϕ') and that of dilation in a combination. However, it is believed that the proposition of Saada *et al.*, (1999) is not completely correct since as shown with Equation (5.1.), ϕ'_p and ψ_p are interdependent. Therefore, according to Figure 8.3, it is seen that initial inclination of shear band can be a function of either ϕ'_p or ψ_p.

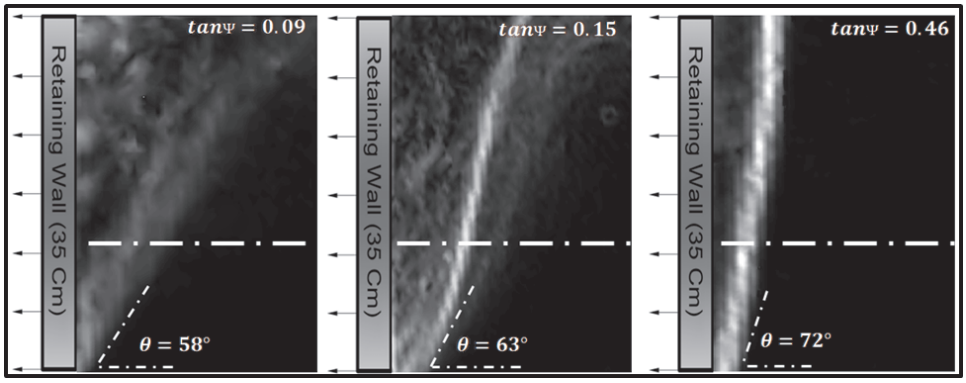


Figure 8.2. Gray Scale Shear Strain Profile of Backfills with Different Dilation Angles (ψ_p).

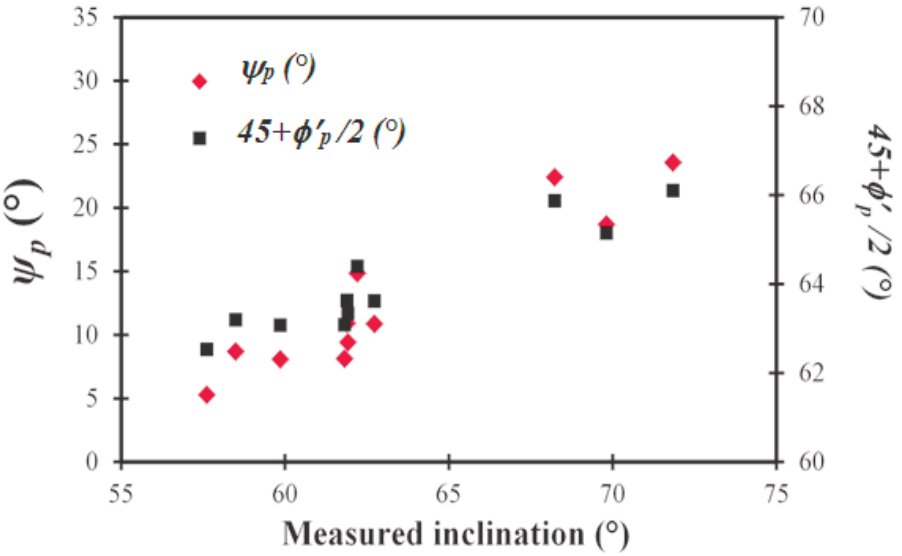
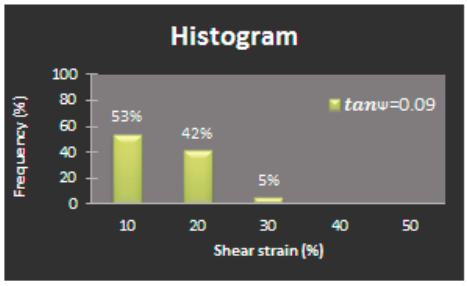


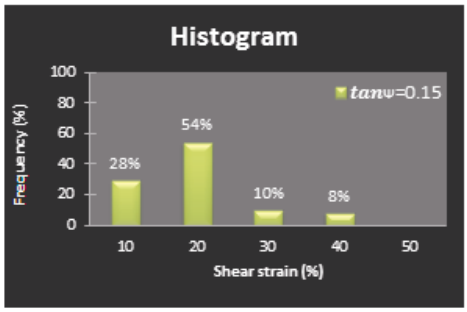
Figure 8.3. Variation of Measured Shear Band Inclination with $(45 + \phi'_p/2)$ and (ψ_p) at Active Failure State.

As an aid to the quantification of the variation of strain through the determined cross-section, the frequency of shear strain magnitude along the proposed cross-section was illustrated using a histogram. MATLAB program was used to obtain the histogram of each model test. According to the analyses, strain distribution along the shear band cross-section of an initially loose backfill seems to be limited dominantly to 0 - 20% range, as shown Figure 8.4. This supports the idea that in a backfill with small dilatancy angle (ψ_p), shearing deformations are in a lower range in comparison to dense backfills. For a medium dense backfill which own newly formed shear band, the strain

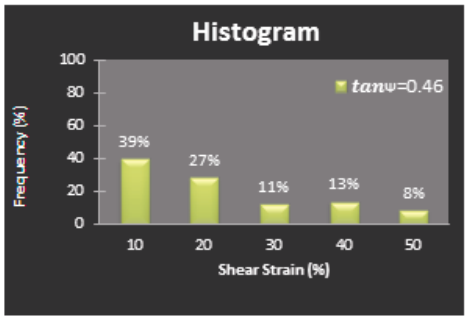
distribution changes relatively and even 40% shear strain was observed (Figure 8.4). However, for the initially dense backfill, which possess a narrow failure wedge and shearing deformations, the strain localized in a zone beside the wall with having a relatively high strain rates. Histogram results also allow calculating the average strain along the determined cross-section, so the magnitude of average shear strain can be compared for each backfill having different dilatant properties (Table 8.1). According to the Table 8.1, it is seen that average strain becomes higher with increasing dilatancy angle (ψ_p) of backfill.



(a)



(b)



(c)

Figure 8.4. The Frequency of Shear Strain Magnitude along the Determined Cross-Sections.

Table 8.1. Average Shear Strain Magnitude along the Determined Cross-Sections for Figure 8.2 and Figure 8.4.

tan (ψ_p)	Average Strain (%)
0.09	15.2
0.15	19.8
0.46	22.7

Shear strain intensity profile of the backfills through determined cross sections with different dilatancy angles (ψ_p) are shown in Figure 8.5. Based on the intensity profile graph, it is possible to identify the influence of dilatancy on shear band formation; it affects strain intensity and shear band thickness generated within the granular soil mass. It is clearly obtained that higher dilation angle (ψ_p) prompts a shear band with intense shear strain magnitude from Figure 8.5. Furthermore, the thickness of the shear band decreases as the dilation angle (ψ_p) increases. This means that, although the shear localization occurs in any density, the most distinct patterns appear at greater backfill densities. As the dilation angle (ψ_p) decreases, the shear zone covers a wider area starting from the toe of the wall and expanding towards the free boundary behind the retaining wall.

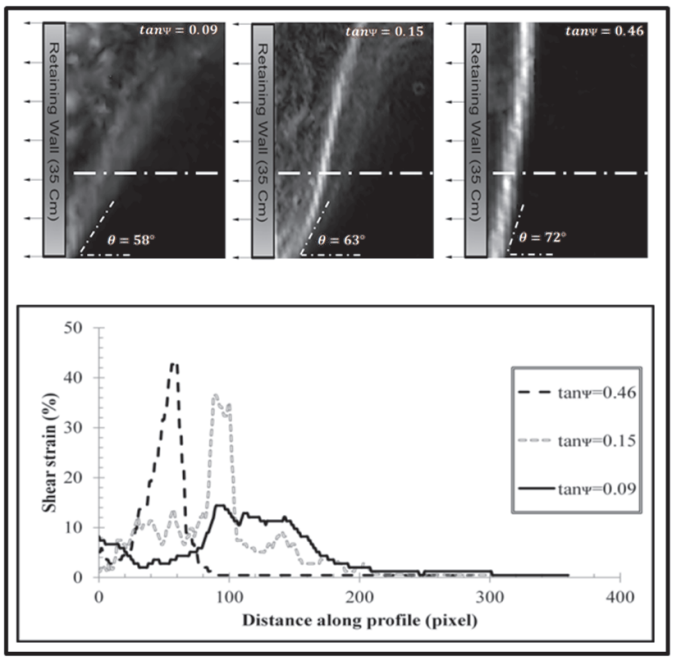
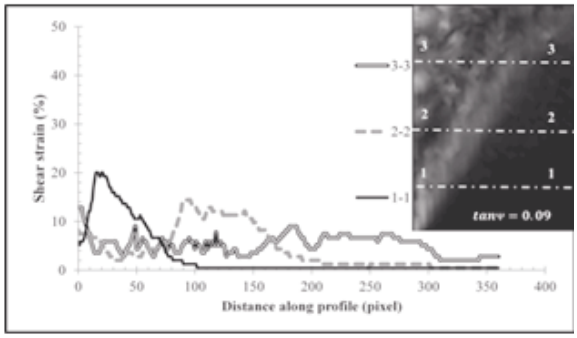


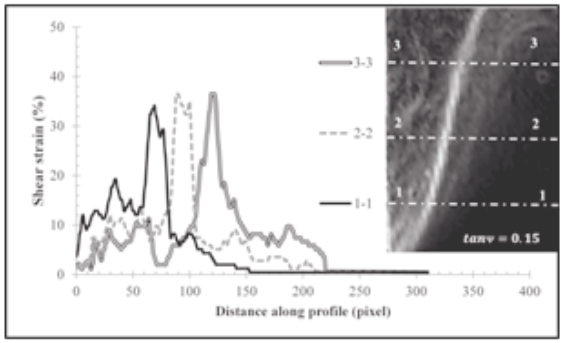
Figure 8.5. Shear Strain Intensity Profile along the Cross-Section.

To demonstrate the variation of strain within the slip zone, from wall top to its toe, cross-sections have been defined across three different positions on the strain map. Figure 8.6 shows the strain distribution along the soil mass with dilation angle of 5 degrees. The 1-1 cross-section represents the variations of strain near the toe of the wall. In comparison to 2-2 and 3-3, cross-section 1-1 yields more intense shearing records and has shown a maximum of 20% shear strain. As cross-sections that are more distant to the wall are considered, strain rate decreases, such that in 2-2 and 3-3 the strain rate drops to half the magnitude of that measured at the toe Cross-Section. Accumulation of strain along the shear band changes with position along the height of the retaining wall for loose granular backfills.

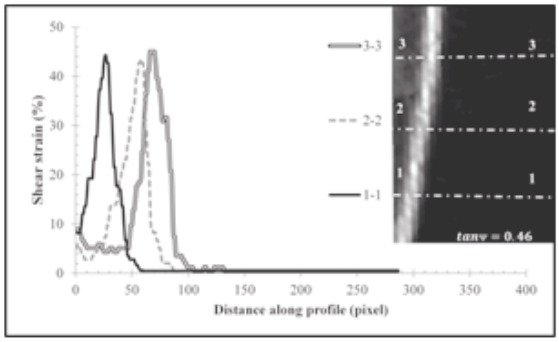
In Figure 8.6b and Figure 8.6c the intensity profiles of the backfills with dilation angles of 9 and 25 degrees are shown, respectively. It is clear that the shear strain magnitude does not change significantly as the positions of the cross-sections change with respect to the toe of the wall.



(a)



(b)



(c)

Figure 8.6. Shear strain intensity profile along the wall a) tan (ψ_p)=0.09 b) tan (ψ_p)=0.15 c) tan (ψ_p)=0.46.

Table 8.2 summarizes previous studies in the literature done with various computational and experimental methods at different initial void ratios to investigate shear band inclination at active state. These studies were concentrated on shearing properties of cohesionless materials retained behind walls. It is commonly observed that shear zones occur in backfills for all densities; however, it is important to evaluate shear strain intensity and distribution. It is well-established that initially loose sand owns a diffused shearing zone and its inclination at the toe section is lower than its value for

a dense backfill.

It is already stated that the thickness of the shear zone and the formed shear band depends on factors such as backfill density, wall roughness, mean grain diameter and mode of wall movement. Table 8.3 represents data available in literature for thickness of shear band and method used to measure it. Determination of the shear band thickness (t) is complicated and a reliable method of measurement must be adopted. For this purpose, in the present study a convenient method was used in light of works done by Niedostatkiewicz *et al.*, (2011). In this method the obtained data in image scale are calibrated to have an object scale measurement of strain distribution in the backfill. Then, the strain intensity profile provides quantified values of shear band thickness which is mainly represented by mean grain diameter (D_{50}). According to Niedostatkiewicz *et al.*, (2011), it was assumed that 50% of the maximum shear strain ($\varepsilon_{(s(max))}$) on the intensity profile is the outer wedge of the shear band as shown in Figure 8.7.

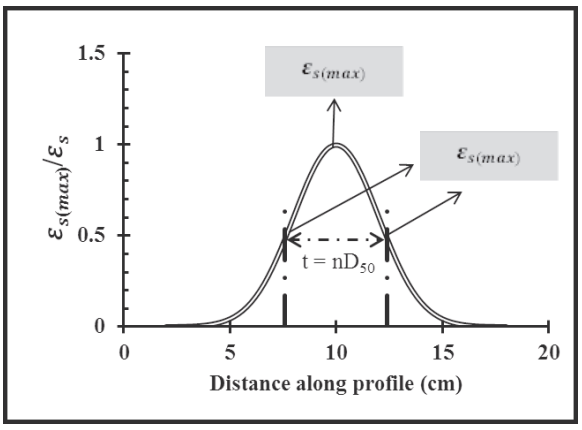


Figure 8.7. Determination of Shear Band Thickness.

Table 8.2. The summary of recorded θ values for shear band inclination.

Researcher	Density	Method	Surcharge (Mpa)	Inclination (^{o})
Nübel (2002)	I_D =0.8	PIV	0	68
J. Tejchman (2004)	Initially dense	FEM	0	50
M. Niedostatkiewicz (2009)	-	X-ray	0	65
M. Niedostatkiewicz *et al.*, (2011)	Initially dense	PIV	0	68
M. Niedostatkiewicz *et al.*,(2011)	Initially loose	PIV	0	65
Widulinski *et al.*,(2011)	Initially dense	DEM	0	58
Widulinski *et al.*,(2011)	Initially dense	FEM	0	50
D. Lesniewska *et al.*,(2012)	Initially dense	PIV	0	70
D. Lesniewska *et al.*,(2012)	Initially loose	PIV	0	60
D. Lesniewska *et al.*, (2012)	Initially dense	PIV	0.4	75
M Jiang *et al.*,(2014)	ID=19.2	DEM	0	58
M Jiang *et al.*,(2014)	ID=80	DEM	0	64
Tehrani *et al.*,(2014)	ID=0.15, ψ=0	DIC	0	65.3
Tehrani *et al.*,(2014)	ID=0.77, ψ=20	DIC	0	66.3

As it is expected, researchers suggested larger values of shear band thickness in loose backfills at active failure state, as given in Table 8.3. Shear band thicknesses (t) were measured at active failure state for each experiment and measurements of two of them having tan(ψ_p)=0.09 and 0.46 were shown in Figure 8.8. This measurement allows investigating the relationship between shear band thickness (t) and dilatancy angle (ψ_p). For this purpose, the relationship between dilatancy angles (ψ_p) versus shear band thickness (t) is presented in Figure 8.9. According to Figure 8.9, it is clearly seen that thickness of the shear bands vary between 90xD_{50} to 35xD_{50} in active model tests which is approximately in the same range with the experimental measurements done previously. Additionally, it was observed that t value increases with decreasing ψ_p. To put it in other words, thicknesses of shear bands are smaller in backfills having higher dilatancy angles (ψ_p) than backfills having smaller dilatancy angles (ψ_p).

Table 8.3. Summary of Recorded (t) Values for Shear Band Thickness.

Researcher	Density	Shear band thickness (t)	D50 (mm)	Method	Actual thickness (mm)
Nübel (2002) active	Initially dense	(11-15) x D_{50}	0.4	PIV	04.04.2006
D. Lesniewska *et al.*, (2012)	Initially dense	15 x D_{50}	0.8	PIV	12
D. Lesniewska *et al.*, (2012)	Initially dense	12.5 x D_{50}	0.8	PIV	10
D. Lesniewska *et al.*, (2012)	Initially loose	20 x D_{50}	0.8	PIV	16
M. Niedostatkiewicz (2009)	-	15 x D_{50}	0.8	X-ray	12
M. Niedostatkiewicz *et al.*, (2011)	Initially dense	12.5 x D_{50}	0.8	PIV	10
M. Niedostatkiewicz *et al.*, (2011)	Initially loose	18.5 x D_{50}	0.8	PIV	14.8
L. Widulinski *et al.*, (2011)	Initially dense	25 x D_{50}	1	DEM	25
L. Widulinski *et al.*, (2011)	Initially dense	32.5 x D_{50}	1	FEM	32.5
J. Tejchman (2004)	Initially dense	(30-35) x D_{50}	0.5	FEM	15 - 17.5
M. Jiang *et al.*,(2014)	Initially loose	7 x D_{50}	1.36	DEM	9.5
M. Jiang *et al.*, (2014)	Initially dense	16 x D_{50}	2.36	DEM	37.7

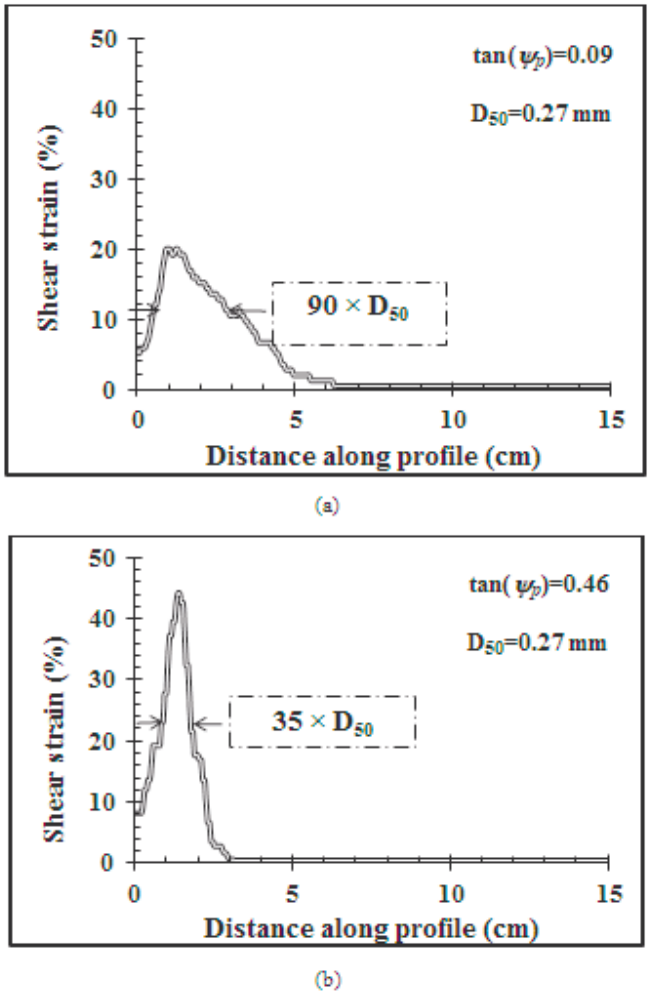


Figure 8.8. Shear Band Determination Based on Mean Grain Diameter at Active Failure State a) $\tan(\psi_p)$=0.09 b)$\tan(\psi_p)$=0.46.

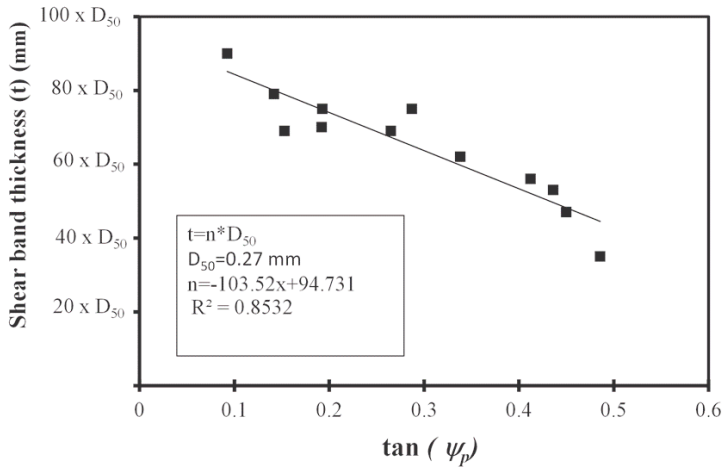


Figure 8.9. Variation of Shear Band Thickness with tan (ψ_p) at Active Failure State.

One outstanding option that GeoPIV provides is the accessibility of strain maps in any stage of test. Using this opportunity, the effect of wall translation on shear band thickness and inclination was investigated. Figure 8.10 shows results from three different steps of the rigid retaining wall movement; it is clear that in 1.5 mm translation, the shear band appeared and the angle that failure surface makes with horizontal is marked with α. As the model wall go further, that is 2.25 mm and 3 mm, the shear band becomes clearer and concentrated shear strain becomes more and more visible. Although soil reached its ultimate state, the inclination of the shear band seems to be constant and the change in thickness can be seen in Figure 8.10b. A cross section, in the same coordinates, of the strain maps for different wall displacements was selected and shear strain distribution graph was extracted using MATLAB. Based on the results it is monitored that the concentration of the accumulated strains are on the shear bands, however, the intensity of the strain is dependent on wall movement magnitude. On the other hand the thickness of shear band and its inclination is approximately constant with wall displacement, but the magnitude of strain is not.

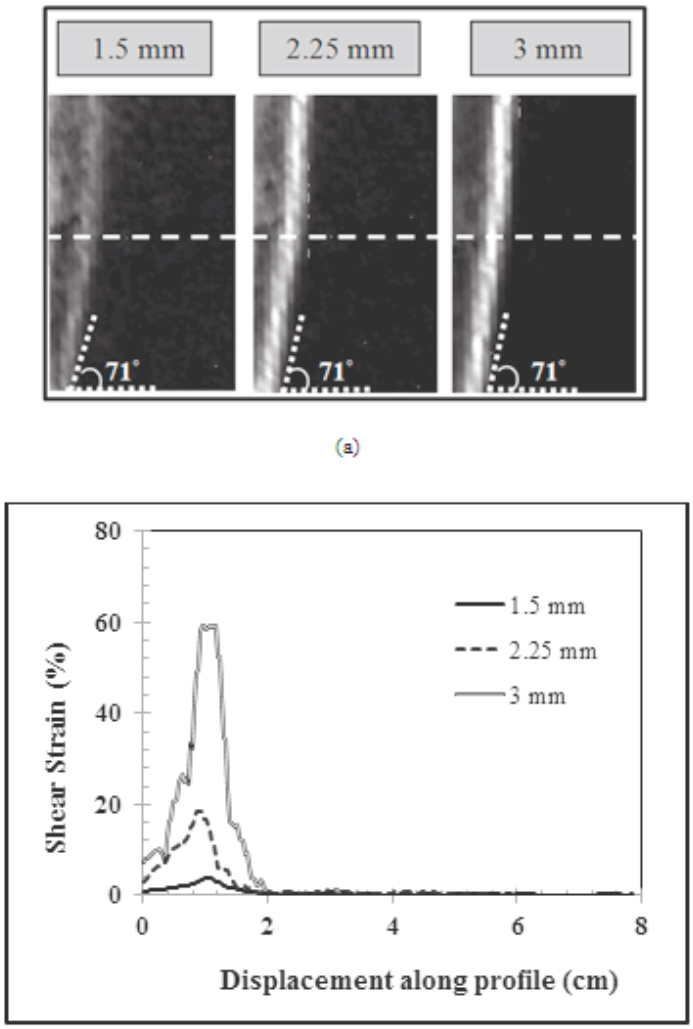


Figure 8.10. Shear Band Formation with respect to Wall Movement i) Strain Maps for Three Different Stages of Test 1.5, 2.25 and 3 mm ii) Intensity Profile of Shear Band on the Proposed Cross-Section.

9. DISCUSSION

Limit equilibrium methods are generally used for calculating earth pressures acting on geotechnical structures. As it is well known, Coulomb, Rankine and Terzaghi teories are based on limit equilibrium assumptions. These methods assume that failure is triggered along an assumed slip plane. The shear stress at every point along the assumed slip line reach a limiting shear stress equal to the shear strength of the material. The shear strength is controlled by shear strength parameters such as cohesion and friction (Shiau and Smith 2006). The limitation of the limit equilibrium method is the requirement of identifying the form of the slip plane (Shiau and Smith 2006). Additionally, classical limit equilibrium method assumes an associated flow rule, which restrict the plastic flow direction such that $\psi = \phi$ (Shiau and Smith 2006). Also, an associative flow rule assumes that the dilation angle of the soil is equal to the friction angle. However, in non-associated materials, dilation angle cannot be greater than friction angle. To be more precise, dilation angle is smaller than internal friction angle in soils. Therefore, this assumption leads to some errors when calculating earth pressures. However, the influence of dilatancy on slip plane geometry at both active and passive failure states have not been investigated yet experimentally in the literature.

In the present study, dependency of the shape of slip plane on ϕ'_p and ψ_p, as in the case of Equation 10 for active case and in the case of Figure 7.19 for passive case, is expected since the influences of ϕ'_p and ψ_p have been considered theoretically in soil plasticity (Atkinson 1981; Chen and Liu 1990; Bolton 1986; Salençon 1997). Generally accepted theoretical influence of dilatancy on a shear plane is conceptually illustrated in Figure 9.1. Since dilatant behavior results in a deformation component that is directed out of the plane of shearing, and the initial direction of the shear plane is dependent on ϕ'_p of the soil (Figure 9.1), in soil plasticity theory geometries of failure planes for frictional soils are controlled by strength and dilatant properties. However, this phenomenon has been dealt with only in theory since it is difficult to measure or calculate dilatancy angles of granular materials that constitute large masses; only dilatancy angles of soil samples can be measured. As a result, geotechnical modelling

studies that quantitatively consider dilatancy effect for both active and passive failure state are almost non-existent.

Problems associated with measuring or calculating dilatancy angles can be attributed to two main problems. First of all, measuring dilatancy is a difficult task since it is almost impossible to obtain high quality undisturbed samples of dilatant materials. Secondly, it is a well-established fact that dilatancy is dependent both on density and confinement; therefore any sample of granular soil that can be sampled in an undisturbed fashion will only be representative of the depth it is retrieved from. Same obstacles in measurement also hinder the calculation of dilatancy angles. Bolton (1986) developed an empirical equation that calculates peak dilatancy angle based on failure confining pressure (p'_f) and relative density (I_D). The underlying reason of Bolton (1986) for choosing p'_f for calculating ψ_p is its direct association to ϕ'_p. It is assumed that ϕ'_p signals the beginning of the plastic stage of deformation, thus it is an alternative way of looking at the flow rule. However, the requirement of the dilatancy equation proposed by Bolton (1986) to calculate ψ_p as a function of p'_finherently assumes the knowledge of ϕ'_p. Unfortunately, this requirement reduces the usability of the dilatancy equation proposed by Bolton (1986) in modelling studies. However, a novel equation proposed by Çinicioğlu and Abadkon (2014) overcomes these problems by using pre-shearing confining pressure (p'_i.) and relative density (I_D) as inputs (Equation 1). As a result, using Equation 5.1 and Equation 2.11 it becomes possible to calculate depth-dependent values of ϕ'_p and ϕ'_p as long as in-situ (pre-deformation) values of ϕ'_i and I_D values are known. That is why, Equation 5.1 is used in this study to calculate the dilatancy angles of backfills as functions of ϕ'_i and I_D. Combining the capability of dilatancy estimations with the image processing techniques, it is now possible to examine the influence of dilatant behavior on deforming granular bodies. Consequently, this study investigates and quantifies the effect of dilatancy on active and passive failure surfaces within granular soil mass.

On the other hand, Equation 5.1 can be inserted into Equation 7.11 and as a result active slip plane can be obtained for translation wall movement by considering the variations in density and confining pressure as long as they are known or calculated

for. Obtained results clearly suggest that the forms of the slip planes are functions of the soil density and stress state. The only requirement for using Equation 5.1 is that unit-independent soil constants α_ψ and m_ψ should be known. According to Çinicioğlu *et al.*, (2013), influences of p'_i and I_D on ψ_p are uncoupled. Therefore, constants α_ψ and m_ψ can be obtained by conducting a few triaxial or plane strain tests at different p'_i and I_D combinations. Thus, it is also possible to use the proposed equations in practical applications. Moreover, Equation 7.11 allows the consideration of the variations in dilatancy angle with depth. As a result, variations in soil density and stress state can be accounted for when the shapes of active slip planes are estimated. However, different types of sand need to be tested to show the universality of Equation 7.11. Additionally, presented model tests were conducted with low confining pressures. Therefore, a new model system with a loading system can be instrumented or presented model can be modified for applying sufficient external surface pressure to observe the effect of pressure level on slip plane for future studies. It is stated in literature that effect of wall friction on the shape of the slip surface is small and can be ignored (Craig 2004) at active failure state. In the present study, this result was also supported with a few model tests. ven though the small possible influences of wall friction on active failure planes are ignored in this study, these influences can be considered as a possible future topic for investigation.

On the contrary, the interface friction between wall and backfill gain much more importance for passive failure conditions and the resulting passive slip planes. Therefore, the effect of dilatant behavior on slip plane could be investigated in this study and the relationship between the geometry of passive slip plane and dilation angle was revealed, but an equation to identify the passive slip plane geometry could not be suggested, yet. To identify the slip plane geometry by a simple equation, an experimental study considering different interface friction angles between wall and backfill should be conducted. Based on the PIV analyses and results of model tests, it is seen that dilatant behavior influences passive slip plane geometry. This result was expected, since it is known that passive earth pressure strongly depends on the magnitude and distribution of the initial density, pressure level and mean grain diameter (Tejchman and Tantono 2007). Strain map could not be obtained for passive failure state in the

present study due to presence of steel braces located on the plexiglass side walls. These braces lead to dark areas on the failure wedge so the slip planes cannot be observed entirely. Therefore, slip plane was determined using displacement vector fields. To eliminate this limitation, testing tank need to be modified for investigating the strain localization on shear band at passive failure.

It is evident from the above discussion that there is a lack of knowledge on the influence of dilatant behavior on slip plane geometry for both active and passive failure conditions. Beside the present study, it needs more investigation in detail for obtaining safe and economic design.

In the light of previous studies, it is seen that very sensitive determination of the shear band thickness and inclination is not possible. However, strain map intensity profiles offer a promising method for the quantification of strain distribution across shear bands generated. Furthermore, utilization of intensity profile allows the measurement of the variation of strain along the slip plane in a much more simple and visible fashion. Besides, strain intensity profile and also strain map allows observing the influence dilatant behavior on shear band thickness and inclination. According to this, it was observed that there is a relationship between shear band thickness (t) and dilatancy angle (ψ_p). This is expected, since dilatant behavior in granular materials is a function of void ratio and confining pressure. However, it should be noted that PIV technique is a useful technique to monitor the processes of shear band deformation, but the thickness of the shear band slightly differs for different patch sizes used in the analyses. The distribution of strain on determined cross-sections can be quantified using strain histograms, so that the average strain on each section can be measured for the first time in this study.

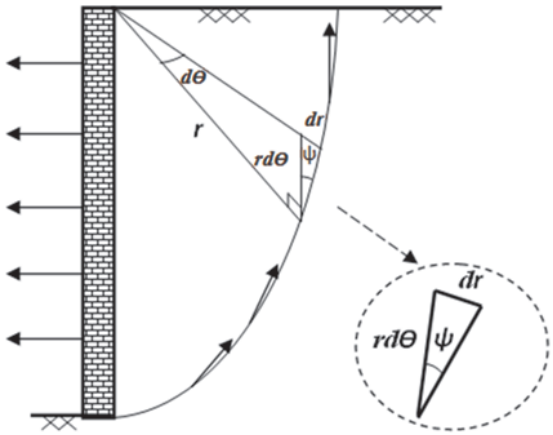


Figure 9.1. Influence of Dilatancy on Shear Plane According the Soil Plasticity Theory.

10. CONCLUSIONS

This study attempts to investigate the effect of dilative behavior on slip plane geometry and strain localization using the results obtained from small scale physical model tests and PIV analyses. For this purpose, a small scale retaining wall model has been constructed. Several model tests were run at 1 g until active and passive failures are simulated. Images captured during the tests were analyzed using PIV method and the resulting slip planes were identified. Based on the results, it is observed that PIV method allows quantification of the deformation by measuring displacements in granular geomaterials and allows visualization of the dilative and contractive behaviors within the failure wedge. Following the proposition of soil plasticity theory that the shapes of slip planes in frictional materials are dependent on the dilatant properties, influence of peak dilatancy angle on active and passive shear planes were examined. For this purpose a novel equation proposed by Çinicioğlu and Abadkon (2014), which allows the computation of peak dilatancy angle as a function of soil density and effective confining pressure, was used to calculate peak dilatancy angles of backfills. Analyzing the results, it is noticed that there is a clear and direct correlation between the calculated dilatancy angles and general characteristics of the active and passive slip planes. In other words, formation of slip plane in sand depends on the dilatant properties of the backfill for both active and passive failure. Additionally, model tests' results suggest that the geometries of active failure surfaces can be quantified using a 2^{nd} order parabolic function, as previously proposed by Spangler and Handy (1984). Accordingly, a parabolic function that uses ϕ'_p and ψ_p as inputs was defined for calculating the shapes of the active failure surfaces for problems in which the backfill is horizontal and the wall moves in translation mode. Using the proposed equation together with the dilatancy equation proposed by Çinicioğlu and Abadkon (2014) allows the computation of the active failure surface shape as a function of soil density and stress state. Thus, it becomes possible to account for the variations in strength and dilatancy throughout the backfill soil. Based on the results, calculated slip planes using the proposed equation for active failure were compared with the measured ones and the results were discussed. The relationships between earth pressure coefficients

and dilatancy angles were also examined. Based on the results, it is reported that ψ_p controls both the K_a and K_p values. With increasing ψ_p, K_a values of the backfills are decreasing whereas K_p values are increasing.

Additionally, progressive deformation was monitored through the shear zones both in shear and in volumetric strains by means of PIV method. Strain map intensity profiles and histograms were obtained by means of MATLAB program. These profiles provide a way to quantify the strain distribution across shear bands generated within the failure wedges behind the retaining wall with a more accurate way for the backfills with different dilatant properties. According to these profiles, it is seen that dilatant behavior influences shear band thickness and inclination at active state. It has been experimentally shown that the values of shear band thickness (t) increases with decreasing dilatancy angle (ψ_p) and shear band inclination (θ) increases with increasing dilatancy angle (ψ_p). Employing shear intensity profile allows monitoring variation of strain within the failure wedge and histogram allows measuring the average strain along the determined cross-sections. Based on both volumetric and shear strain map and intensity profile, it was monitored that shear zones can occur also in initially loose sand. However, dense backfill presents a narrow and steep shear band, whereas, the loose backfill possesses a wide and scattered shear band. Furthermore, when the shear bands initiate, further wall movement has no considerable effect on the properties of shear zone; the boundary of the shear band thickness and inclination remains constant.

REFERENCES

Abadkon, A. 2012, *Strength and Dilatancy of Anisotropic Cohesionless Soils*, Ph.D. Thesis, Bogazici University.

Adrian, R.J., 1991, "Particle Imaging Techniques for Experimental Fluid Mechanics", Ann. Rev. Fluid Mech, Vol. 23, No. 1, pp. 261-304.

Alshibli, K.A., S. Sture, 2000, "Shear Band Formation in Plane Strain Experiments of Sand" *Journal of Geotechnical and Geoenvironmental Engineering, American Society of Civil Engineering*, Vol. 126, pp. 495-503.

American Society for Testing and Materials. 2006, "Standard Test Methods for Minimum Index Density and Unit Weight of Soils and Calculation of Relative Density". *ASTM D-4253.*

American Society for Testing and Materials. 2006, "Standard test Methods for Minimum Index Density and Unit Weight of Soils and Calculation of Relative Density". *ASTM D-4254.*

American Society for Testing and Materials, 2006, "American Society for Testing and Materials, Standard Test Methods for Specific Gravity of Soil Solids by Water Pycnometer", *ASTM Standards: D854.*

American Society for Testing and Materials, 2007, "Standard Test Method for Particle Size Analysis of Soils", *ASTM Standards: D 422-63.*

Atkinson, J., 1981, *Foundations and Slopes*, McGraw-Hill, London.

Benmeddour, D.M., R., Mellas, A., Frank, A., Mabrouki, 2012, "Numerical Study of Passive and Active Earth Pressures of Sands", *Computers and Geotechnics*, Vol. 40, pp. 34-44.

Bishop, A.W. 19722, "Shear Strength Parameters for Undisturbed and Remoulded Soils Specimens". *In Stress-Strain Behaviour of Soils*, pp. 3-58 (ed. R. H. G. Parry). London: Foulis.

Bolton, M.D. 1986, "Strength and Dilatancy of Sands", *Geotechnique*, Vol. 36 No.1, pp. 65-78.

Borja, R.I., X., Song, A.L., Rechenmacher, S., Abedi, W., Wu, 2012, "Shear Band in Sand with Spatially Varying Density", *Journal of the Mechanics and Physics of Solids*, Vol. 61, pp. 219-234.

Brinch-Hansen, J. 1953, "Earth Pressure Calculation", *Danish Technical Press, Copenhagen, Denmark.*

Butterfield, R., R.M., Harkness, 1970, "Verawes, Stereo-Photogrammetric Technique for Measuring Displacement Field", *Geotechnique*, Vol. 20, pp. 308-314.

Caquot, A., and L., Kerisel, 1948, "Tables de Poussee et Butee". *Paris: Gauthier-Villars.*

Chakraborty, T., and R., Salgado, 2010, "Dilatancy and Shear Strength of Sand at low Confining Pressures", *Journal of Geotechnical and Geoenvironmental Engineering*, Vol. 136 No. 3, pp. 527-532.

Chen, W.F., and X.L., Liu, 1990, "Limit analysis in soil mechanics", *Elsevier, Amsterdam.*

Cho, G.C., J., Dodds, 2006, "Santamarina, Particle Shape Effects on Packing Density. Stiffness, and Strength: Natural and Crushed Sands", *Journal of Geotechnical and Geoenvironmental Engineering*, Vol. 132, pp. 591-602.

Cole, R.T., and K.M., Rollins, 2006, "Passive Earth Pressure Mobilization During Cyclic Loading." *Journal of Geotechnical and Geoenvironmental Engineering, American Society of Civil Engineering*, Vol. 132, No. 9, pp. 1154-1164.

Çinicioğlu, O., and A., Abadkon, 2014, "Dilatancy and Friction Angles Based on In-Situ Soil Conditions." *American Society of Civil Engineering, Journal of Geotechnical and Geoenvironmental Engineering (accepted for publication).*

Çinicioğlu, O., A., Abadkon, A., Altunbas, and M., Abzal, 2013, "Variation of Friction Angle and Dilatancy for Anisotropic Coheisonless Soils", *Proceedings, 18th International Conference on Soil Mechanics and Geotechnical Engineering*; pp. 2-6.

Coulomb, C.A. 1776, "Essai Sur Une Application Des Regles De Maximis Et Minimis A Quelques Problèmes De Statique". *Relatifs À l'Architecture. Memoires De l'Academie Royale Pres Divers Savants*, Vol. 3, pp. 343-382.

Craig, R.F., 2004 "Soil Mechanics", *Chapman and Hall.*

Desrues, J., W., Hammad, 1989, "Shear banding dependency on mean pressure level in sand", *In: Dembicki, E., et al. (eds.) Proc. Int. Workshop on Numerical Methods for Localization and Bifurcation of Granular Bodies, Gdansk, Poland*, pp. 57-67.

Desrues, J., R., Chambon, M., Mokni, F., Mazerolle, 1996, "Void Ratio Evolution Inside Shear Bands in Triaxial Sand Specimens Studied by Computed Tomography", *Géotechnique*, Vol. 46, pp. 529-546.

Desreues, J.G., 2004, "Viggiani, Strain Localization in Sand: Overview of the Experiments in Grenoble Using Stereo Photogrammetry", *Int. J. Numer. Anal. Meth. Geomech*, Vol. 28, No. 4, pp. 279-321.

Dubrova, G.A., 1963, "Intersection of Soil And Structures", *Izd. Rechnoy Transport, Moscow.*

Fang, Y.S. and I., Ishibashi, 1986, "Static Earth Pressures With Various Wall Movements", *Journal of Geotechnical Engineering*, Vol. 112, pp. 317-33.

Fang, Y., Y., Ho, and T., Chen, 2002, "Passive Earth Pressure With Critical State

Concept", *J. Geotech. Geoenviron. Eng.*, Vol. 128 No. 8, pp. 651-659.

Fang, Y.S., C.C., Lee and T.J., Chen, 2006, "Passive Earth Pressure with Various Backfill Densities", *Physical Modelling in Geotechnics-6th I CMPG'6-Ng, London, England.*

Goel, S., 2008, "Patra, Effect of Arching on Active Earth Pressure For Rigid Retaining Walls Considering Translation Mode", *International Journal of Geomechanics*, Vol. 8, pp. 123-133.

Duncan, J.M. and R.L., Mokwa, 2001, "Passive Earth Pressures:Theory and Tests", *Journal of Geotechnical and Geoenvironmental Engineering, American Society of Civil Engineering*, Vol. 127, No. 3, pp. 248-57.

Handy, R.L., 1985, "The Arch in Soil Aarching", *Journal of Geotechnical Engineering*, Vol. 111, pp. 302-318.

Hanna, A., and I.A., 2005, "Khoury, Passive Earth Pressure of Overconsolidated Cohesionless Backfill", *Journal of Geotechnical and Geoenvironmental Engineering*, Vol. 131, No. 8.

Jaworski, A.T., 2001, "Dyakowski, Application of Electrical Capacitance Tomography for Measurement of Gas-Solids Flow Characteristics in a Pneumatic Conveying System", *Measurement Science and Technology*, Vol. 12, pp. 1109-1119.

Kerisel, J., E., Absi, 1990, "Tables de Poussée et de Butée Des Terres", *3rd ed., Pressesde l'E ´ cole Nationale des Ponts et Chaussées, Paris.*

Khosravi, M.H., T., Pipatpongsa, and J., Takemura, 2013, "Experimental Analysis of Earth Pressure against Rigid Retaining Walls under Translation Mode", *Geotechnique*, Vol. 63, No. 12, pp. 1020-1028.

Kramer, S., 1996, "Geotechnical earthquake engineering", *Upper Saddle River, NJ, Prentice-Hall.*

Krumbein, W.C., and L.L., Sloss, 1963, "Stratigraphy and Sedimentation", *Freeman and Company, San Francisco.*

Kumar, J., and K.S., Subba Rao, 1997, "Passive Pressure Coefficients, Critical Failure Surface and its Kinematics Admissibility." *Geotechnique*, Vol. 47 No. 1, pp. 185-192.

Janbu N., 1957, "Earth Pressure and Bearing Capacity Calculations by Generalized Procedures of Slices. Proc", 4th Int. Conf. on *Soil Mechanics and Foundation Engineering*, London. Vol. 2, pp. 207-212.

Lade, P.V., 2002, "Instability, Shear Banding and Failure in Granular Materials", *I. J. Solids Structures*, Vol 39, pp. 3337-3357.

Lenoir, N., M., Bornert, J., Desrues, P., Bésuelle and G., Viggiani, 2007, "Volumetric Digital Image Correlation Applied to X-Ray Micro Tomography Images From Triaxial Compression Tests on Argillaceous Rocks", *Strain, International Journal For Experimental Mechanics*, Vol. 43, pp. 193-205.

Lesniewska, D., 2000, "Analysis of Shear Band Pattern Formation in Soil", *Institute of Hydroengineering of the Polish Academiy of Sciences (IBW PAN).*

Lesniewska, D. and Z., Mroz, 2001, "Study of Evolution of Shear Band Systems in Sand Retained by Fexible Wall", *Int. J. Numer. Anal. Meth. Geomech*, Vol. 25, pp. 909-932.

Lesniewska, D. and D., Muir Wood, 2011, "Photoelastic and Photographic Study of a Granular Material", *Géotechnique*, Vol. 61, pp. 605-611.

Lesniewska, D., M., Niedostatkiewicz, and J., Tejchman, 2012, "Experimental Study on Shear Localisation in Granular Materials Within Combined Strain and Stress Field", *Strain*, Vol. 48, pp. 430-444.

Loukidis, D., R., Salgado, 2012, "Active Pressure On Gravity Walls Supporting Purely

Frictional Soils", *Canadian Geotechnical Journal*, Vol. 49, pp. 78-97.

Matsuzawa, H. and H., Hazarika, 1996, "Analyses of Active Earth Pressure Against Rigid Retaining Wall Subjected to Different Modes of Movement", *Soils and Foundations, Japanese Geotechnical Society*, Vol. 36, No. 3, pp. 51-65.

Nadukuru S.S., R.L. 2012, "Michalowski Arching in Distribution of Active Load on Retaining Walls", *Journal of Geotechnical and Geoenvironmental Engineering*, Vol. 138, pp. 575-584.

Narain, J., S., Saran and P., Nandakumaran, 1969, "Model Study of Passive Pressure in Sand", *Journal of Soil Mechanics and Foundation Engineering Division, American Society of Civil Engineering*, Vol.95, pp. 969-83.

Niedostatkiewicz, M., K., Grudzien, Z., Chaniecki, and J., 2008, "Tejchman, Determination of the Bulk Solid Concentration Changes During Granular Flow in a Model Silo with ECT sensors", *Chemical Engineering Science*, Vol. 64, pp. 20-30.

Niedostatkiewicz, M., D., Les´niewska, and J., Tejchman, 2011, "Experimental Analysis of Shear Zone Patterns in Sand During Earth Pressure Problems Using Particle Image Velocimetry", *Strain*, Vol. 47, pp. 218- 231.

Nübel, K., and V., Weitbrecht, 2002, "Visualization of Localization in Grain Skeletons with Particle Image Velocimetry", *Journal of Testing and Evaluation, JTEVA*, Vol. 30, No. 4, pp. 322-329.

Paik, K.H., and R., Salgado, 2003, "Estimation of Active Earth Pressure Against Rigid Retaining Wallsconsidering Arching Effects", *Géotechnique*, Vol. 53, pp. 643-653.

Pan, B., K., Qian, H., Xie, A., Asundi, 2009, "Twodimensional Digital Image Correlation for In-Plane Displacement and Strain Measurement: A Review", *Measurement Science and Technology*, Vol. 20, No. 6, pp. 062-001.

Pietrzak, M. and D., Lesniewska, 2012, "Failure Evolution in Granular Material Re-

tained by Rigid Wall In Active Mode", *Studia Geotechnica et Mechanica*, Vol. 305, No. 4.

Rankine, W.J.M., 1857, "On the Stability of Loose Earth", *Philosophical Transactions of the Royal Society*, London, Vol. 147, pp.9-27.

Rechenmacher, A.L, 2006, "Grain-Scale Processes Governing Shear Band Initiation and Evolution in Sands", *J. Mech. Physics Solids*, Vol. 54, pp. 22-45.

Rechenmacher, A.L., S., Abedi, O., Chupin, and A.D., Orlando, 2011, "Characterization of Mesoscale Instabilities in Localized Granular Shear Using Digital Image Correlation", *Acta Geotechnica*, Vol. 6, pp. 205-217.

Rechenmacher, A.L., and R.J., Finno, 2014, "Digital Image Correlation to Evaluate Shear Banding in Dilative Sands Geotechnical Testing Journal", Vol. 27, No. 1.

Reddy, N.S.C., D.M., Dewaikar, 2013, "Mohapatra, International Journal of Advanced" *Civil Engineering and Architecture Research*, Vol. 2, No. 1, pp. 32-41.

Reynolds, O. 1885, "On the Dilatancy of Media Composed of Rigid Particles in Contact." *Philosophical Magazine*, Vol. 20, No. 5, pp. 469-481.

Roscoe, K.H., J.R.F., Arthur, and R.G., James, 1963, "The Determination of Strains in Soils by an X-Ray Method", *Civil Engineering Public Works Revision*, Vol. 58, pp. 873-876, pp.1009-1012.

Rowe, P.W. 1969, "The Relation Between the Shear Strength of Sands in Triaxial Compression, Plane Strain, and Direct Shear." *Geotechnique*, Vol. 19, No. 1, pp. 75-86.

Saada, A.S., L., Liang, J.L., Figueroa, C.T., Cope, 1999, "Bifurcation and Shear Band Propogation in Sands", *Geotechnique*, Vol. 44, No.3, pp. 367-385.

Sadrekarimi A., S., Damavandinejad Monfared 2013, "Numerical Investigation of The

Mobilization of Active Earth Pressure on Retaining Walls", *Proceedings of the 18th International Conference on Soil Mechanics and Geotechnical Engineering*, pp. 793-796.

Salençon, J. 1977, "Applications of the Theory of Plasticity in Soil Mechanics", *Wiley, New York*.

Schanz, T., and P.A., Vermeer, 1996, "Angle of friction and dilatancy of sand", *Geotechnique*, Vol. 46, No. 1, pp. 145-151.

Shiau, J., and C., 2006, "Smith, Numerical Analysis of Passive Pressures with Interfaces. 3. European Conference on Computational Mechanics Solids", *Structures and Coupled Problems in Engineering*, Vol. 1, pp. 5-8.

Shiau J.S., *et al.*, 2008, "Finite Element Limit Analysis of Passive Earth Resistance in Cohesionless Soils", *Japanese Geotechnical Society, Soils and Foundations*, Vol. 48 No. 6, pp. 843-850.

Shields, D.H., and A.Z., Tolunay, 1973, "Passive Pressure Coefficients by Method of Slices", *J. Soil Mech. Found. Div*, Vol. 99 No. 12, pp. 1043-1053.

Slominski, C., M., Niedostatkiewicz, and J. Tejchman, 2006, "Deformation Measurements in Granular Bodies Using a Particle Image Velocimetry Technique", *Archives of Hydro-Engineering and Environmental Mechanics* Vol. 53 No. 1, pp. 71-94.

Slominski, C.C., M., Niedostatkiewicz, and J. Tejchman, 2007, "Application of Particle Image Velocimetry (PIV) for Deformation Measurement During Granular Silo Flow", *Powder Technol* Vol. 173, pp. 1-18.

Soubra, A.H. 2000, "Static and Seismic Passive Earth Pressure Coefficients on Rigid Retaining Structures", *Can. Geotech*, Vol. 37, pp. 463-478.

Spangler, M.G., and R.L., Handy, 1984, "Soil Engineering", *Harper and Row*, New York,.

Tehrani, F.S., M.I., Arshad, M., Prezzi, and R. Salgado, 2014, "Visualization of Active Mode of Failure Behind Flexible Walls under Pure Rotation Using Digital Image Correlation. Geo-Congress 2014 *Technical Papers, GSP 234, American Society of Civil Engineering.*

Taylor, D.W. , 1948, "Fundamentals of Soil Mechanics, *John Wiley and Sons*, New York.

Tejchman, J., W., Wu, 1995, "Experimental and Numerical Study of SandSteel Interfaces". *International Journal for Numerical and Analytical Methods in Geomechanics*, Vol. 19, pp. 513-537.

Tejchman, J., Bauer, E., Tantono, S.F., 2007, "Influence of Initial Density of Cohesionless Soil on Evolution of Passive Earth Pressure", *Acta Geotech*, Vol. 2, No. 1, pp. 53-63.

Tejchman, J. 2008, "Shear Localization in Granular Bodies with Micro-Polar Hypoplasticity", *Springer Series in Geomechanics and Geoengineering*, Berlin Heidelberg.

Tejchman, J., W., Wu, 2010, "Boundary Effects on Behaviour of Granular Material During Plane Strain Compression", *European Journal of Mechanics, A/Solids*, Vol. 29 No. 1, pp. 18-27.

Terzaghi, K., 1920, "Old Earth-Pressure Theories and New Test Results." *Engineering News Record*, Vol. 85, No. 14, pp. 108-113.

Terzaghi, K., 1936, "A Fundamental Fallacy in Earth Pressure Computations", *Journal of the Bostan Society of Civil Engineers*, Vol. 23, pp. 71-88.

Terzaghi, K., 1943, "Theoretical Soil Mechanics", *Wiley*, New York.

Terzaghi, K., R.B., Peck, and G., 1920, "Mezri, Soil Mechanics in Engineering Practice", 3rd Ed., *John Wiley and Sons, Inc.*, New York.

Tsagareli, Z.V., 1965, "Experimental Investigation of the Pressure of a Loose Medium on Retaining Walls with a Vertical Back Face and Horizontal Backfill Surface", *Soil Mechanics and Foundation Engineering*, Vol. 2, pp. 197-200.

Toyosawa, Y., S.B., Tamrakar, N., Suemasa, 2006, "Redistribution of Active Earthpressures Using Movable Earth Support Apparatus in Centrifuge", *Physical Modelling in Geotechnics - 6th ICPMG*, pp. 1113-1118.

Vaid, Y.P., and S., Sasitharan, 1992, "The Strength and Dilatancy of Sand", *Canadian Geotechnical Journal*, Vol. 29, No. 3, pp. 522-526.

Viggiani, G., S.A., Hall, E., Romero, 2012, "Advanced Experimental Techniques in Geomechanics", *The Alliance of Laboratories in Europe for Research and Technology.*

Wang, Y.Z., 2000, "Distribution of Earth Pressure on a Retaining Wall", *Geotechnique*, Vol. 50, No. 1, pp. 83-88.

White D.J., 2002, "Take GeoPIV: Particle Image Velocimetry (PIV) Software for use in Geotechnical Testing", *Technical Report CUED/D-SOILS/TR322.*

White, D.J., W.A., Take, M.D., Bolton, 2003, "Soil Deformation Measurements using Particle Image Velocimetry (PIV) and Photogrammetry", *Géotechnique*, Vol. 5, pp. 619- 631.

White, D.J., M., Randolph, and B., Thompson, 2005, "An Image-Based Deformation Measurement System for the Geotechnical Centrifuge", *Int. J. Phys. Model. Geotech*, Vol. 3, pp. 1-12.

Whitlow, R., 2001, "Basic Soil Mechanics" *4th. Ed. Pearson Education, Essex.*

Widulinski, L., J., Tejchman, J., Kozicki, and D., 2011, "Lesniewska, Discretesimulations of Shear Zone Patterning in Sand in Earth Pressure Problems of a Retaining Wall", *Int. J. Solids and Structures*, Vol. 48, No. 7-8, pp. 1191-1209.

Wilson, P. and A., Elgamal, 2010, "Large Scale Passive Earth Pressure Load-Displa cment tests and Numerical Simulation", *Journal of Geotechnical and Geoenvironmental Engineering, American Society of Civil Engineering*, Vol. 12, pp. 136-137.

Yoshida, T., F., Tatsuoka, M.S.A., 1994, "Siddiquee, Shear Banding in Sands Observed in Plane Strain Compression", *In, Chambon, R., Desrues, J., Vardoulakis, I. (eds.) Localisation and Bifurcation Theory for Soils and Rocks, Balkema, Rotterdam*, Vol. 3, pp. 165-181.

Zhu, D.Y., and Q., Qian, 2000, "Determination of Passive Earth Pressure Coefficients by the Method of Triangular Slices", *Can. Geotech. J.*, Vol. 37, pp. 485-491.